DFT analysis on structure-property relationships of metal-substituted zeolites

by

Brian D. Montejo Valencia

A dissertation submitted in partial fulfillment of the requirements for the degree of

DOCTOR OF PHILOSOPHY
in
CHEMICAL ENGINEERING

UNIVERSITY OF PUERTO RICO
MAYAGÜEZ CAMPUS
2018

Approved by:

_____	_____
María C. Curet Arana, Ph.D. President, Graduate Committee	Date
_____	_____
Nelson Cardona Martínez, Ph.D. Member, Graduate Committee	Date
_____	_____
Alberto Santana Vargas, Ph.D. Member, Graduate Committee	Date
_____	_____
María M. Martínez Iñesta, Ph.D. Member, Graduate Committee	Date
_____	_____
Carmen A Vega, Ph.D. Representative of Graduate Studies	Date
_____	_____
Aldo Acevedo Rullán, Ph.D. Chairperson of the Department	Date

ABSTRACT

Metal-modified zeolites have proven to be effective catalysts for various important reactions involving the transformation of biomass-derived molecules and the conversion of greenhouse gases, such as CO_2 and CH_4. In this work, we analyzed metal-substituted zeolites and metal-exchanged zeolites in various zeolite frameworks in order to quantify the catalytic activity of these materials. Density functional theory (DFT) calculations, ONIOM calculations, which is an integrated quantum mechanical molecular mechanical method, and periodic DFT calculations were used to analyze these systems.

The substitution of Ti, Sn, Ge, Zr, and Hf in various zeolite frameworks were analyzed. The preferential substitution sites of these metals were reported. The Lewis acidity was measured through the NH_3 binding energies and through the charge transfer of NH_3 upon adsorption on the zeolites. The deprotonation energies of the open sites, which are proportional to the Brønsted acidities, and the hydrolysis energies were also reported. We also present the properties of zeolite beta (BEA) with a single and a double Sn-substitution to compare the active sites obtained with two methods commonly employed for the synthesis of Sn-BEA.

The opening of glucose and fructose rings catalyzed by M-BEA (M = Sn, Ti, Zr, Hf) zeolites were analyzed with periodic DFT calculations. We proposed a novel mechanism for the ring opening of these molecules in one elementary step, which can be achieved in the closed sites of the zeolites. The adsorption energies of glucose and fructose through their different oxygens in M-BEA were also reported. Among the zeolites studied, Sn-BEA exhibits the lowest energy barrier for the opening of the glucose ring, whereas Hf-BEA yields the lowest energy barrier for the opening of the fructose ring.

For the conversion of greenhouse gases, such as CO_2 and CH_4 into acetic acid, we analyzed the reaction catalyzed by MFI zeolite exchanged with Be^{2+}, Co^{2+}, Cu^{2+}, Mg^{2+}, Mn^{2+}, and Zn^{2+} cations. Our results demonstrated that the highest reaction barrier on the reaction mechanism is CH_4 dissociation. We also demonstrated that the CO_2 insertion has a low energy barrier, and the protonation of the acetate species is spontaneous. Furthermore, desorption of acetic acid can be promoted with the co-adsorption of water.

RESUMEN

Las zeolitas sustituidas con metal han demostrado ser catalizadores eficaces para diversas reacciones importantes que implican la transformación de moléculas derivadas de la biomasa y la conversión de gases de efecto invernadero tales como CO_2 y CH_4. En este trabajo, analizamos zeolitas de metal sustituido y zeolitas de metal intercambiado en varios marcos zeolíticos, para cuantificar la actividad catalítica de estos materiales. Para analizar estos sistemas se utilizaron cálculos de la teoría del funcional de la densidad (DFT), cálculos ONIOM, que es un método que integra mecánica cuántica con mecánica molecular y cálculos periódicos de DFT.

Se analizaron los sitios preferenciales de sustitución de Ti, Sn, Ge, Zr y Hf en diferentes marcos. La acidez Lewis se midió a través de las energías de enlace de NH_3 y a través de la transferencia de carga de NH_3 al adsorberse sobre las zeolitas. También se reportaron las energías de desprotonación de los sitios abiertos, que es proporcional a las acidez Brønsted, y las energías de hidrólisis. También se presentan las propiedades de BEA con una sola y una doble sustitución de Sn para comparar los sitios activos obtenidos con dos métodos comúnmente empleados para la síntesis de Sn-BEA.

Se analizó la apertura de los anillos de glucosa y fructosa con zeolitas M-BEA (M = Sn, Ti, Zr, Hf). Se propuso un nuevo mecanismo para la apertura del anillo en una etapa elemental, que se puede conseguir en sitios cerrados de las zeolitas. También se informaron las energías de adsorción de glucosa y fructosa a través de sus diferentes oxígenos en M-BEA. Entre las zeolitas estudiadas, Sn-BEA mostró la menor barrera energética para la apertura del anillo de la glucosa, mientras que Hf-BEA dio la menor barrera energética para la apertura del anillo de fructosa.

Para la conversión de gases de efecto invernadero, tales como CO_2 y CH_4 en ácido acético, se analizó la reacción usando zeolitas MFI intercambiadas con diferentes cationes (Be^{2+}, Co^{2+}, Cu^{2+},

Mg^{2+}, Mn^{2+} y Zn^{2+}) como catalizadores. Nuestros resultados demuestran que la mayor barrera de reacción en el mecanismo de reacción es la disociación de CH_4. También se demostró que la inserción de CO_2 tiene una barrera de energía baja y la protonación de las especies de acetato es espontánea. Además la desorción de ácido acético puede ser promovida con la co-adsorción de agua.

Chapter 2 of this dissertation is a reprint from an article published on the Journal of Physical Chemistry C. Reprinted with permission from Montejo-Valencia, B. D.; Curet-Arana, M. C. DFT Study of the Lewis Acidities and Relative Hydrothermal Stabilities of Bec and Bea Zeolites Substituted with Ti, Sn, and Ge. *J. Phys. Chem. C* **2015**, *119*, 4148–4157. Copyright (2015) American Chemical Society.

Chapter 3 of this dissertation is a reprint from an article published on the Journal of Physical Chemistry C. Reprinted with permission from Montejo-Valencia, B. D.; Salcedo-Pérez, J. L.; Curet-Arana, M. C. DFT Study of Closed and Open Sites of BEA, FAU, MFI, and BEC Zeolites Substituted with Tin and Titanium. *J. Phys. Chem. C* **2016**, *120*, 2176–2186. Copyright (2016) American Chemical Society.

Chapter 5 of this dissertation is a reprint from an article published on ACS Catalysis. Reprinted with permission from Montejo-Valencia, B. D.; Pagan-Torres, Y. J.; Martinez-Inesta, M. M; Curet-Arana, M. C. Density Functional Theory (DFT) Study To Unravel the Catalytic Properties of M-Exchanged MFI, (M=Be, Co, Cu, Mg, Mn, Zn) for the Conversion of Methane and Carbon Dioxide to Acetic Acid. *ACS Catal.* **2017** *7*, 6719–6728. Copyright (2017) American Chemical Society.

To my lovely wife, Natalia, who filled my life with her unconditional love and support.
To my mother, Alcira, who instilled in me the value of education since my childhood.

ACKNOWLEDGEMENTS

I would like to thank:

My lovely wife Natalia Almodovar Arbelo.

My parents Alcira Valencia Carmona and Luis Montejo Lizarralde. Thanks for your love and care.

My brother Luis Montejo Valencia, my sister in law Aidcer Vidot Vega and my beautiful nieces Elianna Montejo Vidot and Arianna Montejo Vidot. Thanks for your support in my life.

My friends: David Castilla Casadiego, Luis Pinzon, Rodinson Arrieta Perez, Valdimir Villanueva Lopez and Martha Rozo Medina. Thanks for always being there and accompany me through this way.

My mentor Professor Maria Curet Arana, for her guidance and mentoring.

My research partner Paul Meza, who taught me the fundamentals in the beginning of my research.

My graduate committee members: Professors Nelson Cardona Martinez, Alberto Santana, and Maria Martinez Iñesta, for their suggestions and corrections to this dissertation.

Dr. Manos Mavrikakis, Dr. Dane Morgan, Dr. Izabela Szlufarska, Dr. Guangfu Luo, and Dr. Srinivas Rangarajan at UW for the VASP training.

Professor Yomaira Pagan Torres for her corrections and feedback in my work.

National Science Foundation for the financial support through grants EPS-1002410 and OIA-1632824.

The National Energy Research Scientific Computing Center and the High-Performance Computing Facility of the Institute for Functional Nanomaterials for the computing facilities.

TABLE OF CONTENTS

LIST OF TABLES

LIST OF FIGURES

GLOSSARY OF TERMS

Al	Aluminum
Au	Gold
B	Boron
Be	Beryllium
BEA	Zeolite framework
BEC	Zeolite framework
BV	Baeyer-Villiger
B3LYP	Effective core potential basis set
B3PW9	Effective core potential basis set
Co	Cobalt
Cu	Cooper
DFT	Density Functional Theory
DFT-D3	Density Functional Theory with long range correction
DH	Dihydroxyacetone
DPE	Deprotonation Energies.
ESP	Electrostatic Potential
EXAFS	Extended X-Ray Absorption Fine Structure
$E_{B.E.}$	Electronic binding energy of ammonia in the zeolites.
E_{rx}	Electronic Reaction energy
E_{Zeo-M^-}	Electronic energy of the deprotonated and hydrolyzed metal- substituted zeolite
$E_{Zeo[M]h}$	Electronic energy of the hydrolyzed metal- substituted zeolite
FAU	Faujasite, zeolite framework
Fe	Iron
FER	Ferrierite, zeolite framework
FF	β-D fructofuranose
FTIR	Fourier Transform infrared
Ga	Gallium
Ge	Germanium
GP	α-D Glucopyranose
h	Planck constant

Hf	Hafnium
HMF	Hydroxymethylfurfural
HOMO	Highest Occupied molecular orbital
ITQ44	Zeolite framework
IRC	Intrinsic Reaction Coordinate
IZA	International Zeolite Association
LANL2DZ	Effective core potential basis set
LUMO	Lowest unoccupied molecular orbital
M	Metal to be substituted in the zeolite
MAS	Magic Angle Spinning
MFI	Zeolite framework
Mg	Magnesium
MM	Molecular Mechanism
Mn	Manganese
MOR	Mordenite, zeolite framework
MWB46	Effective core potential basis set
N	Nitrogen
NBO	Natural Bond Orbital
NEB	Nudge Elastic Band
NMR	Nuclear Magnetic Resonance.
ONIOM	Our Own N-layered. Integrated molecular Orbital, which is an integrated quantum mechanical – molecular mechanical method.
PAW	Projector Augmented Wave method
Pb	Lead
PBE	Perdew–Burke–Ernzrhof exchange-correlation
PCM	Polarizable Continuum Model
QM	Quantum mechanism
Ri	M/Si ratio
S	Singlet State
Si	Silicon
Sn	Tin

T	Temperature
TCF	Trillion Cubic Feet
T_I	T site $_I$ of the zeolite, which is the space occupied by a tetrahedral atom with a specific symmetry.
Ti	Titanium
TOF	Turn over frequency
TS	Transition State
UFF	Universal Force Field
VASP	Vienna ab Initio Simulation Package
VDW	Van der Waals
wt%	Weight percent
XRD	X-Ray Diffraction
Zn	Zinc
ZPE	Zero-Point Energy
Zr	Zirconium
6-31+g**	Basis set with diffusion and polarization
X	Electronegativity
η	Hardness
θ	Local structutal perturbation at the T-Site
α_i	i angle (O-T-O)
$\bar{\alpha}$	Average of the six angles (O-T-O)
φ	Parameter to normalize theta
k_B	Boltzmann constant
$k_{site}^{forward}$	Forward rate constant
p_{CH_4}	Methane partial pressure
θ_{site}	Number of catalytic sites
$r_{site}^{forward}$	Forward rate for CH_4 dissociation
$\Delta G^{\neq}{}_{site}$	Gibbs free energy barrier of the transition state
ωb97XD	Exchange Correlation functional

1 CHAPTER – INTRODUCTION

1.1 Justification

Zeolites are aluminosilicate materials normally composed of silicon, aluminum and oxygen atoms.[1] The incorporation of heteroatoms and metal cations in the zeolitic frameworks can be used to tailor the catalytic properties of these materials. For instance, the incorporation of heteroatoms such as Sn, Ti, Zr ,Hf, Nb, or Ta provides Lewis acidity. [2–20] On the other hand, the incorporation of cations, such as Be^{+2}, Co^{+2}, Cu^{+2}, Mg^{+2}, Mn^{+2}, or Zn^{+2} promotes electron donation mechanisms, which facilitates the activation of stable molecules on zeolites. [21–26]

Lewis acid zeolites are used for the activation and conversion of oxygenated compounds, such as the ones found in molecules derived from biomass.[27–33] Experimental parameters have been used to measure the Lewis acidity of the zeolites, such as the pyridine 15N magic angle spinning nuclear magnetic resonance chemical shift caused by the adsorption of pyridine on metal-substituted zeolites. It has been found that this shift is proportional to the experimental electronegativity of the zeolites.[34] On the other hand, several theoretical parameters have been also used to measure the acidity, such as the LUMO energies, Fukui functions, absolute electronegativity, and absolute hardness of the zeolites.[13]

Theoretical descriptors based solely on the properties of the zeolites do not accurately correlate with the experimental catalytic activity of these materials. For instance, calculated adsorption energies can be used to estimate the Lewis acidity, and trends obtained through this approach are similar to those obtained experimentally. Examples include the adsorption of NH_3 on MFI substituted zeolites.[35] However, even when NH_3 adsorption energies correlate well with the Lewis acidity, this descriptor does not correlate with the catalytic activity of the zeolite. Thus, a comprehensive analysis of these catalysts should include not only the Lewis acidity, but also other

relevant parameters such as the type of reactions, the substitution site of the metal in the zeolite framework, the hydrothermal stability, the zeolitic framework (MFI, BEA, FAU, …), and most importantly the interaction of the reactants, products, and transition states with the catalyst.

Metal-substituted zeolites differ in their catalytic activity depending on the framework employed and on the metal atom used for the functionalization. For instance, Ti-substituted zeolites catalyze the epoxidation of linear alkenes with H_2O_2,[36,37] whereas Zr- and Sn- substituted zeolites do not.[38] Similarly, Sn-substituted zeolites show high initial rates in Baeyer-Villiger (BV) oxidation of cyclic ketones with H_2O_2, and Ti- substituted zeolites do not catalyze this type of reaction.[38] The main difference between these two examples is based on the reaction mechanism. The first step in the epoxidation of alkenes is the adsorption and activation of H_2O_2, which can promoted by Ti- substituted zeolites, while for the BV reactions, the first step of the mechanism is the activation of the carbonyl group, which can be enhanced by Sn-substituted zeolites.[38] In other reactions, such as the isomerization of glucose to fructose,[2] isomerization of glyceraldehyde to dihydroxyacetone (DH),[39] and C-C coupling between DH and formaldehyde,[40] Sn-substituted zeolites usually show high catalytic activity.

The experimental rates that are commonly reported to quantify the activity of zeolites are based on rates normalized by the total metal content, and usually do not take into consideration the possible extra-framework species that may be formed by the metals. Moreover, the metal substituted in the zeolitic framework could be incorporated in several configurations. For instance, metals can be incorporated into the zeolite as a fully connected tetrahedron (closed sites) or could have one, two or even three hydrolyzed Si-O-M bonds (open site).[41] Furthermore, even at mild conditions, the sites can be hydrated with two water molecules forming a octahedral geometry.[3]

The T-Sites and the local geometry of the active sites in the zeolites are factors that also influence the catalytic performance. For instance, Osmundsen and coworkers reported that the reaction of dihydroxyacetone to methyl lactate has higher yields when catalyzed by Sn-BEA than by Sn-MFI, with the same Si/Sn ratio.[16] Corma and coworkers, in a density functional theory (DFT) study, demonstrated that the lowest unoccupied molecular orbital (LUMO) energies vary depending on the Si-O-Ti angle of the T-sites, suggesting that Ti-BEA has a stronger Lewis acidity than Ti-MFI.[42]

In this work, different metal substituted zeolites were analyzed with DFT methods in order to guide the rational design of zeolitic catalysts for the conversion of biomass. Parameters, such as the LUMO energies, charges, and hardness for different T-sites, metal atoms, and zeolitic frameworks were quantified. The adsorption of probe molecules, such as NH_3 in various zeolites were also obtained. Furthermore, the reaction mechanisms for the opening of the glucose and fructose rings were studied in various metal-substituted zeolites. It is well known that during the transformation of biomass into added-value chemicals some undesirable products are also produced. For instance, the reforming of glycerol and glucose to produce alkanes and H_2, respectively also produces CO_2, which is a green-house gas.[43] Thus, in this work we also studied the incorporation of metal cations in zeolites for the conversion of CO_2 and CH_4 into acetic acid.

1.2 Objectives

The main objective of the proposed research is to rationalize the catalytic activity of the metal-modified zeolites. Density functional theory (DFT), ONIOM, which is an integrated quantum mechanical – molecular mechanical method, and periodic DFT calculations were used to analyze

these systems. This research is comprised of four projects. The goals of each of these research projects can be summarized as follows:

1. A DFT study of the Lewis acidities and relative hydrothermal stabilities of BEC and BEA zeolites substituted with Ti, Sn and Ge.
    - Describe the electronic properties of BEC and BEA zeolites substituted with Ti, Sn and Ge. Calculate properties, such as lowest unoccupied molecular orbital (LUMO) energies, partial atomic charges and hardness for each of these systems.
    - Find the preferential sites of substitution of Sn, Ti and Ge in BEA and BEC.
    - Correlate the Lewis aciditiy of the metal substituted zeolites with their electronic properties.
    - Relate the hydrothermal stabilities of the metal substituted zeolites with their hydrolysis energies.
2. DFT study of closed and open sites of BEA, BEC, FAU, MFI zeolites substituted with Sn and Ti.
    - Describe electronic properties of BEA, BEC, FAU and MFI zeolites substituted with Sn and Ti. Calculate properties, such as LUMO energies, binding energies of NH_3, partial atomic charges, hardness and deprotonation energies of the hydrolyzed zeolites for each of these systems.
    - Find the preferential sites of substitution of Sn, and Ti in BEA, BEC, MFI and FAU.
    - Correlate the Lewis acidities of the metal substituted zeolites with their LUMO energies, and with the binding energies of NH_3.
    - Relate the hydrothermal stabilities of the metal substituted zeolites with their hydrolysis energies.

- Relate the Brønsted acidities of the metal substituted zeolites with their deprotonation energies.

3. Periodic DFT study of the reaction mechanisms for the ring opening of glucose and fructose with M-BEA, (M = Sn, Hf, Zr, Ti).
   - Find the preferential sites of substitution of Sn, Hf, Zr, and Ti in BEA.
   - Calculate the adsorption energies of glucose and fructose in M-BEA through the different oxygen atoms of the moelcules.
   - Calculate the complete reaction mechanism for the opening of the glucose and fructose rings on M-BEA.
   - Quantify the energy barriers in the reaction mechanism.
4. DFT study to unravel the catalytic properties of M-exchanged MFI, (M = Be, Co, Cu, Mg, Mn, Zn) for the conversion of methane and carbon dioxide to acetic acid.
   - Find the reaction barriers for the CH_4 dissociation on M-MFI.
   - Correlate the LUMO energies and electronegativity of M-MFI with the reaction barrier for CH_4 dissociation.
   - Quantify the charge transfer between CH_4 and the metal cation in the CH_4 dissociation.
   - Find the reaction barriers for the insertion of CO_2 and the protonation of the acetate.
   - Analyze how the co-adsorption of water in the system affects the desorption of acetic acid.

1.3 Scope of the dissertation

DFT analysis of metal-modified zeolites were conducted to understand and rationalize how the different active sites in zeolite frameworks affect the catalytic performance of these materials.

In chapter 2, a combination of quantum mechanical calculations and integrated quantum mechanics / molecular mechanics calculations along with a polarizable continuum model were used to determine the preferred substitution site of Sn-, Ti-, and Ge- metals in BEC and BEA zeolites, as well as the Lewis acidity and the hydrothermal stability of the metal substituted zeolites. Our results demonstrate that: (1) the most favorable substitution of Ti, Ge, and Sn in BEC is in the T1-site, (2) Ti-BEC has similar Lewis acidity to Sn-BEA, (3) the hydrolysis of Ge-BEC is energetically favorable when the Ge/Si ratio is 1/13, and (4) Ti-substituted zeolites show the highest hydrothermal stability of the zeolites studied.

In chapter 3, DFT with long-range corrections and ONIOM along with a polarizable-continuum model were used to analyze zeolites BEA, FAU, MFI, and BEC substituted with Sn and Ti. The preferential substitution sites for Ti and Sn in the different frameworks are reported. The Lewis acidities were measured through the NH_3 binding energies and through the charge transfer of NH_3 upon adsorption. The deprotonation energies of the open sites, which are proportional to the Brønsted acidities, and the hydrolysis energies are also reported. We analyze BEA with a single and a double Sn-substitution in order to compare the active sites with those obtained through two experimental methods commonly employed for the synthesis of Sn-BEA. Among the zeolites analyzed in this chapter, Sn-BEA with a double Sn-substitution has the highest Lewis acidity. The formation of open sites through the hydrolysis of Sn-BEA, Sn-FAU, and Ti-FAU is energetically favorable, but it is not favorable in MFI or Ti-BEA. Based on the deprotonation energies, the open sites of Sn-BEA have a strong Brønsted acidity, comparable to Al-BEA or Al-MFI. We also demonstrate that the VDW forces in the binding energies of NH_3 on MFI are more significant than in the other zeolite frameworks, and VDW forces decrease with increasing pore size.

In chapter 4, Periodic DFT with long range corrections (D3) were used to analyze the opening of the glucose and fructose rings with M-BEA (M = Sn, Ti, Zr, Hf) zeolites. We proposed a novel mechanism for the opening of these rings in one elementary step, which can be achieved on the closed sites of the zeolites. The preferential site of substitution of the metals in BEA were reported. The adsorption energies of glucose and fructose on M-BEA through the different oxygen atoms of the molecules were also reported. The transition state energies were calculated using the climbing nudge elastic band method. Among the zeolites that were studied, the lowest energy barrier for the opening of the glucose ring was obtained on Sn-BEA. On the other hand, Hf-BEA exhibited the lowest energy barrier for the opening of the fructose ring.

In chapter 5, DFT calculations with long-range corrections and ONIOM were used to analyze the reaction mechanism for the conversion of CO_2 and CH_4 into acetic acid with MFI zeolite exchanged with Be, Co, Cu, Mg, Mn, and Zn cations. Our results demonstrate that: (a) the highest reaction barrier on the reaction mechanism is CH_4 dissociation, and the transition state energy in that step is directly related to the energy of the lowest unoccupied molecular orbital and the electronegativity of the metal exchanged zeolites; (b) a charge transfer between CH_4 and the metal cation occurs simultaneously to CH_4 dissociation; (c) CO_2 insertion has a low energy barrier, and the protonation of the acetate species is spontaneous; (d) dispersion interactions are the main contributions to CH_4 adsorption energies, while in the rest of the steps of the reaction mechanism, the contribution of dispersion to the energies of reaction are almost negligible; (e) desorption of acetic acid could be promoted by the co-adsorption of water; (f) CH_4 dissociation on Cu-MFI has an apparent activation energy of 11.5 kcal/mol, and a forward rate constant of 1.1 s^{-1} at 398 K.

Chapter 6 summarizes the general conclusions for all the results obtained herein, provides some recommendations for future work related to these projects. Finally, the appendices A, B, C, and D, correspond to the supplementary information related to chapters 2, 3, 4, and 5, respectively.

1.4 REFERENCES

(1) Piccione, P.; Laberty, C.; Yang, S.; Camblor, M. A.; Navrotsky, A.; Davis, M. E. Thermochemistry of Pure-Silica Zeolites. *J. Phys. Chem. B* **2000**, *104*, 10001–10011.

(2) Moliner, M.; Román-Leshkov, Y.; Davis, M. E. Tin-Containing Zeolites Are Highly Active Catalysts for the Isomerization of Glucose in Water. *Proc. Natl. Acad. Sci. U. S. A.* **2010**, *107*, 6164–6168.

(3) Wolf, P.; Valla, M.; Rossini, A. J.; Comas-Vives, A.; Núñez-Zarur, F.; Malaman, B.; Lesage, A.; Emsley, L.; Copéret, C.; Hermans, I. NMR Signatures of the Active Sites in Sn-β Zeolite. *Angew. Chem. Int. Ed. Engl.* **2014**, *53*, 10179–10183.

(4) Bare, S. R.; Kelly, S. D.; Sinkler, W.; Low, J. J.; Modica, F. S.; Valencia, S.; Corma, A.; Nemeth, L. T. Uniform Catalytic Site in Sn-Beta-Zeolite Determined Using X-Ray Absorption Fine Structure. *J. Am. Chem. Soc.* **2005**, *127*, 12924–12932.

(5) Moliner, M.; Corma, A. Advances in the Synthesis of Titanosilicates: From the Medium Pore TS-1 Zeolite to Highly-Accessible Ordered Materials. *Microporous Mesoporous Mater.* **2014**, *189*, 31–40.

(6) Lee, F. Y.; Lv, L.; Su, F.; Liu, T.; Liu, Y.; Sow, C. H.; Zhao, X. S. Incorporation of Titanium into Polymorph C for Catalytic Epoxidation of Cyclohexene. *Microporous Mesoporous Mater.* **2009**, *124*, 36–41.

(7) Moliner, M.; Serna, P.; Catin, A.; Sastre, G.; Diaz-Cabanas, M.; Corma, A. Synthesis of the Ti-Silicate Form of BEC Polymorph of B-Zeolite Assisted by Molecular Modeling. *J. Phys. Chem. C* **2008**, *112*, 19547–19554.

(8) Shetty, S.; Pal, S.; Kanhere, D. G.; Goursot, A. Structural, Electronic, and Bonding Properties of Zeolite Sn-Beta: A Periodic Density Functional Theory Study. *Chem. a Eur. J.* **2006**, *12*, 518–523.

(9) Petkov, P. St.; Aleksandrov, H. a.; Valtchev, V.; Vayssilov, G. N. Framework Stability of Heteroatom-Substituted Forms of Extra-Large-Pore Ge-Silicate Molecular Sieves: The Case of ITQ-44. *Chem. Mater.* **2012**, *24*, 2509–2518.

(10) Shetty, S.; Kulkarni, B. S.; Kanhere, D. G.; Goursot, A.; Pal, S. A Comparative Study of Structural, Acidic and Hydrophilic Properties of Sn-BEA with Ti-BEA Using Periodic Density Functional Theory. *J. Phys. Chem. B* **2008**, *112*, 2573–2579.

(11) Kulkarni, B. S.; Krishnamurty, S.; Pal, S. Probing Lewis Acidity and Reactivity of Sn- and Ti-Beta Zeolite Using Industrially Important Moieties: A Periodic Density Functional Study. *J. Mol. Catal. A Chem.* **2010**, *329*, 36–43.

(12) Yang, G.; Pidko, E. a.; Hensen, E. J. M. Structure, Stability, and Lewis Acidity of Mono and Double Ti, Zr, and Sn Framework Substitutions in BEA Zeolites: A Periodic Density Functional Theory Study. *J. Phys. Chem. C* **2013**, *117*, 3976–3986.

(13) Yang, G.; Zhou, L.; Han, X. Lewis and Brönsted Acidic Sites in M4+-Doped Zeolites (M=Ti, Zr, Ge, Sn, Pb) as Well as Interactions with Probe Molecules: A DFT Study. *J. Mol. Catal. A Chem.* **2012**, *363–364*, 371–379.

(14) Boronat, M.; Corma, A.; Renz, M. Mechanism of the Meerwein-Ponndorf-Verley-Oppenauer (MPVO) Redox Equilibrium on Sn- and Zr-Beta Zeolite Catalysts. *J. Phys. Chem. B* **2006**, *110*, 21168–21174.

(15) Lew, C. M.; Rajabbeigi, N.; Tsapatsis, M. Tin-Containing Zeolite for the Isomerization of Cellulosic Sugars. *Microporous Mesoporous Mater.* **2012**, *153*, 55–58.

(16) Osmundsen, C. M.; Holm, M. S.; Dahl, S.; Taarning, E. Tin-Containing Silicates: Structure-Activity Relations. *Proc. R. Soc. A Math. Phys. Eng. Sci.* **2012**, *468*, 2000–2016.

(17) Yang, G.; Pidko, E. a.; Hensen, E. J. M. Structure, Stability, and Lewis Acidity of Mono and Double Ti, Zr, and Sn Framework Substitutions in BEA Zeolites: A Periodic Density Functional Theory Study. *J. Phys. Chem. C* **2013**, *117*, 3976–3986.

(18) Wells, D. H.; Delgass, W. N.; Thomson, K. T. Evidence of Defect-Promoted Reactivity for Epoxidation of Propylene in Titanosilicate (TS-1) Catalysts: A DFT Study. *J. Am. Chem. Soc.* **2004**, *126*, 2956–2962.

(19) Boronat, M.; Concepcion, P.; Corma, a; Renz, M.; Valencia, S. Determination of the Catalytically Active Oxidation Lewis Acid Sites in Sn-Beta Zeolites, and Their Optimisation by the Combination of Theoretical and Experimental Studies. *J. Catal.* **2005**, *234*, 111–118.

(20) Yang, G.; Zhou, L.; Han, X. Lewis and BrOnsted Acidic Sites in M 4+-Doped Zeolites (M = Ti, Zr, Ge, Sn, Pb) as Well as Interactions with Probe Molecules: A DFT Study. *J. Mol. Catal. A Chem.* **2012**, *363–364*, 371–379.

(21) Narsimhan, K.; Michaelis, V. K.; Mathies, G.; Gunther, W. R.; Griffin, R. G.; Román-Leshkov, Y. Methane to Acetic Acid over Cu-Exchanged Zeolites: Mechanistic Insights from a Site-Specific Carbonylation Reaction. *J. Am. Chem. Soc.* **2015**, *137*, 1825–1832.

(22) Wu, J.; Yu, S.; Wang, W. D.; Fan, Y.; Bai, S.; Zhang, C.; Gao, Q.; Huang, J.; Wang, W. Mechanistic Insight into the Formation of Acetic Acid from the Direct Conversion of Methane and Carbon Dioxide on Zinc-Modified H−ZSM-5 Zeolite. *J. Am. Chem. Soc.* **2013**, *135*, 13567–13573.

(23) Benco, L. Electronic Structure of Zn^{+}-Modified Zeolite: A Density Functional Theory Study of Ferrierite. *J. Phys. Chem. C* **2016**, *120*, 6031–6038.

(24) Zhao, Z.-J.; Kulkarni, A.; Vilella, L.; Norskov, J. K.; Studt, F. Theoretical Insights into the Selective Oxidation of Methane to Methanol in Copper-Exchanged Mordenite. *ACS Catal.* **2016**, *6*, 3760–3766.

(25) Kulkarni, A. R.; Zhao, Z.; Siahrostami, S.; Nørskov, J. K.; Studt, F. Monocopper Active Site for Partial Methane Oxidation in Cu- Exchanged 8MR Zeolites. *ACS Catal.* **2016**, *6*, 6531–6536.

(26) Panjan, W.; Sirijaraensre, J.; Warakulwit, C.; Pantu, P.; Limtrakul, J. The Conversion of CO2 and CH4 to Acetic Acid over the Au-Exchanged ZSM-5 Catalyst : A Density Functional Theory Study. *Phys. Chem. Chem. Phys.* **2012**, *14*, 16588–16594.

(27) Wettstein, S. G.; Alonso, D. M.; Gürbüz, E. I.; Dumesic, J. a. A Roadmap for Conversion of Lignocellulosic Biomass to Chemicals and Fuels. *Curr. Opin. Chem. Eng.* **2012**, *1*, 218–224.

(28) Roman, Y.; Davis, M. E. Activation of Carbonyl-Containing Molecules with Solid Lewis Acids in Aqueous Media. *ACS Catal.* **2011**, *1*, 1566–1580.

(29) Holm, M. S.; Saravanamurugan, S.; Taarning, E. Conversion of Sugars to Lactic Acid Derivatives Using Heterogeneous Zeotype Catalysts. *Science.* **2010**, *328*, 602–605.

(30) Dong, W.; Shen, Z.; Peng, B.; Gu, M.; Zhou, X.; Xiang, B.; Zhang, Y. Selective Chemical Conversion of Sugars in Aqueous Solutions without Alkali to Lactic Acid Over a Zn-Sn-Beta Lewis Acid-Base Catalyst. *Sci. Rep.* **2016**, *6*, 26713.

(31) Lew, C. M.; Rajabbeigi, N.; Tsapatsis, M. Tin-Containing Zeolite for the Isomerization of Cellulosic Sugars. *Microporous Mesoporous Mater.* **2012**, *153*, 55–58.

(32) Bui, L.; Luo, H.; Gunther, W. R.; Román-Leshkov, Y. Domino Reaction Catalyzed by Zeolites with Brønsted and Lewis Acid Sites for the Production of γ-Valerolactone from Furfural. *Angew. Chem. Int. Ed. Engl.* **2013**, *52*, 8022–8025.

(33) West, R. M.; Holm, M. S.; Saravanamurugan, S.; Xiong, J.; Beversdorf, Z.; Taarning, E.; Christensen, C. H. Zeolite H-USY for the Production of Lactic Acid and Methyl Lactate from C3-Sugars. *J. Catal.* **2010**, *269*, 122–130.

(34) Gunther, W. R.; Michaelis, V. K.; Griffin, R. G.; Roman-Leshkov, Y. Interrogating the Lewis Acidity of Metal Sites in Beta Zeolites With 15N Pyridine Adsorption Coupled With MAS NMR Spectroscopy. *J. Phys. Chem. C* **2016**, *120*, 28533–28544.

(35) Li, H.; Wang, J.; Zhou, D.; Tian, D.; Shi, C.; Müller, U.; Feyen, M.; Gies, H.; Xiao, F.; Vos, D. De; et al. Microporous and Mesoporous Materials Structural Stability and Lewis Acidity of Tetravalent Ti , Sn , or Zr-Linked Interlayer-Expanded Zeolite COE-4 : A DFT Study. *Microporous Mesoporous Mater.* **2015**, *218*, 160–166.

(36) Waal, J. C. Van Der; Rigutto, M. S.; Bekkum, H. Van. Zeolite Titanium Beta as a Selective Catalyst in the Epoxidation of Bulky Alkenes. *Appl. Catal. A Gen.* **1998**, *167*, 331–342.

(37) Zeolite Titanium Beta : A Versatile Epoxidation Catalyst . Solvent Effects. *J. Mol. Catal. A Chem.* **1997**, *124*, 1997.

(38) Boronat, M.; Corma, A.; Renz, M.; Viruela, P. M. Predicting the Activity of Single Isolated Lewis Acid Sites in Solid Catalysts. *Chem. a Eur. J.* **2006**, *12*, 7067–7077.

(39) Wolf, P.; Hammond, C.; Conrad, S.; Hermans, I. Post-Synthetic Preparation of Sn-, Ti- and Zr-Beta: A Facile Route to Water Tolerant, Highly Active Lewis Acidic Zeolites. *Dalt. Trans.* **2014**, *43*, 4514–4519.

(40) Vyver, S. Van De; Odermatt, C.; Romero, K.; Prasomsri, T.; Roma, Y. Solid Lewis Acids Catalyze the Carbon − Carbon Coupling between Carbohydrates and Formaldehyde. *ACS Catal.* **2015**, *5*, 972–977.

(41) Luo, H. Y.; Consoli, D. F.; Gunther, W. R.; Román-leshkov, Y. Investigation of the Reaction Kinetics of Isolated Lewis Acid Sites in Beta Zeolites for the Meerwein – Ponndorf – Verley Reduction of Methyl Levulinate to c -Valerolactone. *J. Catal.* **2014**, *320*, 198–207.

(42) Sastre, G.; Corma, A. Relation between Structure and Lewis Acidity of Ti-Beta and TS-1 Zeolites : A Quantum-Chemical Study. *Chem. Phys. Lett.* **1999**, *302*, 447–753.

(43) Chheda, J. N.; Huber, G. W.; Dumesic, J. A. Liquid-Phase Catalytic Processing of Biomass-Derived Oxygenated Hydrocarbons to Fuels and Chemicals Angewandte. *Angew. Chem. Int. Ed. Engl* **2007**, *46*, 7164–7183.

2 CHAPTER - A DFT STUDY OF THE LEWIS ACIDITIES AND RELATIVE HYDROTHERMAL STABILITIES OF BEC AND BEA ZEOLITES SUBSTITUTED WITH TI, SN AND GE

2.1 INTRODUCTION

The substitution of zeolite materials with heteroatoms, such as titanium (Ti) or tin (Sn) in framework positions changes drastically the catalytic properties of the zeolites. These catalytic properties, together with their high hydrothermal stability, have allowed the application of zeolites in different types of reactions. Of particular interest are the reactions involving the transformation of biomass derived molecules to high value chemicals. In many of these reactions water takes a central role. Water can either serve as a solvent, reactant, or product of the reaction (e.g., the production of 5-hydroxymethyl furfural and furfural from fructose and xylose, respectively).[1] Hence, adequate catalysts for these reactions must have high hydrothermal stability. A well-known example of this type of catalyst is the Beta zeolite substituted with Sn or Ti that exhibits high catalytic activity in the isomerization of glucose to fructose following an Meerwein-Ponndorf-Verley type mechanism with high stability in liquid water.[2]

BEA is a highly faulted intergrowth of two polymorphs (Polymorphs A and B).[3] The ratio between polymorph A and B is about 50:50,[4] and the size of ordered interlayer stacking sequences is less than 12 nm, with five repetitions of the unit cell of polymorph A along the C axis.[5,6] The incorporation of Sn in BEA has been reported up to 10 wt%, however, it is at low loadings (0.5 wt%) that high turn-over-frequencies (TOF) are observed.[7] The reduction in the TOF for loadings above 0.5 wt% could be due to the incorporation of Sn in extra-framework positions as tin oxide (SnO_2).[7] Furthermore, interlayer stacking faults present in BEA affect the pore structure and potentially the diffusion of molecules within the pores.[8] Moreover, the interlayer stacking in BEA

could be one of the factors limiting the amount of Sn that can be incorporated in the BEA framework.[4]

Polymorphism C (BEC) is another polymorphism of the zeolite Beta that can be synthesized as a pure and crystalline structure. BEC has three dimensional pore topology, all three with twelve-membered ring channels.[9] BEC, owing to its ordered and crystalline structure, could overcome the diffusion problems exhibited in BEA. However, only few studies have been reported in the literature on the use of BEC in catalysis.[8,10,11] Recently, Corma and coworkers demonstrated that BEC functionalized with titanium (Ti-BEC) performed better in terms of activity and selectivity than BEA functionalized with titanium (Ti-BEA) when cyclic compounds as cyclo-octene were tested for epoxidation reactions.[8] BEC was synthesized for the first time as a germanium-silicate, showing poor hydrothermal stability,[9] but after, BEC has been synthesized as a pure silicate with a much higher hydrothermal stalibility.[12]

Density functional theory (DFT) calculations have been widely used to study the incorporation of metals in zeolites. Periodic boundary conditions have been applied to different frameworks, such as Ti-BEA, Sn-BEA, Zr-BEA, Ge-ITQ44 and Ti-ITQ44.[13-17] Cluster models have been used to study zeolites, such as Zr-MFI, Ti-MFI, Ge-MFI, Sn-MFI, Sn-BEA, Zr-BEA and Pb-MFI.[18, 19] These studies have reported the preferential location of the metals in the zeolites, and most have used the electronic properties of the zeolites to determine the Lewis and Brønsted acidities. However, to the best of our knowledge, studies have not reported the electronic properties of metal substituted BEC. In this study, we analyzed BEC zeolites functionalized with Sn, Ti or Ge, and compared the properties of these materials with the well-known Sn-BEA and Ti-BEA zeolites. We have quantified how the properties of the metal atoms (Ge, Ti, and Sn) in the zeolite framework

change upon hydrolysis. Finally, we have analyzed the effect of water on the zeolite structure simulating the presence of solvent using a polarizable continuum model (PCM).

We validated the method used for the calculation of the hydrothermal stability with the experimental results obtained for Si-BEC and Ge- BEC. However, hydrothermal stabilities for BEC functionalized with Sn and Ti are not reported in the literature. This work demonstrates that Ti-BEC should have a high hydrothermal stability and Lewis Acidity.

2.2 METHODOLOGY

Three exchange correlation functionals (B3LYP[20], B3PW91[21] and ωB97XD[22]) were systematically analyzed, to select the one that best describes the properties of the materials. The NMR shifts of Si-BEC, the optimized geometries of the zeolites and various vibrational frequencies were obtained with the 3 functionals. (See Appendix A.) Results were compared with experimental data available in the literature. The three functionals accurately describe the properties of the zeolites. Errors above 10% were only obtained on the NMR shifts calculated using B3LYP. Since the ωB97XD functional best described the properties of the zeolites and takes into consideration the dispersion forces, this functional was used for subsequent calculations.

2.2.1 Preferential location of Ge, Sn and Ti in BEC and Ti in BEA

DFT calculations were used to locate preferred substitution sites for zeolitic materials that have not been fully characterized, such as BEC substituted with Sn and Ti and BEA substituted with Ti. Preferred substitution site for Ge in BEC was also calculated in order to corroborate that the preferred substitution of Ge is in the T1 site.[23] Clusters used for the calculations of Si-BEC, Ge-

BEC, Sn-BEC and Ti-BEC centered in each T-site and Ti-BEA centered in T1 and T2 are shown in Figure 2-1. Clusters of Ti-BEA centered in T3 to T9 are shown in Figure A-4.

The cluster models were obtained from the experimental structures of BEC[9] reported by the literature and BEA reported by the International Zeolite Association (IZA).[24] The clusters were obtained cutting the periodic structure and hydrogen atoms were placed on the terminal atoms of the model where bonds were truncated. These hydrogen atoms were aligned along the truncated bond. Their positions were calculated with the position vector of the atoms involved in the bond. The Si-H bond distances were fixed at 1.5000 Å. This approach has been widely used for the computational study of different zeolite structures, such as MFI[18], BEA[19], TS1[25] and Faujasite.[26]

The results were obtained using a mix of basis sets: 6-31+g** (Si, O, H), LANL2DZ[27] (Ti, Ge) and MWB46[28] (Sn) along with the ωB97XD functional. Geometries and energies were obtained by performing geometry optimizations, while maintaining the coordinates of the hydrogen atoms fixed. The E_{LUMO}'s and the Hardness were calculated using a larger basis set (6-311+G**) for the Si, O and H atoms. As shown in Table A- 3, no significant differences were obtained for these electronic properties when the size of the basis set increases.

For Ti-BEC and Ti-BEA, we analyzed the three lowest spin states of the system, and our calculations demonstrate that the singlet state ($S = 0$) is the lowest energy state. Hence, the results presented herein for Ti-BEA and Ti-BEC correspond to the single spin state. Energy values for the three lowest spin states of Ti-BEC and Ti-BEA are shown in Table A-4 and Table A-5**,** respectively. Partial atomic charges were obtained with the natural bond orbital (NBO) population analysis[29]. All calculations were carried out with the Gaussian 09 program package.[30]

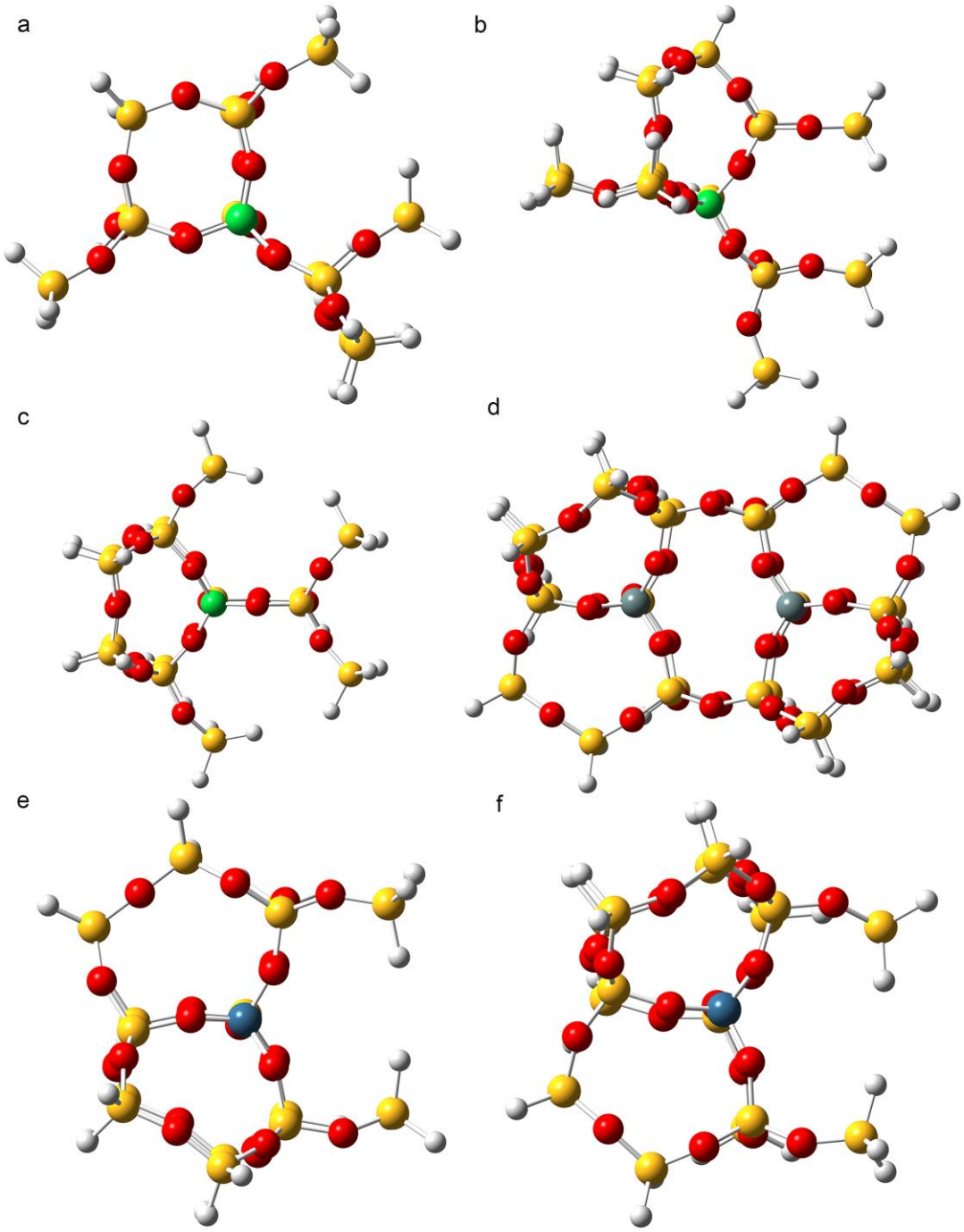

Figure 2-1. Clusters used for the DFT calculations of M-BEC, Sn-BEA and Ti-BEA. a.) 53-atom M-BEC cluster centered in T1 b.) 65-atom M-BEC cluster centered in T2 c.) 60-atom M-BEC cluster centered in T3. d.) 98-atoms Sn-BEA cluster centered in a double substitution in T2 sites. e.) 59-atom Ti-BEA cluster centered in T1 f.) 59-atom Ti-BEA cluster centered in T2. Color legend: yellow = Si; red = O; white = H; green = metal atom (M=Ge, Sn, Ti) centered on the T site in BEC; gray= Sn; blue=Ti.

2.2.2 Hydrolysis energies and Lewis acidity of metal substituted zeolites

Preferential locations of Ge, Sn and Ti in BEC and Ti in BEA were calculated in the previous section, but preferential location of Sn in BEA was obtained in the literature.[4] Bare and coworkers demonstrated the substitution of Sn in zeolite Beta is a double-paired substitution in the T2 sites and that this functionalization exhibits the best catalytic activity.[4,31] The cluster of Sn-BEA is shown in Figure 2-1.d Hydrolysis energies of substituted zeolites (Ge-BEC, Ti-BEC, Ti-BEA, Sn-BEC and Sn-BEA) were calculated using a Polarizable Continuum Model (PCM) to study solvent effects on the energies of the stable intermediates. For these calculations, water was used as the solvent, which has a dielectric constant of 78.3553. PCM has proven to reproduce properties of structures similar to the ones in this study with low errors in energies of reaction.[32,33]

ONIOM, which is a combined quantum mechanics (QM) / molecular mechanics (MM) method, was used to incorporate the effect of the surrounding zeolite framework. For these calculations, two layers linked via mechanical embedding were used. The level of theory described in Section 2.1 was used for the QM layer, and universal force field (UFF) was used for the MM layer. For the metal-substituted BEC, the inner layer consisted of 56 atoms. Three different cluster sizes were analyzed to assess different metal (M) to Si ratios, (M = Ge, Sn or Ti). Calculations were carried out with outer layers consisting of 61, 172 and 338 atoms, which correspond to M/Si ratios of 1/32, 1/64 and 1/114, respectively. For Ti-BEA, the inner layer consisted of 64 atoms and the outer layer consisted of 57, 155 and 317 atoms, which correspond to Ti/Si ratios of 1/33, 1/62 and 1/110, respectively. For Sn-BEA, the inner layer consisted of 104 atoms and the outer layer consisted of 76, 196 and 406 atoms, which correspond to Sn/Si ratios of 2/50, 2/86 and 2/148, respectively. The ONIOM clusters used to analyze M-BEC, Ti-BEA and Sn-BEA are shown in Figure 2-2, Figure 2-3, and Figure 2-4, respectively.

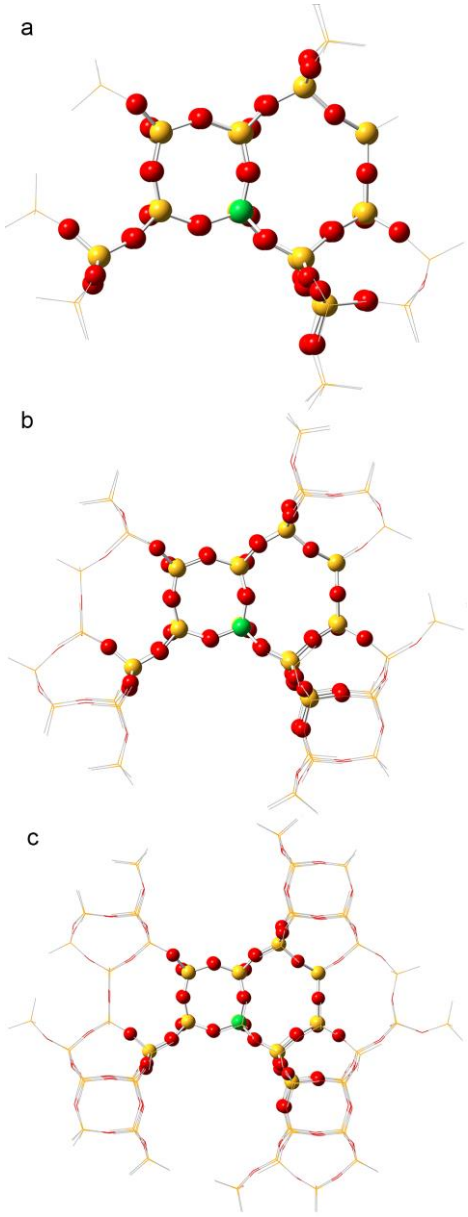

Figure 2-2. ONIOM clusters of M-BEC with different M/Si ratios. a.) 117-atoms cluster with an M/Si ratio of 1/32, b.) 228-atoms cluster with an M/Si ratio of 1/64 and c.) 394-atoms cluster with an M/Si ratio of 1/114. M corresponds to the metal atom, Ge, Sn or Ti.

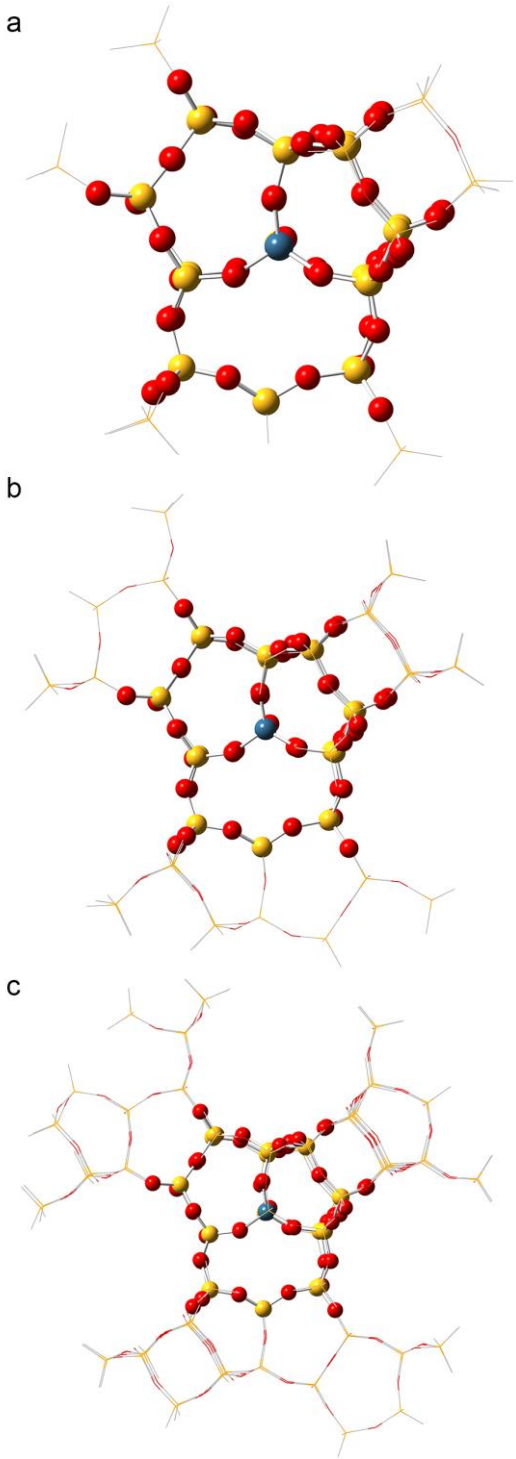

Figure 2-3. ONIOM clusters of Ti-BEA with different Ti/Si ratios a.) 121-atoms cluster with a Ti/Si ratio of 1/33, b.) 219-atoms cluster with a Ti/Si ratio of 1/62 and c.) 381-atoms cluster with a Ti/Si ratio of 1/110.

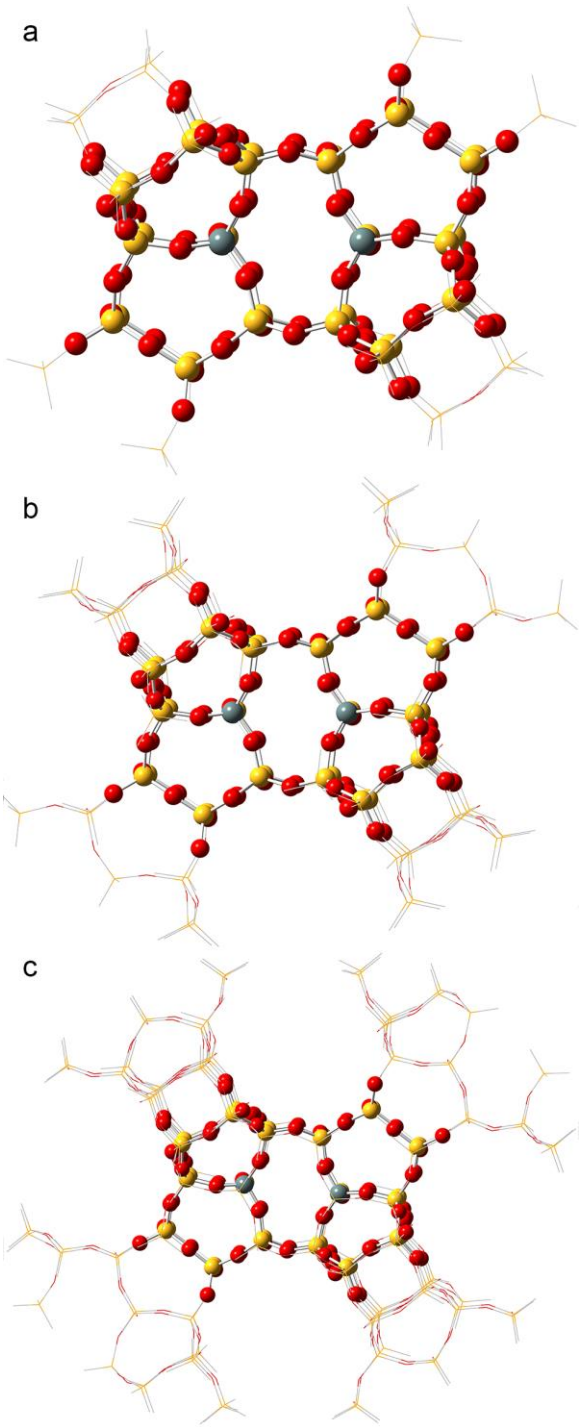

Figure 2-4. ONIOM clusters of Sn-BEA with different Sn/Si ratios a.)180-atoms cluster with a Sn/Si ratio of 2/50, b.) 300-atoms cluster with a Sn/Si ratio of 2/86 and c.) 510-atoms cluster with a Sn/Si ratio of 2/148.

2.3 RESULTS AND DISCUSSION

2.3.1 Preferential location of Ge, Sn and Ti in BEC and Ti in BEA

The energy of substituting a Si atom by Ge, Sn or Ti in the three different crystallographic T-sites of BEC was calculated based on the reaction presented in Scheme 2-1.

Scheme 2-1. Reaction describing the metal substitution into the zeolite framework.

$$Zeo[Si] + M(OH)_4 \quad \rightarrow \quad Zeo[M] + Si\ (OH)_4$$

$$\mathrm{E_{rx}} = \mathrm{E^{e}_{Zeo[M]}} + \mathrm{E^{e}_{Si\ (OH)_4}} - \mathrm{E^{e}_{Zeo[M]}} - \mathrm{E^{e}_{Zeo[M]}} \qquad \textbf{(2-1)}$$

Table A-6 and Figure 2-5 summarize the electronic energies of reaction obtained for the substitution of each heteroatom in each T-site according to the Equation 2-1. We are aware that this reaction energy does not provide an absolute measure of the substitution preference of the heteroatoms in the zeolite since this energy depends on the stability of the different species ($Si(OH)_4$, $Ge(OH)_4$, $Ti(OH)_4$ and $Sn(OH)_4$). However, this method provides an estimate of the most favorable substitution site of each heteroatom among the three different T-sites. Our results indicate that the T1-site is the location that yields the lowest energy for the substitution of the three heteroatoms studied. The results for Ge are in good agreement with the work of Corma and coworker, which demonstrate that the most favorable substitution of Ge in BEC is in the T1-site.[23] Based on our results, Ti and Sn are also likely to be substituted in the T1-site.

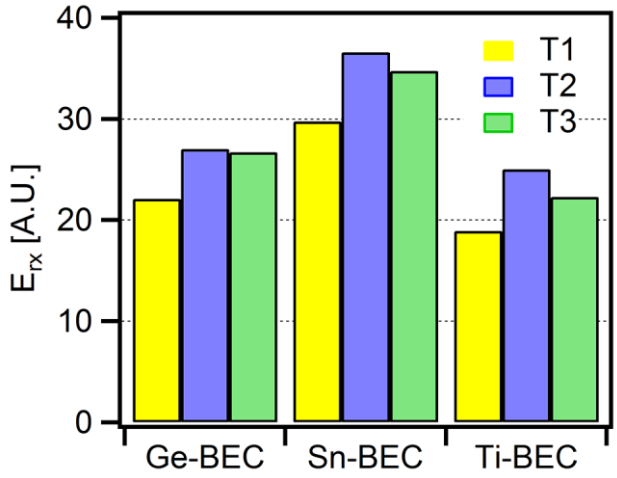

Figure 2-5. Preferential location of the heteroatoms (Ge,Sn, Ti) in BEC.

The preferential location of Ti in BEA was determined as shown in Table A- 7. The energies obtained through the sites T1 to T6 are close, but the lowest energy was obtained for the sites T1 (14.84 kcal/mol) and T2 (14.89 kcal/mol). These results are in good agreement with those reported by Yang and coworkers.[17] In their work, they demonstrated that the preferred site for the substitution of Ti in BEA is T2, followed closely by T1.[17] Hence, both DFT methods suggest that the preferential site for the substitution of Ti in BEA is at either the T2 or T1 site.

Figure 2-6 and Table A-8 to Table A-10 show the LUMO energies, the hardness (η) and the NBO charges of the metal in Ge-BEC, Sn-BEC and Ti-BEC. The strength of a Lewis acid is commonly related to the LUMO energy, such that the lower the LUMO energy of a molecule the easier it interacts with a Lewis base.[18] Sastre and Corma carried out *ab initio* calculations on TS-1 and Ti- BEA zeolites to unravel the electronic properties of the Ti atoms on both systems that manifest in different catalytic properties.[34] They demonstrated that the Lewis acidity of these materials was indeed correlated to the LUMO energies of the zeolite clusters that they analyzed. Based on the LUMO energies shown in Figure 2-6.a, the Lewis acidity of the metal substituted BEC decreases according the following trend: Ti-BEC > Sn-BEC > Ge-BEC. Substitution in T1

site corresponds to the substitution with the lowest LUMO energy for the three heteroatoms studied, therefore, substitution in T1 represent the most favorable substitution, as well as the substitution with the highest Lewis acidity.

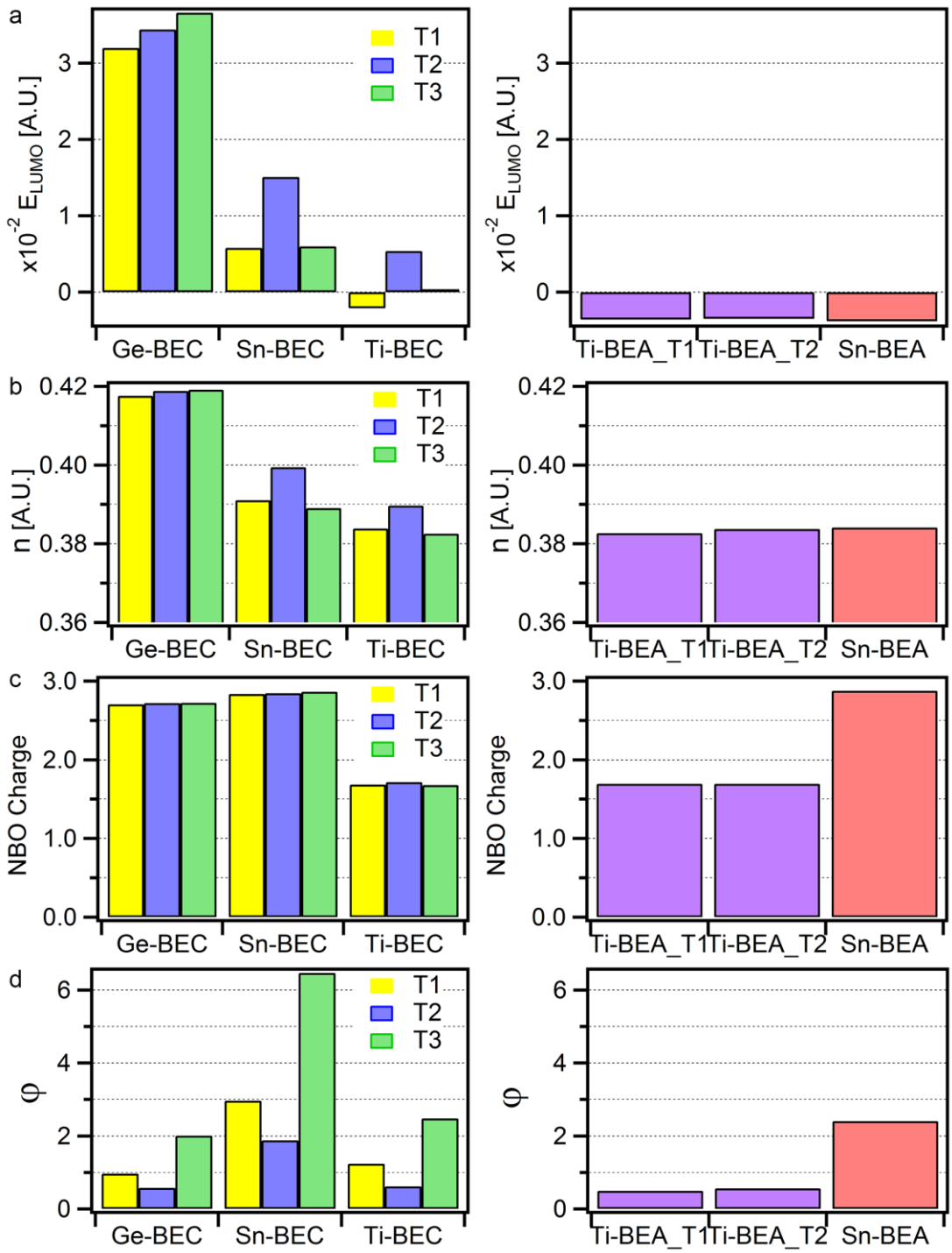

Figure 2-6. Electronic properties and local deformation of M-BEC (M = Ge, Sn, Ti), Sn-BEA and Ti-BEA obtained in vacuum. a.) LUMO energies, b.) hardness, c.) NBO charges of the metal atom, d.) local structural perturbation at the T-site.

Another descriptor that is commonly employed in the literature to assess the catalytic activity is the hardness.[16] The hardness could be approximated as the energy gap between the two frontier orbitals HOMO and LUMO.[35] As the hardness increases, the zeolite becomes a harder acid. As it is shown in Figure 2-6.b, the "hard acid" character of the substituted BEC decreases with the following trend: Ge-BEC > Sn-BEC > Ti-BEC.

It is also shown in Figure 2-6.c that the charge of the metal atom in BEC is not affected by the substitution site. The charges of the metals in Ge-BEC and Sn-BEC are similar, and Ti has the lowest NBO charge of the three systems studied. A hard acid has an acceptor atom of high positive charge, while a soft acid has an acceptor atom of low positive charge.[35] Based on the NBO charges and the hardness, Ti-BEC would be a soft acid, while Ge-BEC and Sn-BEC would be a hard acid. In terms of chemical reactivity, soft molecules will be more reactive than hard molecules for unimolecular reactions such as isomerization.[35] These results suggest that Ti-BEC might be an active catalyst for reactions involving soft bases, such as the isomerization of glucose to fructose.

The local structural perturbation at the T-site can be calculated by the change of [TO_4] from a regular tetrahedron using the mean square deviation parameter (θ) as defined in Equation 2-2.[36,37]

$$\theta = \sqrt{\frac{1}{6}\sum_{i=1}^{6}(\alpha_i - \bar{\alpha})^2} \qquad (2\text{-}2)$$

In this equation, α_i represents the ith θ(O-T-O) angle and $\bar{\alpha}$ is the average of the six θ(O-T-O) angles. The mean square deviation parameter is not a direct measure of the distortion caused by the incorporation of the heteroatoms in the framework positions of the zeolites. A normalization of θ for each functionalized zeolite, θ_M, must be done with respect to the value of θ in a pure zeolite (θ_{Si}) as described in Equation 2-3.

$$\varphi = \frac{(\theta_M - \theta_{Si})}{\theta_{Si}} \qquad \textbf{(2-3)}$$

The normalization parameters (φ) for each substitution of BEC are shown in Figure 2-6.d (Table A-11). The substitution in T2 for all the heteroatoms results in the lowest structural perturbation. The local structural perturbation parameter φ also indicates that the incorporation of Sn in framework positions causes more distortion in the structure than the incorporation of Ti or Ge, owing to its larger radius.

Figure 2-6 also allows comparing the properties obtained for M-BEC with the properties obtained for Ti-BEA and Sn-BEA in the preferred site of substitution (T1 and T2 for Ti-BEA and the double substitution in T2 for Sn-BEA). Based on the LUMO energies, the Lewis acidity of Ti-BEC in the preferred site of substitution is comparable to that of Sn-BEA and Ti-BEA, and perhaps might show comparable catalytic properties. The incorporation of Sn in framework positions in BEA and BEC causes significantly more distortions in the structure than the incorporation of Ge or Ti in the zeolites, indicating that the incorporation of Sn in the zeolite could be more difficult to achieve than the incorporation of Ti.

2.3.2 Hydrolysis energies and Lewis Acidities of metal substituted zeolites

In any system, the presence of a hydroxyl group coordinated to a metal atom produces a material with a high affinity to water molecules. Hence, the analysis of the energies of hydrolysis can be used to estimate how feasible it would be for the metal-substituted zeolites to react with water. Hydrolysis energies of the different substituted zeolites were calculated through the electronic energies of reaction of the structure with water, as illustrated in Scheme 2-2.

Scheme 2-2. Hydrolysis reaction of the metal substituted zeolite.

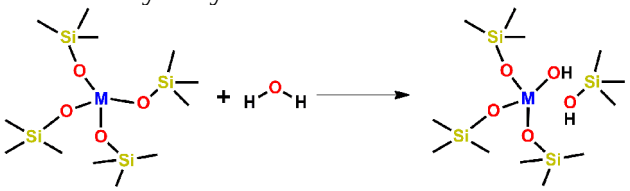

Upon hydrolysis, the metal atom ends up coordinated to a hydroxyl group. In M-BEC, and Ti-BEA the hydrolysis can occur through four different bonds. In Sn-BEA, there are eight different bonds that could be broken through the hydrolysis. The figures and tables that illustrate the oxygen atoms that might be involved in the hydrolysis, and the hydrolysis energies associated with the breaking of each of the oxygen atoms are in the Appendix A (Figure A- 5 to Figure A-7 and Table A-12 to Table A-14). In M-BEC, the lowest hydrolysis energies were obtained by breaking the bond formed with the same oxygen atom on the four structures analyzed.

Figure 2-7 and Table A-15 compare some of the electronic properties of the hydrolyzed and the non-hydrolyzed zeolites. The properties for the hydrolyzed zeolites shown in Figure 2-7 were obtained for the zeolite hydrolyzed through the weakest bond. As it is shown in Figure 2-7.a, the LUMO energies of Si-BEC, Ge-BEC, Sn-BEA, Ti-BEC and Ti-BEA decrease when they are hydrolyzed, while the LUMO energy of Sn-BEC increases when it is hydrolyzed. Thus, the addition of defects through the hydrolysis in the zeolite increases the Lewis acidity in all the zeolites analyzed, except in Sn-BEC. The LUMO energies of the hydrolyzed Ti-BEC and Ti-BEA are even lower than the LUMO energy of the hydrolyzed Sn-BEA. Hence, the addition of defects to the structure through the hydrolysis allows Ti-BEC and Ti-BEA to have a higher Lewis acidity than Sn-BEA. Figure 2-8 depicts the LUMO surfaces for the hydrolyzed and non hydrolyzed zeolites. For each of the systems that were analyzed, the LUMO surface is mainly located close to the metal atom, even when the system is hydrolyzed.

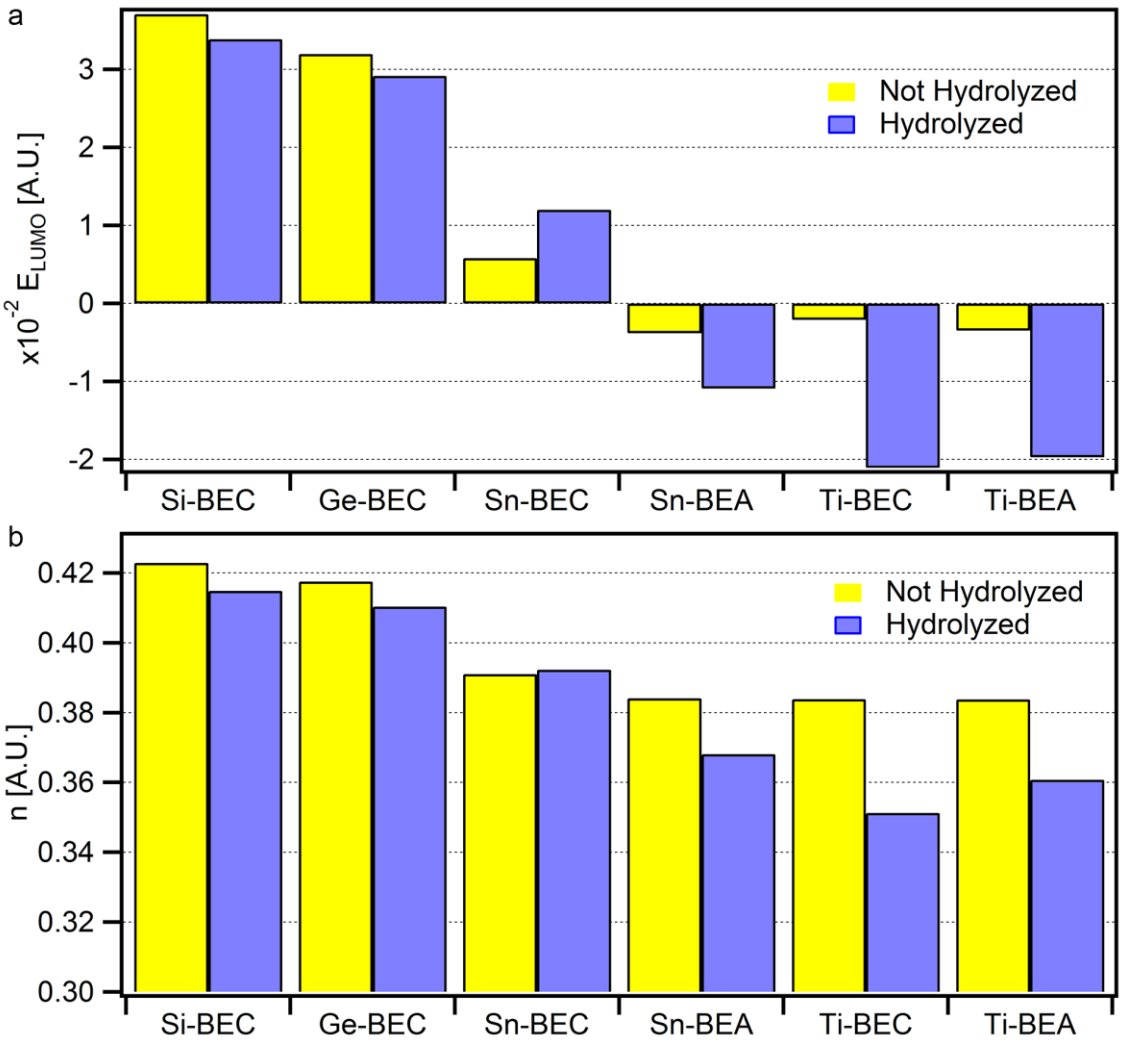

Figure 2-7. Comparison of electronic properties of the hydrolyzed and non-hydrolyzed M-BEC (M = Si, Ge, Sn, Ti), Sn-BEA and Ti-BEA obtained in vacuum. a.) LUMO energies, b.) Hardness.

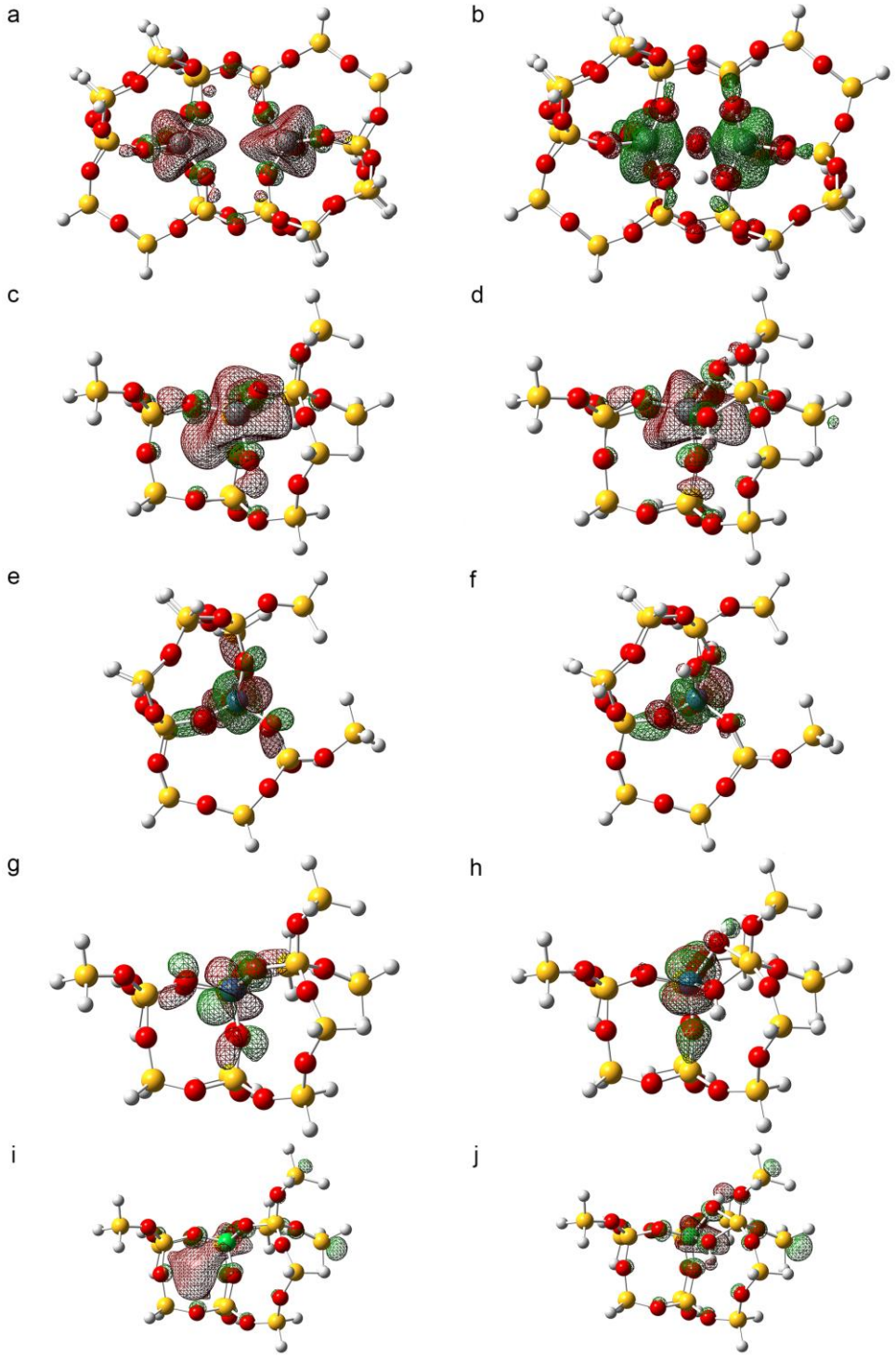

Figure 2-8. LUMO diagrams of a.) Sn-BEA, b.) Sn-BEA_OH, c.) Sn-BEC, d.) Sn-BEC_OH, e.) Ti-BEA, f.) Ti-BEA_OH, g.) Ti-BEC, h.) Ti-BEC_OH, i.) Ge-BEC, j.) Ge-BEC_OH

It can also be observed in Figure 2-7.b that the hardness of Si-BEC, Ge-BEC, Sn-BEA, Ti-BEC and Ti-BEA decrease when they are hydrolyzed. However, the hardness of Sn-BEC increases when it is hydrolyzed. Table A-15 shows the NBO charges for the heteroatoms in the zeolites. Two values of NBO charges are shown for Sn-BEA, that correspond to the two Sn atoms substituted in Sn-BEA according to Figure A-7. The hydrolysis of the metal substituted zeolites does not affect significantly the NBO charges in the metals. The Ti atom in Ti-BEC and in Ti-BEA has the lowest charge, even when it is hydrolyzed, confirming the soft acid character of Ti-BEC and Ti-BEA.

We used the integrated QM/MM scheme as implemented in ONIOM to analyze the effect of the solvent and metal / silicon (M/Si) ratios in the hydrolysis energies of the metal substituted zeolites. Local structural perturbation parameters for the non-hydrolyzed zeolites with different M/Si ratios are shown in Figure 2-9 (Table A-17). The parameter φ was calculated in relation with the θ_{Si} parameter obtained for the biggest cluster of the pure zeolite. The deformation of the structure decreases according to the following trend Sn-BEA > Sn-BEC > Ti-BEC > Ti-BEA > Ge-BEC. The highest deformations were obtained for the zeolites functionalized with Sn, as it has the biggest radius of the metal atoms analyzed in this work. For Ge-BEC and Sn-BEC, as the metal composition decreases, the local structure perturbation decreases. The decrease in the metal composition in the zeolite allows the zeolite become a more stable structure, with less deformation in its structure after the incorporation of the metal. On the other hand, Sn-BEA, Ti-BEC and Ti-BEA do not show changes in the structural perturbation of its configuration for the different M/Si ratios. The insertion of Ti in BEA or BEC results in a lower structure deformation than the insertion of Sn in BEA or BEC. These results suggest that the zeolites could be functionalized in higher

proportions with Ti than Sn. The feasibility to incorporate higher amounts of Ti in the zeolites than Sn would give zeolites more active sites and increased Lewis acidity.

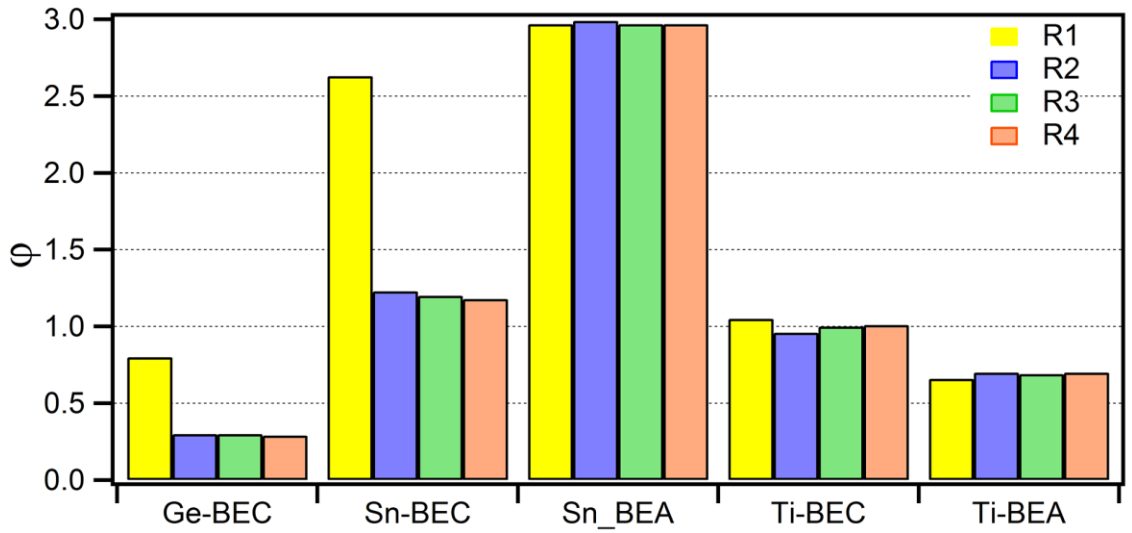

Figure 2-9. Local structural perturbation of M-BEC (M = Ge, Sn, Ti), Sn-BEA and Ti-BEA for different metal composition. For M-BEC, the M/Si ratios are R1=1/13, R2=1/32, R3=1/64, R4=1/114; for Sn-BEA the Sn/Si ratios are R1=2/30, R2=2/50, R3=2/86, R4=2/148; for Ti-BEA the Ti/Si ratios are R1=1/15, R2=1/33, R3=1/62, R4=1/110.

In order to take into account the effect of the solvent on the properties of the zeolites, single points of the optimized geometries obtained for the different M/Si ratios were carried out using PCM. Figure A-8 shows a scheme of the surface cavity used for the PCM calculations for the hydrolyzed Ge-BEC. The use of ONIOM and PCM allow us to take into consideration the metal composition, as well as, the solvent effect on the properties of the zeolites.

Figure 2-10 (Table A-18) shows the electronic energies of hydrolysis of M-BEC, Sn-BEA and Ti-BEA using a PCM for different M/Si ratios. The hydrolysis energies for the highest M/Si ratio (1/13 in M-BEC, 2/30 in Sn-BEA and 1/15 in Ti-BEA) decrease with the following trend: Si-BEC > Ti-BEC ≈ Ti-BEA > Sn-BEC > Sn-BEA > Ge-BEC. However, for lower M/Si relations, the hydrolysis energy of Ge-BEC changes drastically from a negative to a positive value. For the other M/Si ratios, the hydrolysis energies decrease with the following trend: Si-BEC > Ge-BEC >

Ti-BEC ≈ Ti-BEA > Sn-BEC > Sn-BEA. These results are in good agreement with various reports in the literature.[38,39,40] Our results demonstrate that Si-BEC exhibits a high resistance to be hydrolyzed due to the crystallinity of its zeolitic walls in agreement with Corma and Davis.[38] Our calculations also demonstrate that Ti-BEC and Ti-BEA have a higher hydrolysis energy compared to Sn-BEC and Sn-BEA, in agreement with observations by Corma and coworkers on metal substituted BEA with Ti that exhibit higher hydrothermal stability than those functionalized with Sn.[40] Finally, our results indicate that Ge-BEC exhibits a drastic change in the hydrolysis energy on systems with Ge/Si ratios of 1/32 or less (14 kcal/mol) when compared to the systems with a higher Ge/Si ratio (-39.5 kcal/mol). These results are consistent with experimental work that reported that Ge substituted zeolites lose its structure when interacting with water when the Ge/Si ratio is lower than 1/20.[39,41] Hydrolysis energies calculated in vacuum for M-BEC, Sn-BEA and Ti-BEA are tabulated in the Appendix A (Table A-16).

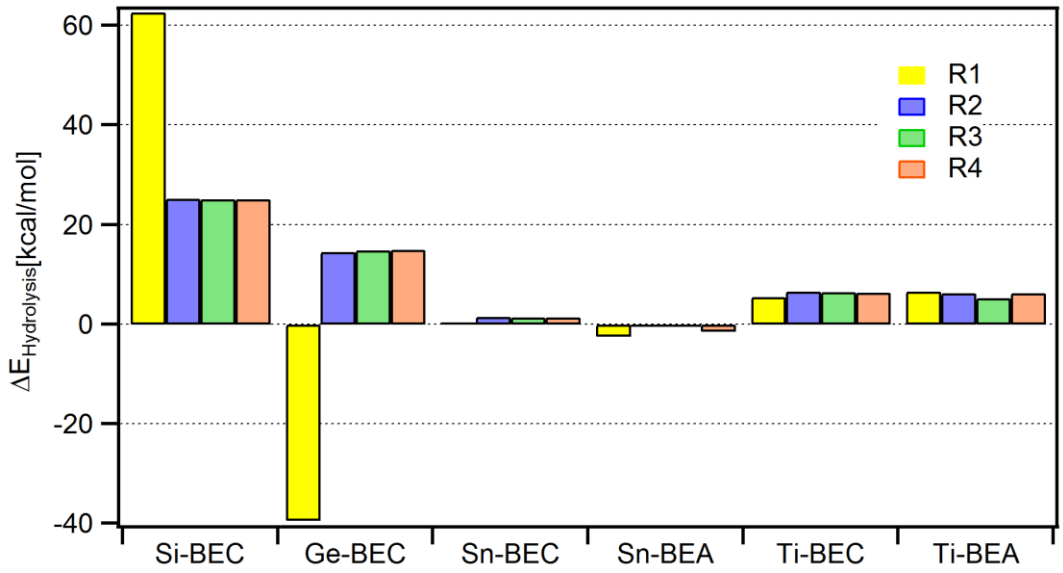

Figure 2-10. Electronic energies of hydrolysis of M-BEC (M = Ge, Sn, Ti), Sn-BEA and Ti-BEA including water as a solvent through PCM. For M-BEC the ratios M/Si are R1=1/13, R2=1/32, R3=1/64, R4=1/114; for Sn-BEA the ratios Sn/Si are R1=2/30, R2=2/50, R3=2/86, R4=2/148; for Ti-BEA the ratios Ti/Si are R1=1/15, R2=1/33, R3=1/62, R4=1/110.

Table A-19 shows the electronic properties (ε_{LUMO}, η, NBO charges) for the hydrolyzed and non-hydrolyzed M-BEC, Sn-BEA and Ti-BEA. The hardness and the NBO charges are not affected by the solvent. Figure 2-11 shows the LUMO energies of the hydrolyzed and non-hydrolyzed M-BEC, Sn-BEA and Ti-BEA when the solvent is included in the calculations through the PCM. Si-BEC, Ge-BEC and Sn-BEC have high LUMO energies, indicating their poor Lewis acidity. The LUMO energy of the hydrolyzed Sn-BEC increases drastically when compared to the non-hydrolyzed counterpart, indicating that the incorporation of Sn in the polymorphism C would not have a high Lewis acidity in water. The lowest LUMO energy was obtained for Ti-BEC, suggesting that Ti-BEC has a higher Lewis acidity that Sn-BEA even in the presence of water.

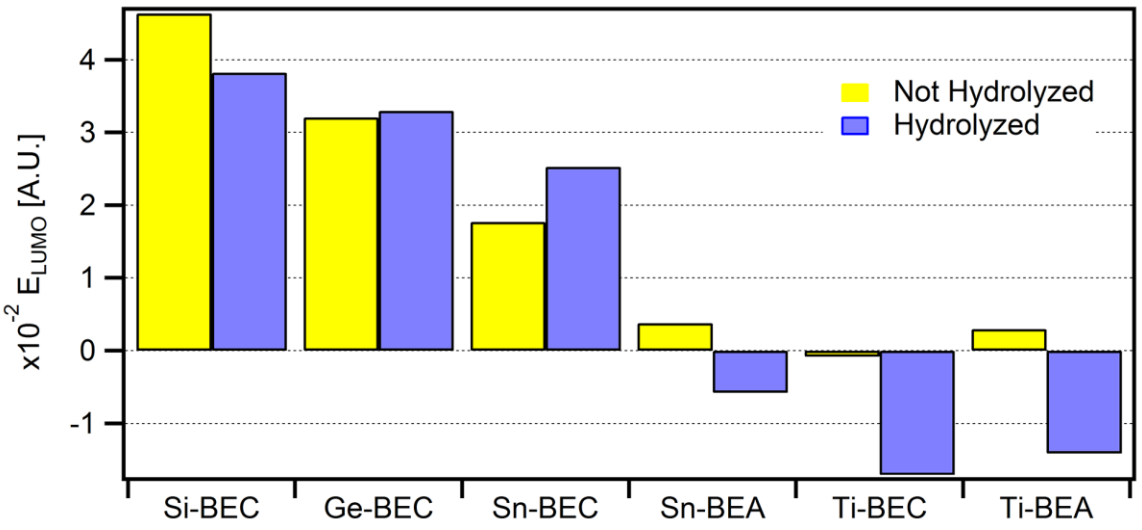

Figure 2-11. LUMO energies of the hydrolyzed and non-hydrolyzed M-BEC (M = Ge, Sn, Ti), Sn-BEA and Ti-BEA taken the solvent into account through PCM.

2.4 CONCLUSIONS

Our results demonstrate that the most favorable substitution of Ti, Ge and Sn in BEC is in the T1-site. This site also corresponds to the site that yields the highest Lewis acidity for these metal

substituted zeolites. Hydrolyzed Ti-BEC and Ti-BEA have the lowest LUMO energies of the systems that were analyzed, even when the solvent was included in the calculations. Hydrolyzed Ti-BEC and Ti-BEA also have the lowest hardness and NBO charges, suggesting that these materials would be soft acids. Our results also demonstrate that based on the hydrolysis energies, Ti substituted zeolites have a higher hydrothermal stability than Sn substituted zeolites. Also, the hydrolysis of Ge-BEC is energetically favorable when the Ge/Si ratio is 1/13. The local structural perturbation calculated for each of the systems suggests that the substitution of Ti in BEC is more favorable than Sn in either BEA of BEC. Finally, our calculations demonstrate that Ti-BEC exhibits similar electronic properties than Ti-BEA, and because of its crystalline structure with less faults than BEA, it should outperform BEA catalysts for reactions mediated by Lewis acidity.

2.5 REFERENCES

(1) Assary, R. S.; Curtiss, L. A.; Dumesic, J. A. Exploring Meerwein–Ponndorf–Verley Reduction Chemistry for Biomass Catalysis Using a First-Principles Approach. *ACS Catal.* **2013**, *3*, 2694–2704.

(2) Moliner, M.; Román-Leshkov, Y.; Davis, M. E. Tin-Containing Zeolites Are Highly Active Catalysts for the Isomerization of Glucose in Water. *Proc. Natl. Acad. Sci. U. S. A.* **2010**, *107*, 6164–6168.

(3) Newsam, J. M.; Treacy, M. M. J.; Koetsier, W. T.; Gruyter, C. B. D. Structural Characterization of Zeolite Beta. *Proc. R. Soc. A Math. Phys. Eng. Sci.* **1988**, *420*, 375–405.

(4) Bare, S. R.; Kelly, S. D.; Sinkler, W.; Low, J. J.; Modica, F. S.; Valencia, S.; Corma, A.; Nemeth, L. T. Uniform Catalytic Site in Sn-Beta-Zeolite Determined Using X-Ray Absorption Fine Structure. *J. Am. Chem. Soc.* **2005**, *127*, 12924–12932.

(5) Szostak, R.; Lillerud, K.; Stocker, M. Properties of Tschernichite, the Aluminum-Rich Mineral Analog of Zeolite Beta. *J. Catal.* **1994**, *148*, 91–99.

(6) Szostak, R.; Pan, J. M.; Lillerudo, K. P. High-Resolution TEM Imaging of Extreme Faulting in Natural Zeolite Tschernichite. *J. Phys. Chem.* **1995**, *99*, 2104–2109.

(7) Wolf, P.; Valla, M.; Rossini, A. J.; Comas-Vives, A.; Núñez-Zarur, F.; Malaman, B.; Lesage, A.; Emsley, L.; Copéret, C.; Hermans, I. NMR Signatures of the Active Sites in Sn-β Zeolite. *Angew. Chem. Int. Ed. Engl.* **2014**, *53*, 10179–10183.

(8) Moliner, M.; Corma, A. Advances in the Synthesis of Titanosilicates: From the Medium Pore TS-1 Zeolite to Highly-Accessible Ordered Materials. *Microporous Mesoporous Mater.* **2014**, *189*, 31–40.

(9) Corma, A.; Navarro, M. T.; Rey, F.; Rius, J.; Valencia, S. Pure Polymorph C of Zeolite Beta Synthesized by Using Framework Isomorphous Substitution as a Structure-Directing Mechanism. *Angew. Chem. Int. Ed. Engl* **2001**, *40*, 2277–2280.

(10) Lee, F. Y.; Lv, L.; Su, F.; Liu, T.; Liu, Y.; Sow, C. H.; Zhao, X. S. Incorporation of Titanium into Polymorph C for Catalytic Epoxidation of Cyclohexene. *Microporous Mesoporous Mater.* **2009**, *124*, 36–41.

(11) Moliner, M.; Serna, P.; Catin, A.; Sastre, G.; Diaz-Cabanas, M.; Corma, A. Synthesis of the Ti-Silicate Form of BEC Polymorph of B-Zeolite Assisted by Molecular Modeling. *J. Phys. Chem. C* **2008**, *112*, 19547–19554.

(12) Cantín, Á.; Corma, A.; Díaz-Cabañas, M. J.; Jordá, J. L.; Moliner, M.; Rey, F. Synthesis and Characterization of the All- Silica Pure Polymorph C and an Enriched Polymorph B Intergrowth of Zeolite Beta. *Angew. Chem. Int. Ed. Engl.* **2006**, *45*, 8013–8015.

(13) Shetty, S.; Pal, S.; Kanhere, D. G.; Goursot, A. Structural, Electronic, and Bonding Properties of Zeolite Sn-Beta: A Periodic Density Functional Theory Study. *Chem. a Eur. J.* **2006**, *12*, 518–523.

(14) Petkov, P. St.; Aleksandrov, H. a.; Valtchev, V.; Vayssilov, G. N. Framework Stability of Heteroatom-Substituted Forms of Extra-Large-Pore Ge-Silicate Molecular Sieves: The Case of ITQ-44. *Chem. Mater.* **2012**, *24*, 2509–2518.

(15) Shetty, S.; Kulkarni, B. S.; Kanhere, D. G.; Goursot, A.; Pal, S. A Comparative Study of Structural, Acidic and Hydrophilic Properties of Sn-BEA with Ti-BEA Using Periodic Density Functional Theory. *J. Phys. Chem. B* **2008**, *112*, 2573–2579.

(16) Kulkarni, B. S.; Krishnamurty, S.; Pal, S. Probing Lewis Acidity and Reactivity of Sn- and Ti-Beta Zeolite Using Industrially Important Moieties: A Periodic Density Functional Study. *J. Mol. Catal. A Chem.* **2010**, *329*, 36–43.

(17) Yang, G.; Pidko, E. a.; Hensen, E. J. M. Structure, Stability, and Lewis Acidity of Mono and Double Ti, Zr, and Sn Framework Substitutions in BEA Zeolites: A Periodic Density Functional Theory Study. *J. Phys. Chem. C* **2013**, *117*, 3976–3986.

(18) Yang, G.; Zhou, L.; Han, X. Lewis and Brönsted Acidic Sites in M4+-Doped Zeolites (M=Ti, Zr, Ge, Sn, Pb) as Well as Interactions with Probe Molecules: A DFT Study. *J. Mol. Catal. A Chem.* **2012**, *363–364*, 371–379.

(19) Boronat, M.; Corma, A.; Renz, M. Mechanism of the Meerwein-Ponndorf-Verley-Oppenauer (MPVO) Redox Equilibrium on Sn- and Zr-Beta Zeolite Catalysts. *J. Phys. Chem. B* **2006**, *110*, 21168–21174.

(20) Becke, A. D. Density-Functional Thermochemistry . III . The Role of Exact Exchange. *J. Chem. Phys.* **1993**, *98*, 5648–5652.

(21) Perdew, J. P.; Wang, Y. Accurate and Simple Analytic Representation of the Electron-Gas Correlation Energy. *Phys. Rev. B* **1992**, *45*, 13244–13249.

(22) Chai, J.-D.; Head-Gordon, M. Long-Range Corrected Hybrid Density Functionals with Damped Atom-Atom Dispersion Corrections. *Phys. Chem. Chem. Phys.* **2008**, *10*, 6615–6620.

(23) Sastre, G.; Vidal-Moya, J. a; Blasco, T.; Rius, J.; Jordá, J. L.; Navarro, M. T.; Rey, F.; Corma, A. Preferential Location of Ge Atoms in Polymorph C of Beta Zeolite (ITQ-17) and Their Structure-Directing Effect: A Computational, XRD, and NMR Spectroscopic Study. *Angew. Chem. Int. Ed. Engl.* **2002**, *41*, 4722–4726.

(24) International Zeolite Association (IZA). http://europe.iza-structure.org/IZA-SC/ftc_fw.php?STC=MFI (accessed Aug 20, 2016).

(25) Yang, G.; Lan, X.; Zhuang, J.; Ma, D.; Zhou, L.; Liu, X.; Han, X.; Bao, X. Acidity and Defect Sites in Titanium Silicalite Catalyst. *Appl. Catal. A Gen.* **2008**, *337*, 58–65.

(26) Sung, C.-Y.; Broadbelt, L. J.; Snurr, R. Q. A DFT Study of Adsorption of Intermediates in the NOx Reduction Pathway over BaNaY Zeolites. *Catal. Today* **2008**, *136*, 64–75.

(27) Hay, P. J.; Wadt, W. R. Ab Initio Effective Core Potentials for Molecular Calculations. Potentials for K to Au Including the Outermost Core Orbitals. *J. Chem. Phys.* **1985**, *82*, 299–310.

(28) Andrae, D.; Häußermann, U.; Dolg, M.; Stoll, H.; Preuß, H. Energy-Adjusted Ab Initio Pseudopotentials for the Second and Third Row Transition Elements. *Theor. Chim. Acta* **1990**, *77*, 123–141.

(29) Weinhold, F.; Carpenter, J. *The Structure of Small Molecules and Ions*; Naaman, R., Vager, Z., Eds.; Springer US: (Plenum, New York), 1988.

(30) Frisch, M. J.; Trucks, G. W.; Schlegel, H. B.; Scuseria, G. E.; Robb, M. A.; Cheeseman, J. R.; Scalmani, G.; Barone, V.; Mennucci, B.; Petersson, G. A.; et al. Gaussian 09, Revision A.02. *Gaussian Inc Wallingford CT*. Gaussian, Inc. 2009.

(31) Corma, A.; Domine, M. E.; Nemeth, L.; Valencia, S. Al-Free Sn-Beta Zeolite as a Catalyst for the Selective Reduction of Carbonyl Compounds (Meerwein-Ponndorf-Verley Reaction). *J. Am. Chem. Soc.* **2002**, *124*, 3194–3195.

(32) Schaffer, C. L.; Thomson, K. T. Density Functional Theory Investigation into Structure and Reactivity of Prenucleation Silica Species. *J. Phys. Chem. C* **2008**, *112*, 12653–12662.

(33) Stare, J.; Henson, N. J.; Eckert, J. Mechanistic Aspects of Propene Epoxidation by Hydrogen Peroxide. Catalytic Role of Water Molecules, External Electric Field, and Zeolite Framework of TS-1. *J. Chem. Inf. Model.* **2009**, *49*, 833–846.

(34) Sastre, G.; Corma, A. Relation between Structure and Lewis Acidity of Ti-Beta and TS-1 Zeolites : A Quantum-Chemical Study. *Chem. Phys. Lett.* **1999**, *302*, 447–753.

(35) Pearson, R. G. Chemical Hardness and Density Functional Theory. *J. Chem. Sci.* **2005**, *117*, 369–377.

(36) Gamba, A.; Tabacchi, G.; Fois, E. TS-1 from First Principles. *J. Phys. Chem. A* **2009**, *113*, 15006–15015.

(37) Yang, G.; Wang, Y.; Zhou, D.; Liu, X.; Han, X.; Bao, X. Density Functional Theory Calculations on Various M/ZSM-5 Zeolites: Interaction with Probe Molecule H2O and Relative Hydrothermal Stability Predicted by Binding Energies. *J. Mol. Catal. A Chem.* **2005**, *237*, 36–44.

(38) Corma, A.; Davis, M. E. Issues in the Synthesis of Crystalline Molecular Sieves: Towards the Crystallization of Low Framework-Density Structures. *ChemPhysChem* **2004**, *5*, 304–313.

(39) Jiang, J.; Yu, J.; Corma, A. Extra-Large-Pore Zeolites: Bridging the Gap between Micro and Mesoporous Structures. *Angew. Chem. Int. Ed. Engl.* **2010**, *49*, 3120–3145.

(40) Corma, A.; Domine, M.; Valencia, S. Water-Resistant Solid Lewis Acid Catalysts: Meerwein–Ponndorf–Verley and Oppenauer Reactions Catalyzed by Tin-Beta Zeolite. *J. Catal.* **2003**, *215*, 294–304.

(41) Moliner, M.; Diaz-Cabanas, M.; Fornes, V.; Martinez, C.; Corma, A. Synthesis Methodology, Stability, Acidity, and Catalytic Behavior of the 18×10 Member Ring Pores ITQ-33 Zeolite. *J. Catal.* **2008**, *254*, 101–109.

3 CHAPTER - DFT STUDY OF CLOSED AND OPEN SITES OF BEA, FAU, MFI, AND BEC ZEOLITES SUBSTITUTED WITH SN AND TI.

3.1 INTRODUCTION

The incorporation of heteroatoms, such as Ti and Sn into zeolites frameworks modifies the catalytic properties of zeolites. It is well known that different frameworks exhibit different catalytic activities. For instance, Lew and coworkers reported high conversions of glucose to fructose with Sn substituted beta (Sn-BEA), while the conversion was almost null after 3 hours with Sn substituted MFI (Sn-MFI).[1] The difference in conversion between the two systems might reflect the size exclusion of MFI, since the pore diameter of MFI is significantly smaller than BEA.

Interestingly, however, in a reaction involving smaller molecules, Osmundsen and coworkers reported that the reaction of dihydroxyacetone to methyl lactate has higher yields when catalyzed by Sn-BEA than by Sn-MFI, with the same Si/Sn ratio.[2] The catalytic activity of a zeolite framework is commonly correlated with either the Lewis or the Brønsted acidity, depending on the reaction to be catalyzed. A Lewis acid is defined as a chemical species that accepts electron density from a Lewis base, while a Brønsted acid is defined as a species that donates a proton in a chemical reaction. In previous works, the adsorption of probe molecules, such as ammonia, acetonitrile, water or pyridine on M-MFI (M = Ti, Zr, Ge, Sn, Pb),[3] M-BEA (M = Ti, Zr, Sn)[4] and Sn-BEA[5] has been correlated with the Lewis acidity. The Brønsted acidity, on the other hand, is commonly correlated with the deprotonation energy.[6]

Many zeolites exhibit high hydrothermal stabilities, and have proven to be excellent catalysts for a wide range of reactions involving the transformation of biomass into high value chemicals. For these particular reactions, water plays an important role as it may be produced as a byproduct (e.g., the production of 5-hydroxymethylfurfural and furfural from fructose and xylose,

respectively).[7] Few studies have reported the catalytic performance of metal-substituted zeolites in water.[8,9] Water is a protic solvent that can act as a Lewis base. Because of its mild basicity, water can compete with the reactants to coordinate with the acid sites within the metal-substituted zeolites, and hence, can decrease the Lewis acidity of the zeolites.[8]

MFI, BEA, BEC and FAU have a tridimensional pore system with a maximum sphere diameter that can diffuse along their pores of 4.70 Å, 5.95 Å, 6.09 Å, and 7.35 Å, respectively.[10] Metal substituted BEA and MFI have been the most studied zeolites for reactions that require Lewis acidity.[1,2,11,12] BEA consists of a highly faulted intergrowth of two polymorphisms (Polymorphism A and B), with two straight channels along a- and b- axis, and one tortuous channel along the c-axis.[13] Al-FAU has been widely studied in reactions involving Brønsted acidity,[14] but only few studies have reported the substitution of Ti or Sn in FAU or BEC.[15–18] BEC is a third polymorphism of zeolite beta that can be synthesized as a pure and crystalline structure without faults.[19] Corma and coworkers reported higher turnover frequencies for Ti-BEC than Ti-BEA in the epoxidation of cyclic-alkenes, attributing the difference to the diffusion problems presented in BEA.[16]

Density functional theory (DFT) has been used to analyze the substitution of several heteroatoms in the zeolites. Periodic DFT calculations have been applied to analyze Sn-, Ti-, and Zr-BEA.[4,20] Cluster models have been also used to study Ti-MFI,[21] Sn-BEA,[5] and Ti-, Zr-, Ge-, Sn-, Pb- MFI.[3] In general, these studies calculated the preferential site of substitution of the heteroatoms in the zeolite, and measured the Lewis acidities through either the LUMO energies or the adsorption of probe molecules. Similarly, the Brønsted acidities have been measured by employing DFT calculations. For instance, Jones and coworkers related the Brønsted acidities of Al-, Ga-, Fe-, B- MFI with their deprotonation energies.[6] Jones and coworkers also related the

rate constants of a dehydration reaction mediated by Brønsted sites with the van der Waals energies in different Al-substituted zeolites.[22] While most of those studies have made significant contributions to the fundamental understanding of metal-substituted zeolites, a systematic analysis of the effect of the zeolite framework on the Lewis acidity, Brønsted acidity and on the electronic properties of Sn and Ti still lacks in the literature. Furthermore, quantum mechanical calculations based solely on cluster models or periodic boundary conditions might face the shortcomings from these methods. For instance, the use of clusters models does not take into account long-range interactions with the zeolite framework. Moreover, this approach may result in artificial effects due to the hydrogen atoms lying at the boundary of the truncated structure. Periodic DFT calculations, on the other hand, may result in a metal-substituted-zeolite with a high percent of substitution.

In this study, we systematically analyzed and compared the properties of zeolites BEA, FAU, MFI, and BEC, substituted with Sn and Ti. We used DFT and ONIOM, which is an integrated quantum mechanics (QM) / molecular mechanics (MM) method that takes in consideration long-range interactions. The Lewis acidities of the metal-substituted zeolites were measured through the NH_3 binding energies, the charge transfer of NH_3 upon adsorption, and the LUMO energies. We also calculated the Lewis acidities in water by using a polarizable continuum model and by incorporating water molecules in the system. We reported the hydrolysis energies, as well as the deprotonation energies of the open sites.

Finally, the properties of BEA with a single and a double Sn-substitution are presented to compare the active sites obtained with two different methods commonly employed for the synthesis of Sn-BEA.

3.2 METHODOLOGY

The coordinates used to generate the BEA, FAU and MFI clusters were obtained from the International Zeolite Association (IZA).[10] The coordinates for the BEC clusters were obtained from the experimentally refined structure reported in the literature.[19] The cluster models were obtained by cutting the periodic structure, as is shown in Figure 3-1, and Figure B-1 to Figure B-5, in the Appendix B. The boundary Si-atoms were saturated with hydrogen atoms, which were aligned on the same direction of the oxygen atoms that were removed. The Si-H bonds were maintained at 1.5000 Å. All the results were obtained using the functional ωB97XD,[23] which is a long-range corrected functional. A mix of basis sets were used in the calculations involving the preferential substitution site, binding energy of NH_3 and the electronic properties of the different zeolites. The Pople basis set 6-31+g** was used for Si, O, N and H atoms, whereas the effective core potentials LANL2DZ,[24] and MWB46[25] were used for Ti, and Sn, respectively. For the calculations involving deprotonation energies and hydrolysis energies, a larger basis set (6-311++g**) was applied to Al, Si, O and H in order to enhance the ability of the clusters to delocalize the charge.[6] In our previous study, this methodology was validated against FTIR, NMR shifts, and the crystallographic positions of metal-substituted zeolites.[26] The geometry optimizations were performed by optimizing all the atoms, except for the terminal hydrogen atoms that were kept fixed. For the DFT clusters, the partial atomic charges were obtained with the natural bond orbital (NBO) population analysis.[27]

Figure 3-1 shows the M-BEA, M-BEC, M-FAU, M-MFI and Sn-BEA clusters centered in the preferred site of substitution. Other clusters used for the calculation of the preferred site of substitution are shown in Figure B-1 to Figure B-5, in the Appendix B. Bare and coworkers demonstrated that the substitution of Sn in zeolite beta is a double-paired substitution in the T2

sites.[28] Hence, the preferential location for the double substitution of Sn in BEA (Sn-BEA) was taken from the work of Bare and coworkers. However, we also analyzed a single Sn substitution in BEA (Sn-1-BEA) and compared the properties of both materials. The electronic properties of Sn-1-BEA were obtained with the clusters of BEA centered in T2 (Figure 3-1a) as previous DFT studies have demonstrated that the preferential site of a single substitution of Sn in BEA is at T2.[4]

The hydrolysis energies of metal-substituted zeolites were calculated with ONIOM in order to incorporate the effect of the surrounding zeolite framework. Single point calculations on the optimized structures were then performed with a polarizable continuum model (PCM) to study the effect of the solvent on the reaction energies. For these calculations, water was used as the solvent, which has a dielectric constant of 78.3553. ONIOM is a combined QM/MM method, in which two layers are linked via mechanical embedding. The functional ωB97XD was used for the QM layer, and UFF[29] was used for the MM layer. Figure 3-2 shows the ONIOM clusters of M-BEA, M-BEC, M-FAU, M-MFI and Sn-BEA with M/Si ratios of 1/62, 1/63, 1/54, 1/76 and 2/86, respectively. Figure 3-3 shows the ONIOM clusters of M-BEA, M-BEC, M-FAU, M-MFI and Sn-BEA with M/Si ratios of 1/110, 1/113, 1/91, 1/135 and 2/148, respectively. The NH_3 adsorption energies were calculated in vacuum, as well as in water using the PCM model. NH_3 binding energies and hydrolysis energies were calculated with the ONIOM clusters shown in Figure 3-2 and Figure 3-3, respectively. The ONIOM clusters were set with more than 28 T-atoms to avoid finite size effects.[30] The net charge of NH_3 adsorbed on the metal-substituted zeolites was obtained using the electrostatic potential (ESP) charges as implemented in ONIOM.[31,32] The deprotonation energies were calculated using the ONIOM clusters shown in Figure 3-3. All calculations were carried out with Gaussian 09.[33]

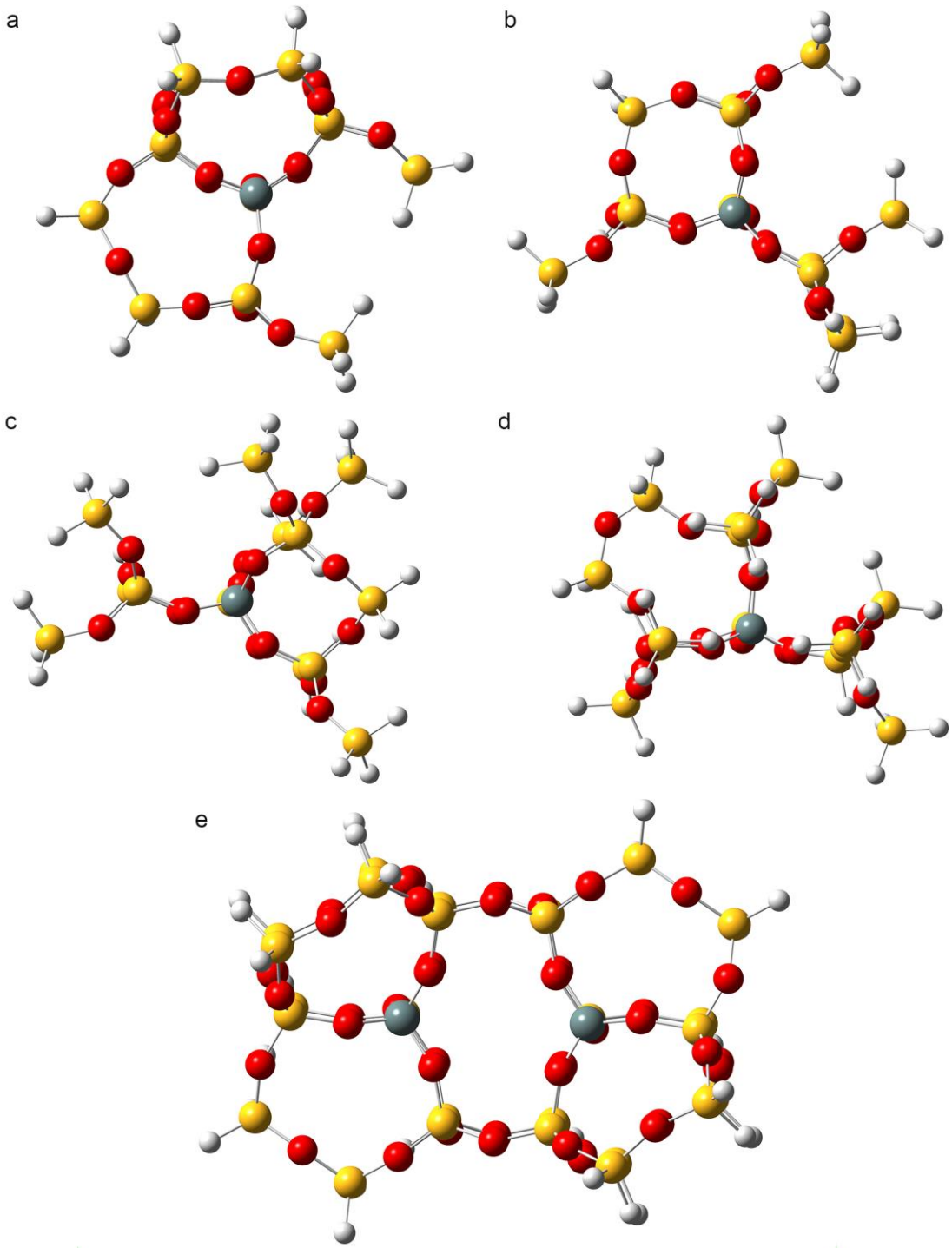

Figure 3-1. Clusters used for the DFT calculations of M-BEA, M-BEC, M-FAU, M-MFI and Sn-BEA. (a) 59-atom M-BEA cluster centered in T2 (b) 53-atom M-BEC cluster centered in T1 (c) 54-atom M-FAU cluster centered in T11 (d) 65-atom M-MFI cluster centered in T11 (e) 98-atoms Sn-BEA cluster centered in a double substitution in T2 sites. Color legend: yellow = Si; red = O; white = H; gray = metal atom (M = Sn or Ti)

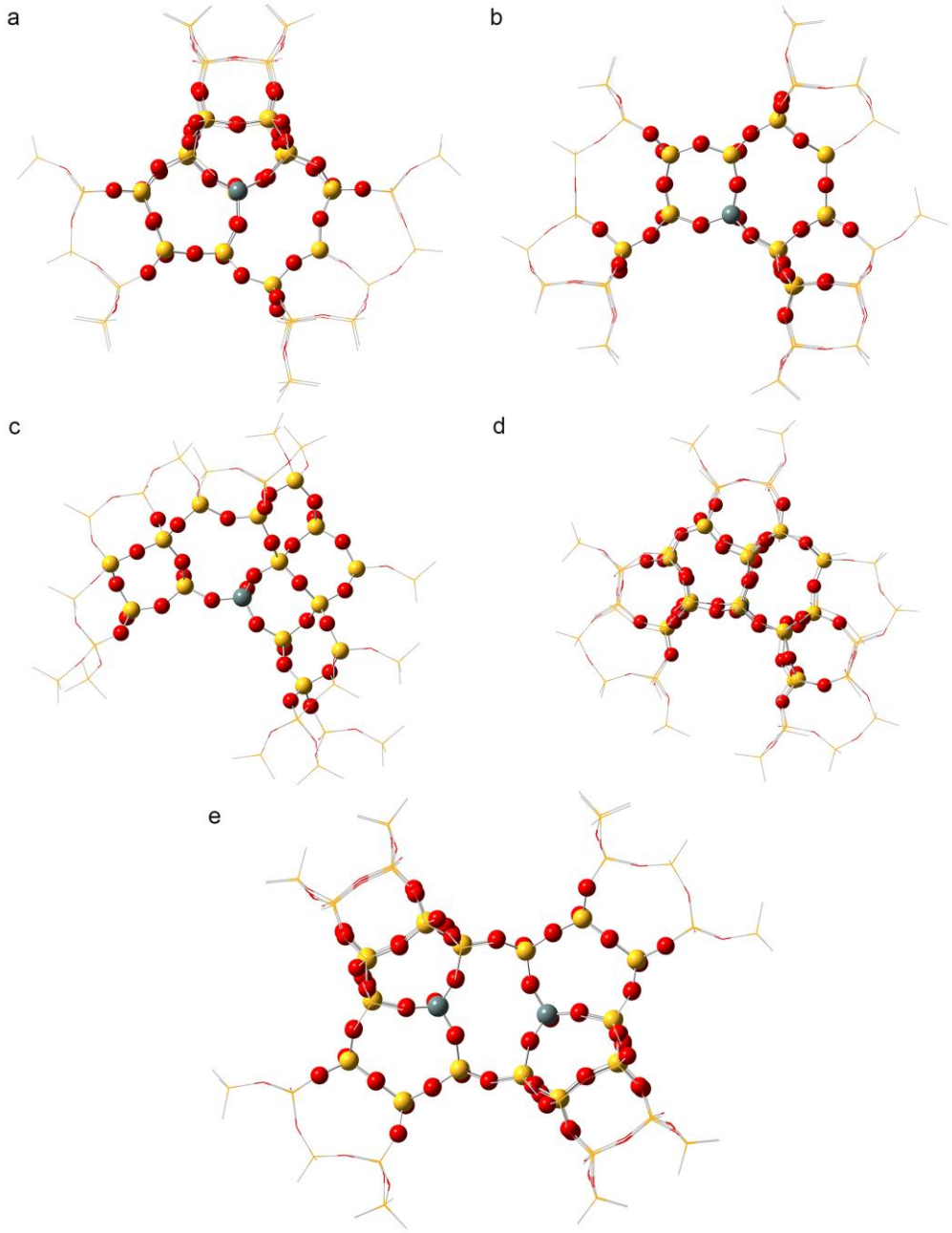

Figure 3-2. ONIOM clusters of M-BEA, M-BEC, M-FAU, M-MFI and Sn-BEA with different M/Si ratios. M corresponds to the metal atom Sn or Ti. (a) 219-atoms M-BEA cluster (64-DFT-atoms, 155-MM-atoms) with a Ti/Si ratio of 1/62, (b) 228-atoms M-BEC cluster (56-DFT-atoms, 172-MM-atoms) with a M/Si ratio of 1/63, (c) 195-atoms M-FAU cluster (62-DFT-atoms, 133-MM-atoms) with a M/Si ratio of 1/54, (d) 268-atoms M-MFI cluster (70-DFT-atoms, 198-MM-atoms) with a M/Si ratio of 1/76, and (e) 300-atoms Sn-BEA cluster (104-DFT-atoms, 196-MM-atoms) with a Sn/Si ratio of 2/86. The atoms treated with DFT and the atoms treated with MM are shown with the ball and stick, and with the wireframe representations, respectively.

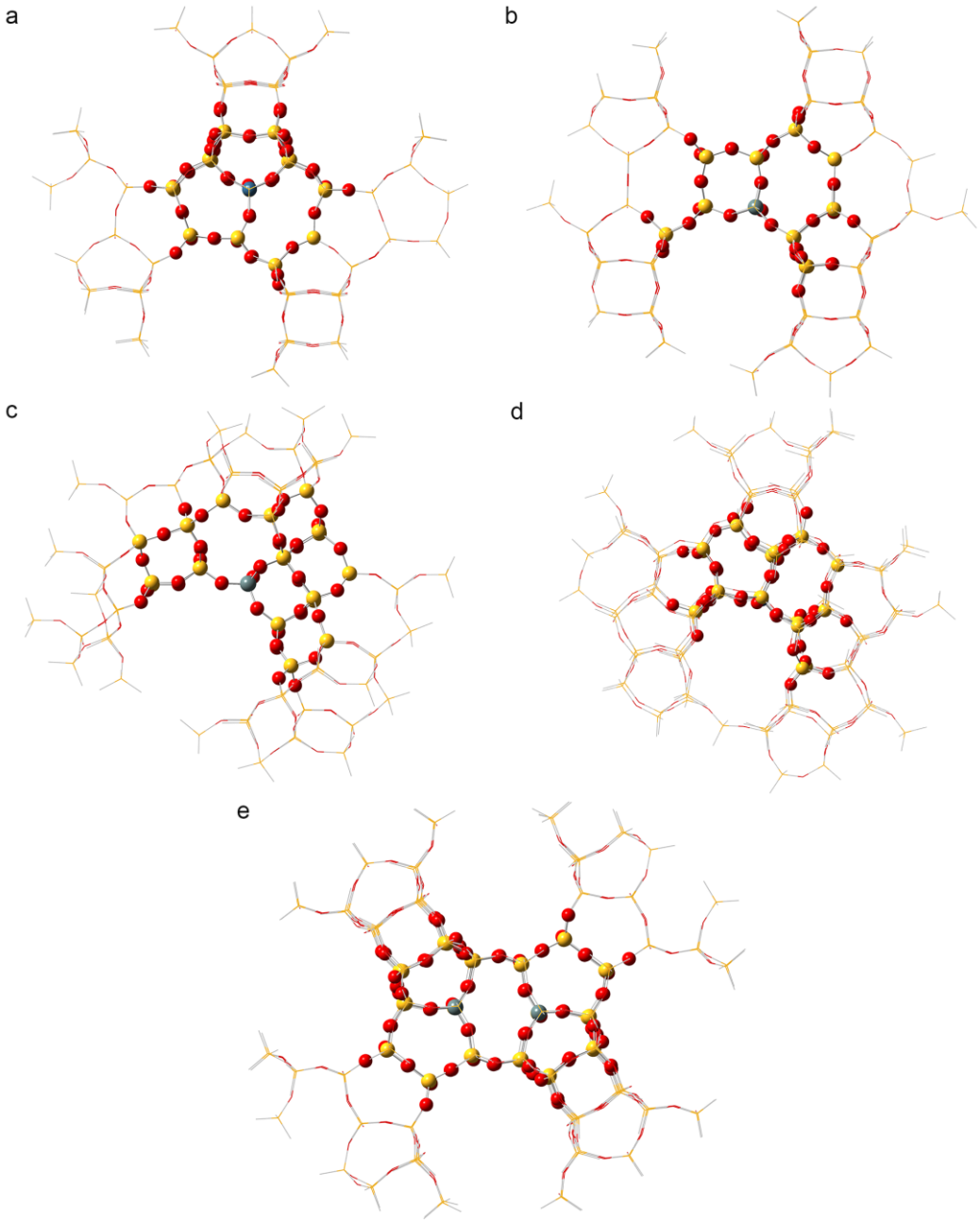

Figure 3-3. ONIOM clusters of M-BEA, M-BEC, M-FAU, M-MFI and Sn-BEA with different M/Si ratios. M corresponds to the metal atom Sn or Ti. (a) 381-atoms M-BEA cluster (64-DFT-atoms, 317-MM-atoms) with a Ti/Si ratio of 1/110, (b) 394-atoms M-BEC cluster (56-DFT-atoms, 338-MM-atoms) with a M/Si ratio of 1/113, (c) 320-atoms M-FAU cluster (62-DFT-atoms, 258-MM-atoms) with a M/Si ratio of 1/91, (d) 468-atoms M-MFI cluster (70-DFT-atoms, 398-MM-atoms) with a M/Si ratio of 1/135, and (e) 510-atoms Sn-BEA cluster (104-DFT-atoms, 406-MM-atoms) with a Sn/Si ratio of 2/148. The atoms treated with DFT and the atoms treated with MM are shown with the ball and stick, and with the wireframe representations, respectively.

3.3 RESULTS AND DISCUSSION

The following sections discuss the results obtained for Sn and Ti substituted in BEA, BEC, FAU and MFI. First, the preferential locations of Ti and Sn in the metal substituted zeolites are presented followed by the analysis of the open sites in the metal-substituted zeolites, with their corresponding Brønsted acidities. The Lewis acidities of the open and closed sites in vacuum, and in water are then discussed. In the last section, the properties of BEA with a single and a double substitution of Sn in the framework are presented in order to compare the active sites that could be obtained with the two experimental methods reported in the literature for the synthesis of Sn-BEA.[34–36]

3.3.1 Preferential Location of Ti and Sn in BEA, BEC, FAU and MFI Zeolites

The preferential locations of Ti and Sn in the zeolites were determined based on the electronic energies of reaction (E_{rx}) for the reaction depicted in Scheme 3-1, and they were calculated with Equation 3-1.

Scheme 3-1. Reaction describing the metal substitution into the zeolite framework.

$$Zeo[Si] + M(OH)_4 \quad \rightarrow \quad Zeo[M] + Si\ (OH)_4$$

$$\mathrm{E_{rx}} = \mathrm{E_{Zeo[M]}} + \mathrm{E_{Si\ (OH)_4}} - \mathrm{E_{Zeo[Si]}} - \mathrm{E_{M(OH)4}} \qquad \textbf{(3-1)}$$

In Equation 3-1 and Scheme 3-1, *M* represents the metal to be substituted in the zeolite. Thus, *Zeo*[*Si*] and *Zeo*[*M*] correspond to the silica zeolite and the metal-substituted zeolite, respectively. Because the reaction energies, as described in Equation 3-1, depend on the stability of the species $Si(OH)_4$, $Sn(OH)_4$, and $Ti(OH)_4$, we only used this method to determine the preferential substitution of one heteroatom in a specific zeolite. Table B-1 and Table B-2 in the Appendix B show the E_{rx}'s for the substitution of the heteroatoms (Sn, Ti) in BEC and MFI, respectively. Similarly, Table B-3 in the Appendix B shows the E_{rx}'s of Ti in BEA. In our previous work,[26] this

methodology was used to corroborate that the preferential location of Ge in BEC is in T1. This result is in good agreement with the results reported by Sastre and coworkers, in which they determined that the preferential location of Ge in BEC is in T1 based on XRD and NMR spectroscopy.[37] On the basis of our results, the preferential substitution site of Sn and Ti in BEC is also in T1.

The lowest electronic energy for the substitution of Ti in MFI was obtained in T10 (100.16 kJ/mol) followed by T11 (101.55 kJ/mol). However, the electronic energies for the substitution of Ti in the different sites of MFI are similar among the different sites. For instance, the energy difference between the most favorable substitution site (T10), and the least favorable substitution site (T6) is only 18.75 kJ/mol. These results indicate that, while the preferential location for the substitution of Ti in MFI is in T10 and T11, the substitution can also occur in the other T-sites of the zeolite. These results are in good agreement with several experimental results. For instance, Lamberti and coworkers concluded that Ti is homogeneously distributed in all the T-sites of the MFI zeolite based on results obtained through Synchrotron Radiation X-Ray Powder Diffraction.[38] However, by using high resolution temperature-dependent XRD, Marra and coworkers determined that about half of the Ti atoms were located in T10 and T11 on MFI, while the rest of the Ti atoms were located among the T1-T3 and T5-T9 sites.[39] The electronic energies for the substitution of Sn in MFI, on the other hand, are more dispersed. The preferential location of Sn in MFI is located in T11 (132.51 kJ/mol), followed by T10 (141.88 kJ/mol). The lowest energy obtained for the substitution of Ti in BEA was for T1 (62.09 kJ/mol), followed closely by T2 (62.30 kJ/mol). This result is in agreement with the periodic DFT calculations of Yang and coworkers, which determined that the preferential substitution of Ti in BEA is in T1, followed by T2.[4]

In this work, we calculated the properties of the metal-substituted zeolites only in the preferential locations. For Ti-MFI, we analyzed the substitution in the T11 site. Since the substitution of Ti in the T10 and T11 sites are close energetically, (e.g. the energy difference between both sites is 1.39 kJ/mol), we analyzed the same site of substitution for Sn and Ti in MFI.

3.3.2 Open Sites in M-BEA, M-BEC, M-FAU and M-MFI

Open sites ($M(OSi)_3OH$) are defects formed when the substituted metal is not completely bonded to the four oxygen atoms of the zeolite. Open sites have been detected in Ti-MFI and Sn-BEA.[5,21,40–43] For instance, solid state MAS NMR has been used to detect open sites in Ti-MFI,[21,40,41] and the open sites have been quantified with Neutron Powder Diffraction.[42] Boronat and coworkers obtained different ratios of open/closed sites in Sn-BEA by varying the water concentration in the zeolite activation, and they proposed that the open sites are formed through the hydrolysis of Sn-O-Si bridges during the activation process.[5]

The hydrolysis of metal substituted zeolites can occur through four different bonds, with the exception of Sn-BEA, in which eight different bonds had to be analyzed due to its double substitution. Thus, the open sites structures were obtained with the weakest M-O bond in the zeolites by comparing the hydrolysis energies of the metal substituted zeolites, as shown in Scheme 3-2. Figure B-6 to Figure B-10 and Table B-4 – Table B-8 in the Appendix B show the hydrolysis energies involving each of the bonds of the zeolites. For BEC, FAU and MFI, the weakest bond was the same, regardless if the zeolite was substituted with Sn or Ti.

Scheme 3-2. Hydrolysis reaction of the metal substituted zeolite.

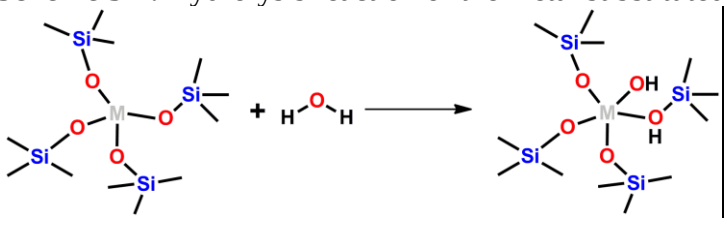

Figure 3-4 shows the hydrolysis energies obtained with the weakest bonds of the metal substituted zeolites. The energies were calculated with the ONIOM clusters depicted in Figure 3-3 and a polarizable continuum model was used in all the calculations to recreate the hydrolysis in water.

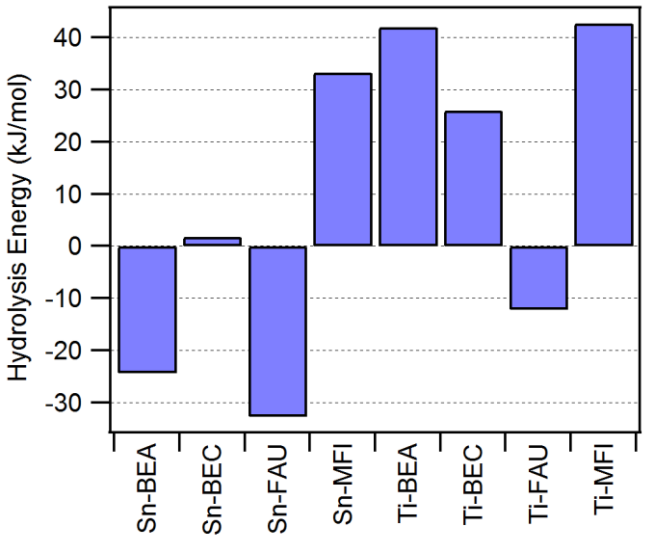

Figure 3-4. Hydrolysis energies of Sn-substituted zeolites.

On the basis of Figure 3-4, the hydrolysis of Sn-MFI is unfavorable (33.3 kJ/mol), indicating a possible low concentration of open sites in its structure. The hydrolysis energies of Sn-BEA (-24.3 kJ/mol) and Sn-FAU (-32.6 kJ/mol) are negative, suggesting that both frameworks could exhibit closed and open sites. While experimental data on the hydrolysis energies of these systems are not available, some experimental findings can be used to corroborate that, in fact, it is easier to hydrolyze Sn-BEA than Sn-MFI. For instance, Sn-BEA has been synthesized with open sites through wet activation, and in that same study Sn-MFI could not be synthesized with open sites by employing the same method.[43] To our knowledge, studies on the detection of open sites in Sn-BEC have not been reported in the literature, but based on the hydrolysis energy (1.9 kJ/mol), it is likely that Sn-BEC could be synthesized with a low concentration of open sites.

To our knowledge, studies on the stability of Ti-substituted zeolites in water have not been reported. However, there are some studies that address the stability of Ti-substituted zeolites in H_2O_2. For example, Davies and coworkers, and Carati and coworkers demonstrated that Ti-MFI and Ti-BEA are stable in H_2O_2 for over a week, before they could detect Ti leaching.[44,45] Based on the hydrolysis energies, Ti-FAU has the lowest hydrolysis energy among the Ti-substituted zeolites analyzed in this study.

3.3.3 Brønsted Acidity of the Metal Substituted Zeolites

Brønsted acids are species or materials that donate protons. Hence, the formation of open sites on metal-substituted zeolites (e.g. the product in the reaction depicted in Scheme 3-2) could provide Brønsted acidity to the zeolite. In order to measure the Brønsted acidity of the hydrolyzed metal-substituted zeolites, the deprotonation energies (DPE) were calculated with Equation 3-2.

$$DPE = E_{Zeo-M^-} - E_{Zeo[M]h} \quad \textbf{(3-2)}$$

In this equation, $E_{Zeo[M]^-}$ and $E_{Zeo[M]h}$ are the electronic energies of the deprotonated and hydrolyzed metal-substituted zeolites, respectively. Figure 3-5 shows the deprotonation energies of the various zeolites analyzed in this work. On the basis of these energies, the Brønsted acidity of the metal-substituted zeolites decreases as follows: Sn-BEA >> Ti-BEA > Sn-FAU > Sn-BEC ≈ Sn-MFI > Ti-FAU ≈ Ti-MFI > Ti-BEC.

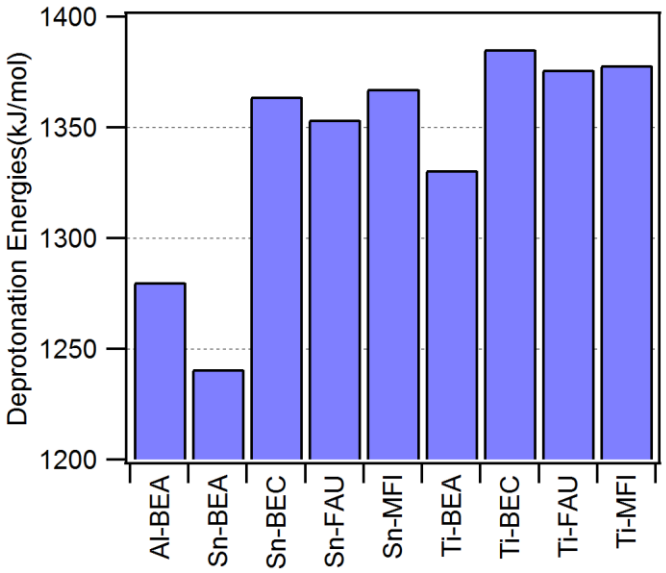

Figure 3-5. Deprotonation energies of the hydrolyzed metal-substituted zeolites

The deprotonation energy of Al-BEA was also calculated using the ONIOM cluster shown in Figure B-11 in the Appendix B. Based on the energies presented in Figure 3-5, the open site of Sn-BEA (1241 kJ/mol) has a very strong Brønsted acidity, even higher than the Brønsted acidity of Al-BEA (1280 kJ/mol). Furthermore, the deprotonation energy obtained for Sn-BEA is comparable to the deprotonation energy reported for Al-MFI. Jones and coworkers reported deprotonation energies for Al-MFI in the range of 1200 to 1250 kJ/mol, depending on the cluster size of the calculation.[6] Their results were obtained with ωB97XD and 6-311++g**, which the same level of theory for the QM part of ONIOM that was employed in this study. Wang and coworkers also reported the deprotonation energy of Y-zeolite (Al-FAU), and the deprotonation energy that they obtained with periodic DFT calculations (1244 kJ/mol), is equal to the energy obtained for the hydrolyzed Sn-BEA.[46] Our results, hence, suggest that the open sites in Sn-BEA are able to catalyze reactions requiring Brønsted acidity.

3.3.4 Lewis Acidities of BEA, BEC, FAU and MFI Zeolites Substituted with Sn and Ti in Open and Closed Sites

3.3.4.1 Electronic properties of the metal-substituted zeolites in the closed sites

Figure 3-6 shows the binding energies of NH_3, the hardness of the metal substituted zeolites, the NBO charges of the metal atom, and the charge of NH_3 upon adsorption. Ammonia is a basic molecule, and its lone pair electrons can be donated to an acid structure, such as a metal-substituted zeolite. Because a Lewis acid is defined as a structure that can accept electron density from a Lewis base, the interaction of NH_3 with the zeolite is proportional to its Lewis acidity. Some theoretical studies have also used the binding energies of ammonia on zeolites to determine their Lewis acidities.[3,20] The binding energy of ammonia was calculated with Equation 3-3.

$$E_{B.E.} = E_{Zeo[M-NH_3]} - E_{Zeo[M]} - E_{NH_3} \quad \textbf{(3-3)}$$

In this equation, $E_{Zeo[M]}$, E_{NH_3}, and $E_{Zeo[M-NH_3]}$ correspond to the electronic energies of the metal-substituted zeolite, the isolated ammonia and the adsorbed complex, respectively. On the basis of DFT, Sn-BEA has the lowest NH_3 binding energy (-117 kJ/mol), followed by Sn-BEC (-100 kJ/mol). Figure 3-6a also shows the binding energies of NH_3 on the metal substituted zeolites obtained with the ONIOM clusters depicted in Figure 3-2. The binding energies calculated with ONIOM also demonstrate that Sn-BEA and Sn-BEC have the lowest binding energies. For the rest of the zeolies analyzed in this study, the binding energies obtained with ONIOM do not follow the same trends of those obtained with DFT clusters. However, the calculated binding energies with ONIOM are in better agreement than the DFT results when compared against experimental results reported in the literature. Jänchen and coworkers reported heats of adsorption between 100 and 60 kJ/mol for the adsorption of ammonia on Ti-MFI.[47] The binding energy obtained with ONIOM is

within the energy range reported by Jänchen and coworkers, whereas the DFT result underestimated the binding energy. Thus, on the basis of the adsorption energies calculated with the ONIOM clusters, the Lewis acidity of the metal substituted zeolites decreases as follows: Sn-BEA > Sn-BEC ≈ Sn-MFI > Sn-FAU > Ti-MFI > Ti-BEC ≈ Ti-FAU ≈ Ti-BEA.

Table B-10 in the Appendix B shows the difference between the binding energy calculated with ONIOM and the binding energy calculated with the DFT clusters. Sn-MFI (-20.2 kJ/mol) and Ti-MFI (-22.4 kJ/mol) have the largest negative difference in the binding energies when the DFT and ONIOM results are compared. Table B-11 in the Appendix B lists the VDW forces contributions to the binding energies calculated with ONIOM. By taking a closer look into these contributions, the VDW forces are greater in the MFI frameworks than in the other frameworks. Our results demonstrate that VDW forces decrease with increasing pore size. The pore size of MFI (10 membered) is smaller than the pore size of BEA, BEC and FAU (12 membered), and as the pore size decreases, the interaction of ammonia with the zeolite framework is more significant. A similar conclusion was made by Jones and Iglesia when they analyzed the adsorption of ammonia on Al-MFI. They found that the VDW forces and hydrogen bondings affect significantly the adsorption energies of ammonia on Al-MFI.[48] Our results indicate that Sn-substituted zeolites have higher Lewis acidity when compared to the Ti substituted zeolites. There are various examples in the literature in which Sn-substituted zeolites exhibit higher catalytic activity than the Ti-substituted zeolites in reactions requiring high Lewis acidity.[8,12,34] For instance, Corma and coworkers reported higher activity of Sn-BEA over Ti-BEA for the Baeyer-Villiger oxidation of dihydrocarvone to the corresponding lactone.[34] Corma and coworkers also reported superior catalytic performance of Sn-BEA over Ti-BEA for the Meerwin- Ponndorf- Verley reaction of the reduction of cyclohexanone with 2-butanol.[12] These studies demonstrated that Sn-BEA in fact

gives higher conversions and yields when compared to other zeolite frameworks in reactions requiring Lewis acidity.

Figure 3-6 also shows the hardness of the metal substituted zeolites analyzed in this work. The hardness was calculated with the energy gap between the highest occupied molecular orbital (HOMO) and the lowest unoccupied molecular orbital (LUMO) of a structure.[49] On the basis of Figure 3-6b, Sn-BEA exhibits the lowest hardness among the Sn- zeolites analyzed in this study and, whereas Ti-MFI has the lowest hardness among the Ti- zeolites. The reactivity of a structure has been previously correlated to the hardness, such as the most reactive structures have the lowest hardness.[49] Based on that descriptor, Sn-BEA is the most reactive structure among the Sn-substituted zeolites analyzed in this study.

Figure 3-6c shows the partial atomic charges of the metal atom (Sn and Ti) in the zeolite. The partial atomic charge of the Sn atom is much higher than the partial atomic charge of the Ti atom in all the zeolites analyzed in this study. As the metal-substituted atom has a higher positive charge, it could be expected that the atom has a higher capacity to gain electron density. However, the charges of the heteroatoms do not change significantly with different frameworks. Thus, the partial atomic charges of metal atoms cannot be used as a descriptor of the Lewis acidity when comparing the substitution of the metal atom on different frameworks.

Figure 3-6d shows the charge of NH_3 upon adsorption onto the metal-substituted zeolites. It would be expected that upon adsorption to a Lewis acid, the NH_3 molecule would donate electron density to the metal-substituted zeolite. Furthermore, it could also be expected that the charge transfer from NH_3 to the zeolite be proportional to the Lewis acidity of the system. Hence, on the basis of Figure 3-6d, the Lewis acidity of the metal substituted zeolites decreases as follows: Sn-BEA >Sn-BEC > Sn-FAU > Ti-BEA > Sn-MFI > Ti-BEC > Ti-FAU >Ti-MFI. This trend is similar

to the one obtained with the DFT cluster, suggesting that the difference between the acidities as obtained with the DFT and ONIOM methods reflect the confinement effect of the framework.

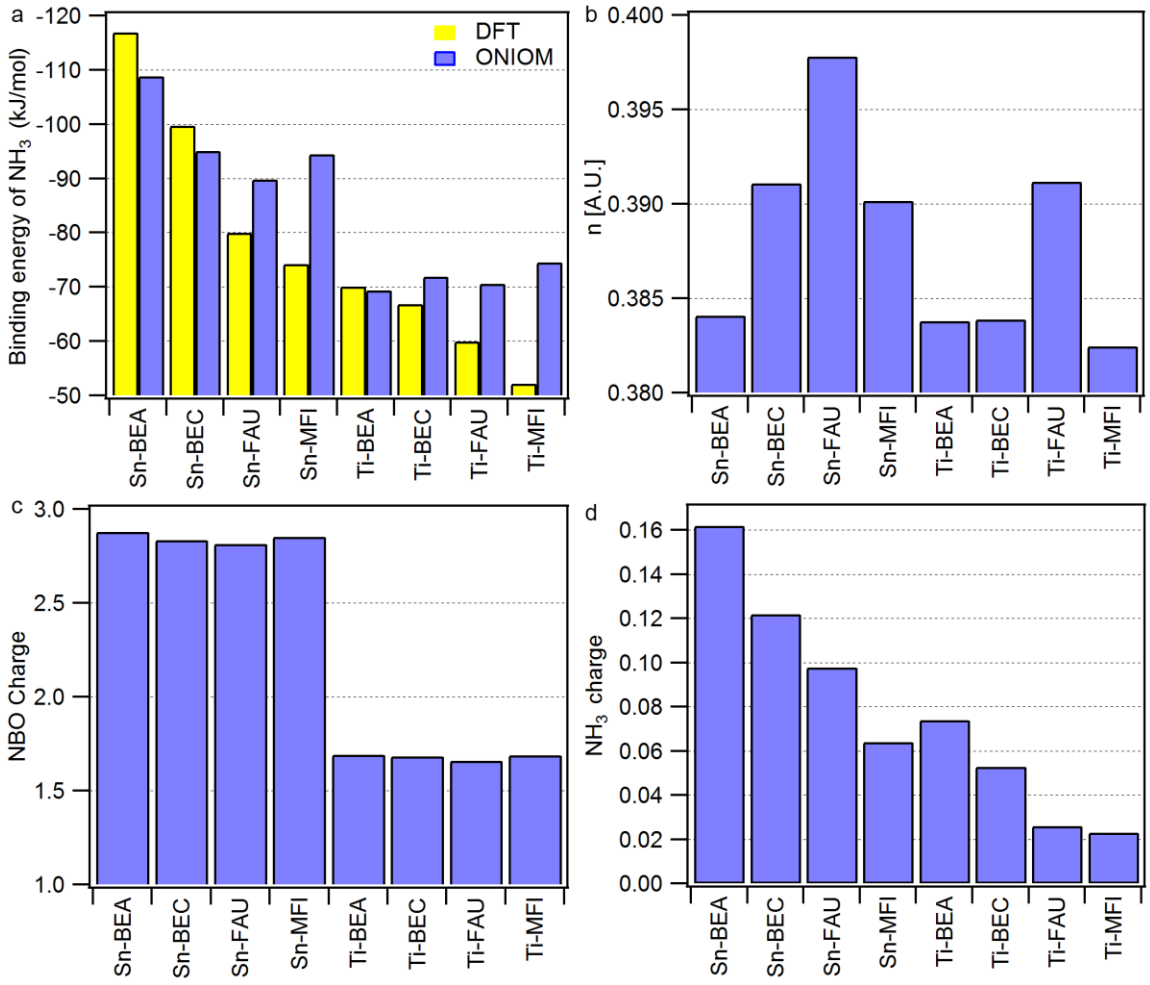

Figure 3-6. Electronic properties of metal substituted zeolites. (a) binding energies of NH3, (b) hardness, (c) NBO charge of the metal atom, (d) Charge of NH_3 upon adsorption.

Figure 3-7 shows the normalized deformation (φ) associated to the substitution of Ti and Sn in the zeolite frameworks. This parameter was obtained with the mean square deviations, θ, that describes the deviation of the [MO_4] from a regular tetrahedron, and it was calculated using Equation 3-4.[3]

$$\theta = \sqrt{\frac{1}{6}\sum_{i=1}^{6}(\alpha_i - \bar{\alpha})^2} \quad \textbf{(3-4)}$$

In this equation, α_i represents the ith θ(O-T-O) angle, and $\bar{\alpha}$ is the average of the six θ(O-T-O) angles. The parameter θ is not a direct measure of the deformation caused by the substitution of the metal in the zeolite. The normalized deformation (φ) of each θ_M has to be calculated with respect to the values corresponding to the pure zeolite θ_{Si}, as described in Equation 3-5.

$$\varphi = \frac{(\theta_M - \theta_{Si})}{\theta_{Si}} \quad \textbf{(3-5)}$$

In all the zeolites, the deformation caused by Sn is higher than the deformation caused by Ti. This is expected because Sn has a larger radius than Ti. Our results are consistent with previous studies. For instance, Yang and coworkers reported higher deformation for the substitution of Sn in BEA compared to the deformation caused by the substitution of Ti.[4] These deformation parameters have been correlated with the stabilities of the zeolites.[3,4] On the basis of this parameter, the zeolites are more stable with the substitution of Ti than of Sn. MFI is the framework with the lowest deformations for Sn- and Ti- substituted zeolites, indicating that MFI is more stable than the other metal-substituted zeolites upon substitution of Sn or Ti. The deformation parameters were also calculated using the ONIOM clusters depicted in Figure 3-2 and Figure 3-3, but no significant variations were obtained between the methods.

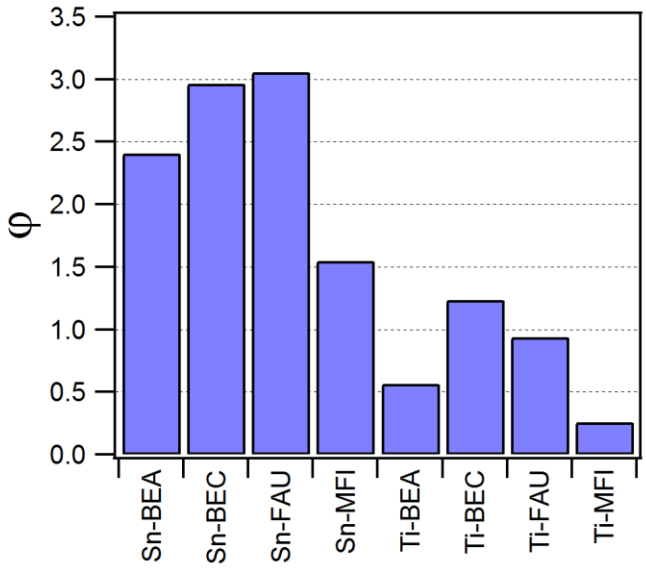

Figure 3-7. Local structural perturbation at the T-Site of the metal substituted zeolites

3.3.4.2 Comparison of the Lewis acidity between the closed sites and the open sites

Figure 3-8 shows the hardness and the LUMO energies of the metal-substituted zeolites. On the basis of Figure 3-8, the formation of defects decreases the hardness of the zeolites. The hardness of hydrolyzed Sn-BEA, Sn-MFI, Ti-BEA, Ti-BEC, and Ti-MFI are significantly lower compared to the non-hydrolyzed zeolites. However, Sn-BEC, Sn-FAU, and Ti-FAU do not exhibit significant change in their hardness upon hydrolysis.

While the adsorption of a probe molecule, such as NH_3, is commonly used to describe the Lewis acidity of a system, in hydrolyzed zeolites, NH_3 can interact with the Lewis sites or with the Brønsted site of the zeolites. Therefore, the binding energy of NH_3 on a hydrolyzed metal-substituted zeolite is not necessarily correlated to the Lewis acidity of the system. In this study, the Lewis acidities of the hydrolyzed zeolites were, thus, correlated to the LUMO energies. As the LUMO energy decreases, the zeolite could gain electronic density easier, resulting in a higher Lewis acidity. Sastre and Corma employed the LUMO energies of Ti-BEA and Ti-MFI as

descriptors of the Lewis acidity.[50] In this work, however, the LUMO energies were only used to compare the Lewis acidities of the open and closed sites of the same metal-substituted zeolite.

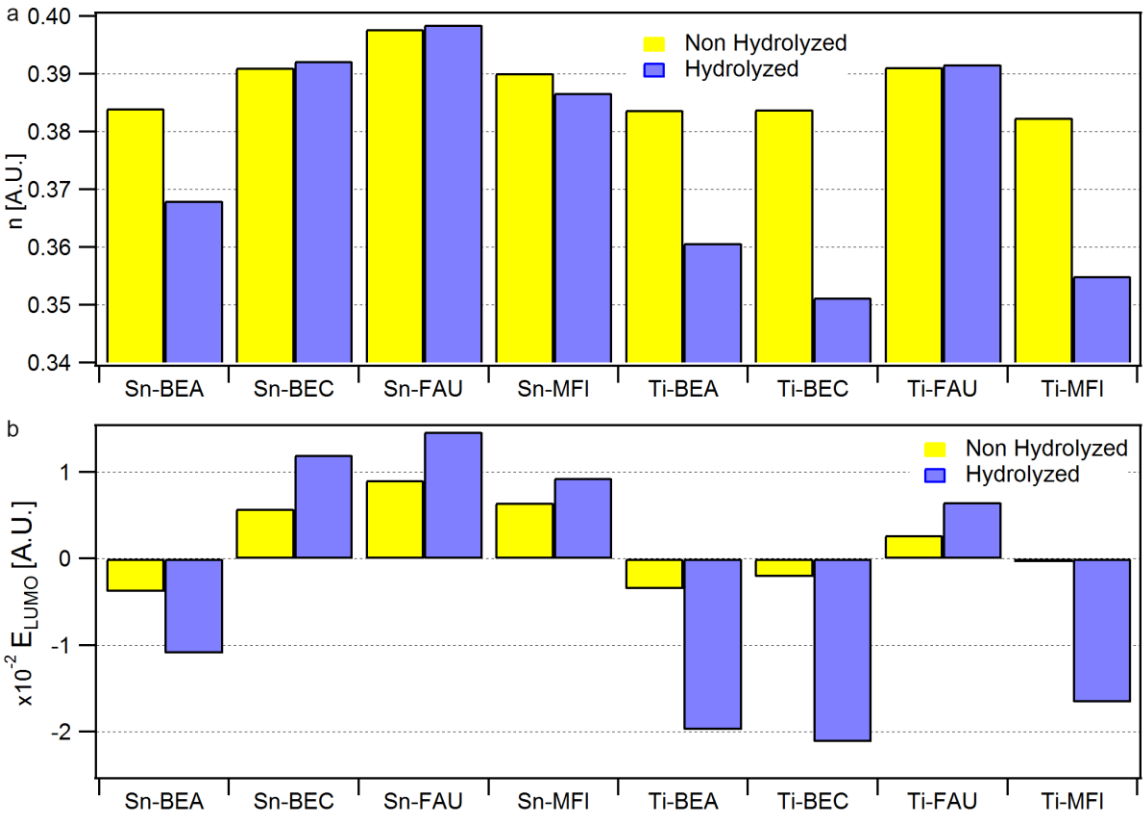

Figure 3-8. Comparison of electronic properties of the hydrolyzed and non-hydrolyzed metal-substituted zeolites obtained in vacuum. (a) Hardness, (b) LUMO energies.

Based on the LUMO energies (Figure 3-8b), the open sites of Sn-BEA, Ti-BEA, Ti-BEC and Ti-MFI have higher Lewis acidity than their closed sites. On the contrary, the open sites of Sn-BEC, Sn-FAU, Sn-MFI and Ti-FAU have lower Lewis acidity than the open sites. Wells and coworkers determined through a DFT study that the open sites in Ti-MFI are more reactive in the propylene epoxidation reaction than the closed sites.[21] Based on the LUMO energies, our results also suggest that the open sites in Ti-MFI exhibit higher Lewis acidity than the closed sites. This is also in agreement with the study of Boronat and coworkers, in which they reported that the open sites in Sn-BEA have higher catalytic activity than the closed sites for oxidation reactions.[5] They

reported that a higher concentration of open sites promoted the Baeyer-Villiger oxidation of ketones. Boronat and coworkers corroborated this, by performing a FTIR study through the adsorption of acetonitrile in both sites of Sn-BEA.[43] On the basis of the LUMO energies, our study also suggests that the open sites of Sn-BEA exhibit higher Lewis acidity than the closed sites. Boronat and coworkers also performed DFT calculations on the open sites of Sn-MFI.[43] Their results, based on the adsorption of acetonitrile, suggest that the open and closed sites of Sn-MFI have similar Lewis acidities. Based on our results, however, the open sites in Sn-MFI have lower Lewis acidity than the closed sites.

3.3.4.3 Lewis acidity of the metal-substituted zeolites in water

Figure 3-9 shows the binding energies of the metal substituted zeolites with NH_3 in water calculated with the ONIOM clusters depicted in Figure 3-2. The binding energies were calculated with two explicit water molecules and a PCM in order to take into account the effect of the water as is shown in Scheme 3-3. As shown in Table B-12, the NH_3 binding energies with the solvent vary significantly when compared to the energies obtained in vacuum. Based on the binding energies with water as the solvent, Sn-BEA has the lowest binding energy, and the Lewis acidities of the metal-substituted zeolites decrease as follows: Sn-BEA > Sn-FAU > Sn-BEC > Ti- FAU > Sn-MFI > Ti-BEC > Ti-MFI > Ti-BEA.

Scheme 3-3. Adsorption of NH_3 on the metal substituted zeolites in water.

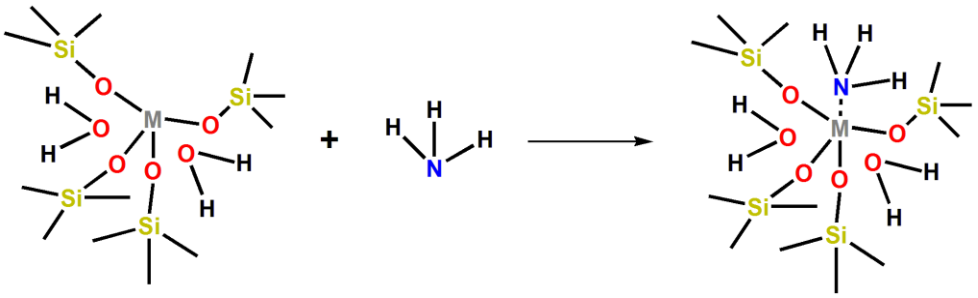

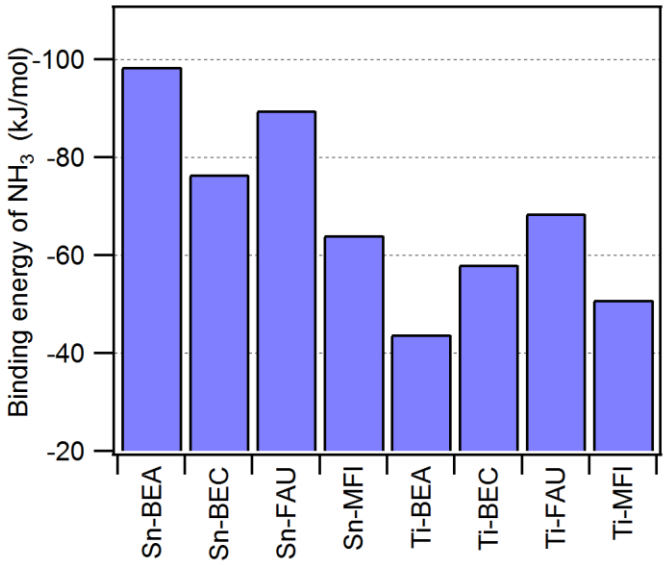

Figure 3-9. Binding energies of metal substituted zeolites of NH_3 in water.

In our results, the NH_3 binding energies increase when water is taken into account when compared to the vacuum systems. This tendency could be associated with the competition for the Lewis acidic site between NH_3 and water due to the Lewis basic characters of these molecules.

3.5 Comparison Between a Single and a Double Substitution of Sn in BEA.

Experimentally, the incorporation of Sn in BEA has been obtained through two different methods: the hydrothermal synthesis,[34] and the dealumination of Al-BEA, followed by the insertion of Sn.[35,36] In the hydrothermal synthesis, the insertion of Sn occurs during the crystallization, and the structure is usually formed without defects. It has been determined experimentally that, through the hydrothermal synthesis, the Sn atoms are substituted simultaneously in two T2 sites, as depicted in Figure 3-1e.[28] However, when Sn-BEA is synthesized by the dealumination of Al-BEA, the insertion of Sn in BEA depends upon the position of Al in the framework. We calculated the preferential location of Al in BEA, by employing the same level of theory presented in the Methodology. As shown in Table B-9 in the Appendix B, our results indicate that the preferred substitution site for Al in BEA is also T2. Hence, the analysis

of Sn-BEA with a single Sn substitution was also performed with Sn in the T2 site, as illustrated in Figure 3-1a.

Table 3-1 shows the electronic properties of BEA with a single Sn substitution (Sn-1-BEA) and with a double Sn substitution (Sn-BEA) in the framework. The table shows the binding energies of NH_3 obtained with the DFT clusters, and with the ONIOM clusters in vacuum. On the basis of the NH_3 binding energies, Sn-BEA with a double Sn substitution exhibits a higher Lewis acidity than Sn-1-BEA. Table 3-1 also compares the hydrolysis energies of the two systems, and based on these energies, the hydrolysis of the closed sites in Sn-BEA is more favorable than Sn-1-BEA.

Furthermore, on the basis of the deprotonation energies, the open sites of Sn-BEA (1241 kJ/mol) have a similar Brønsted acidity to those in Sn-1-BEA (1248 kJ/mol). Finally, the LUMO energies and the hardness of the hydrolyzed systems are also reported in Table 3-1. These results indicate that the open sites in Sn-BEA have higher Lewis acidity and a lower hardness than the open sites in Sn-1-BEA, suggesting that Sn-BEA would be more reactive than Sn-1-BEA.

In summary, based in the results presented in Table 3-1, the hydrothermal synthesis of Sn-BEA, which provides a double Sn substitution in the beta framework, results in a catalyst with higher Lewis acidity and similar Brønsted acidity than the dealumination process.

Table 3-1. Electronic properties of Sn-1-BEA (single substitution) and Sn-BEA (double substitution).

	$E_{BE\text{-}NH3}$ DFT-vacuum (kJ/mol)	$E_{BE\text{-}NH3}$ ONIOM-vacuum (kJ/mol)	$E_{Hydrolysis}$ ONIOM-solvent (kJ/mol)	**DPE** kJ/mol	ε_{LUMO} (A.U) hydrolyzed zeolite in vacuum	η (A.U.) vacuum	η (A.U) vacuum hydrolyzed zeolite
Sn-1-BEA	-99	-97	12	1248	0.0188	0.3912	0.3999
Sn-BEA	-117	-109	-24	1241	-0.0109	0.3841	0.3681

3.4 CONCLUSIONS

Our results demonstrate that the preferential location for the substitution of Sn and Ti in BEC is T1. The substitution of Ti in MFI is slightly more preferential in T10 and T11, but the difference in energies among the different sites is small. Among the metal-substituted zeolites studied, Sn-BEA has the highest Lewis acidity, which is manifested in the low binding energy of NH_3, the low hardness, and the highest charge transfer from NH_3 to the zeolite. Furthermore, open sites in Sn-BEA form Brønsted acid sites, providing a double functionality to the catalyst, while also increasing the Lewis acidity. Our results also demonstrate that the formation of open sites through the hydrolysis of Sn-BEA and Sn-FAU is energetically favorable. However, the hydrolysis reactions to create such sites in Sn- Ti- MFI are not favorable. We also demonstrated that the VDW forces in the NH_3 binding energy on MFI are more significant than in BEA, BEC, and FAU zeolites, and VDW forces decrease with increasing pore size.

3.5 REFERENCES

(1) Lew, C. M.; Rajabbeigi, N.; Tsapatsis, M. Tin-Containing Zeolite for the Isomerization of Cellulosic Sugars. *Microporous Mesoporous Mater.* **2012**, *153*, 55–58.

(2) Osmundsen, C. M.; Holm, M. S.; Dahl, S.; Taarning, E. Tin-Containing Silicates: Structure-Activity Relations. *Proc. R. Soc. A Math. Phys. Eng. Sci.* **2012**, *468*, 2000–2016.

(3) Yang, G.; Zhou, L.; Han, X. Lewis and Brönsted Acidic Sites in M^{4+}-Doped Zeolites (M = Ti, Zr, Ge, Sn, Pb) as Well as Interactions with Probe Molecules: A DFT Study. *J. Mol. Catal. A Chem.* **2012**, *363-364*, 371–379.

(4) Yang, G.; Pidko, E. a.; Hensen, E. J. M. Structure, Stability, and Lewis Acidity of Mono and Double Ti, Zr, and Sn Framework Substitutions in BEA Zeolites: A Periodic Density Functional Theory Study. *J. Phys. Chem. C* **2013**, *117*, 3976–3986.

(5) Boronat, M.; Concepcion, P.; Corma, a; Renz, M.; Valencia, S. Determination of the Catalytically Active Oxidation Lewis Acid Sites in Sn-Beta Zeolites, and Their Optimisation by the Combination of Theoretical and Experimental Studies. *J. Catal.* **2005**, *234* , 111–118.

(6) Jones, A. J.; Carr, R. T.; Zones, S. I.; Iglesia, E. Acid Strength and Solvation in Catalysis by MFI Zeolites and Effects of the Identity, Concentration and Location of Framework Heteroatoms. *J. Catal.* **2014**, *312*, 58–68.

(7) Assary, R. S.; Curtiss, L. A.; Dumesic, J. A. Exploring Meerwein–Ponndorf–Verley Reduction Chemistry for Biomass Catalysis Using a First-Principles Approach. *ACS Catal.* **2013**, *3*, 2694–2704.

(8) Román-Leshkov, Y.; Davis, M. E. Activation of Carbonyl-Containing Molecules with Solid Lewis Acids in Aqueous Media. *ACS Catal.* **2011**, *1*, 1566–1580.

(9) Moliner, M.; Román-Leshkov, Y.; Davis, M. E. Tin-Containing Zeolites Are Highly Active Catalysts for the Isomerization of Glucose in Water. *Proc. Natl. Acad. Sci. U. S. A.* **2010**, *107*, 6164–6168.

(10) International Zeolite Association (IZA). http://izasc.fos.su.se/fmi/xsl/IZA-SC/ft.xsl (accessed Jan 6, 2016).

(11) Wolf, P.; Valla, M.; Rossini, A. J.; Comas-Vives, A.; Núñez-Zarur, F.; Malaman, B.; Lesage, A.; Emsley, L.; Copéret, C.; Hermans, I. NMR Signatures of the Active Sites in Sn-β Zeolite. *Angew. Chemie - Int. Ed.* **2014**, *53*, 10179–10183.

(12) Corma, A.; Domine, M. E.; Nemeth, L.; Valencia, S. Al-Free Sn-Beta Zeolite as a Catalyst for the Selective Reduction of Carbonyl Compounds (Meerwein-Ponndorf-Verley Reaction). *J. Am. Chem. Soc.* **2002**, *124*, 3194–3195.

(13) Szostak, R.; Pan, J. M.; Lillerud, K. P. High-Resolution TEM Imaging of Extreme Faulting in Natural Zeolite Tschernichite. *J. Phys. Chem.* **1995**, *99*, 2104–2109.

(14) West, R. M.; Holm, M. S.; Saravanamurugan, S.; Xiong, J.; Beversdorf, Z.; Taarning, E.; Christensen, C. H. Zeolite H-USY for the Production of Lactic Acid and Methyl Lactate from C_3-Sugars. *J. Catal.* **2010**, *269*, 122–130.

(15) Lee, F. Y.; Lv, L.; Su, F.; Liu, T.; Liu, Y.; Sow, C. H.; Zhao, X. S. Incorporation of Titanium into Polymorph C for Catalytic Epoxidation of Cyclohexene. *Microporous Mesoporous Mater.* **2009**, *124*, 36–41.

(16) Moliner, M.; Serna, P.; Cantin, A.; Sastre, G.; Diaz-Cabanas, M. J.; Corma, A. Synthesis of the Ti-Silicate Form of BEC Polymorph of β-Zeolite Assisted by Molecular Modeling. *J. Phys. Chem. C* **2008**, *112*, 19547–19554.

(17) Oumi, Y.; Manabe, T.; Sasaki, H.; Inuzuka, T.; Sano, T. Preparation of Ti Incorporated Y Zeolites by a Post-Synthesis Method under Acidic Conditions and Their Catalytic Properties. *Appl. Catal. A Gen.* **2010**, *388*, 256–261.

(18) Wang, X. X.; de Mallmann, A.; Bayard, F.; Lefebvre, F.; Basset, J. M. Study of the Reaction of Tetramethyltin with H-Faujasite. Characterization of the Grafted Species and Thermal Stability. *Microporous Mesoporous Mater.* **2003**, *63*, 147–161.

(19) Corma, A.; Navarro, M. T.; Rey, F.; Rius, J.; Valencia, S. Pure Polymorph C of Zeolite Beta Synthesized by Using Framework Isomorphous Substitution as a Structure-Directing Mechanism. *Angew. Chem. Int. Ed. Engl* **2001**, *40*, 2277–2280.

(20) Kulkarni, B. S.; Krishnamurty, S.; Pal, S. Probing Lewis Acidity and Reactivity of Sn- and Ti-Beta Zeolite Using Industrially Important Moieties: A Periodic Density Functional Study. *J. Mol. Catal. A Chem.* **2010**, *329*, 36–43.

(21) Wells, D. H.; Delgass, W. N.; Thomson, K. T. Evidence of Defect-Promoted Reactivity for Epoxidation of Propylene in Titanosilicate (TS-1) Catalysts: A DFT Study. *J. Am. Chem. Soc.* **2004**, *126*, 2956–2962.

(22) Jones, A. J.; Zones, S. I.; Iglesia, E. Implications of Transition State Confinement within Small Voids for Acid Catalysis. *J. Phys. Chem. C* **2014**, *118*, 17787–17800.

(23) Chai, J.-D.; Head-Gordon, M. Long-Range Corrected Hybrid Density Functionals with Damped Atom-Atom Dispersion Corrections. *Phys. Chem. Chem. Phys.* **2008**, *10*, 6615–6620.

(24) Hay, P. J.; Wadt, W. R. Ab Initio Effective Core Potentials for Molecular Calculations. Potentials for K to Au Including the Outermost Core Orbitals. *J. Chem. Phys.* **1985**, *82*, 299–310.

(25) Andrae, D.; Häußermann, U.; Dolg, M.; Stoll, H.; Preuß, H. Energy-Adjusted Ab Initio Pseudopotentials for the Second and Third Row Transition Elements. *Theor. Chim. Acta* **1990**, *77*, 123–141.

(26) Montejo-Valencia, B. D.; Curet-Arana, M. C. DFT Study of the Lewis Acidities and Relative Hydrothermal Stabilities of BEC and BEA Zeolites Substituted with Ti, Sn, and Ge. *J. Phys. Chem. C* **2015**, *119*, 4148–4157.

(27) Weinhold, F.; Carpenter, J. *The Structure of Small Molecules and Ions*; Naaman, R., Vager, Z., Eds.; Springer US: (Plenum, New York), 1988.

(28) Bare, S. R.; Kelly, S. D.; Sinkler, W.; Low, J. J.; Modica, F. S.; Valencia, S.; Corma, A.; Nemeth, L. T. Uniform Catalytic Site in Sn-β-Zeolite Determined Using X-Ray Absorption Fine Structure. *J. Am. Chem. Soc.* **2005**, *127*, 12924–12932.

(29) Rappe, a. K.; Casewit, C. J.; Colwell, K. S.; Goddard III, W. a.; Skiff, W. M. UFF, a Full Periodic Table Force Field for Molecular Mechanics and Molecular Dynamics Simulations. *J. Am. Chem. Soc.* **1992**, *114*, 10024–10035.

(30) Svelle, S.; Tuma, C.; Rozanska, X.; Kerber, T.; Sauer, J. Quantum Chemical Modeling of Zeolite-Catalyzed Methylation Reactions: Toward Chemical Accuracy for Barriers. *J. Am. Chem. Soc.* **2009**, *131*, 816–825.

(31) Singh, U. C.; Kollman, P. A. An Approach to Computing Electrostatic Charges for Molecules. *J. Comput. Chem.* 1984, 5, 129–145.

(32) Besler, B. H.; Merz, K. M.; Kollman, P. A. Atomic Charges Derived from Semiempirical Methods. *J. Comput. Chem.* **1990**, *11*, 431–439.

(33) Frisch, M. J.; Trucks, G. W.; Schlegel, H. B.; Scuseria, G. E.; Robb, M. A.; Cheeseman, J. R.; Scalmani, G.; Barone, V.; Mennucci, B.; Petersson, G. A. . et al. Gaussian 09. Gaussian, Inc., Wallingford CT 2009.

(34) Corma, A.; Nemeth, L. T.; Renz, M.; Valencia, S. Sn-Zeolite Beta as a Heterogeneous Chemoselective Catalyst for Baeyer-Villiger Oxidations. *Nature* **2001**, *412*, 423–425.

(35) Hammond, C.; Conrad, S.; Hermans, I. Simple and Scalable Preparation of Highly Active Lewis Acidic Sn-β. *Angew. Chemie - Int. Ed.* **2012**, *51*, 11736–11739.

(36) van der Graaff, W. N. P.; Li, G.; Mezari, B.; Pidko, E. a; Hensen, E. ;J. M. Synthesis of Sn-Beta with Exclusive and High Framework Sn Content. *ChemCatChem* **2015**, *7*, 1152–1160.

(37) Sastre, G.; Vidal-Moya, J. a; Blasco, T.; Rius, J.; Jordá, J. L.; Navarro, M. T.; Rey, F.; Corma, A. Preferential Location of Ge Atoms in Polymorph C of Beta Zeolite (ITQ-17) and Their Structure-Directing Effect: A Computational, XRD, and NMR Spectroscopic Study. *Angew. Chem. Int. Ed. Engl.* **2002**, *41*, 4722–4726.

(38) Lamberti, C.; Bordiga, S.; Zecchina, a.; Carati, a.; Fitch, a. N.; Artioli, G.; Petrini, G.; Salvalaggio, M.; Marra, G. L. Structural Characterization of Ti-Silicalite-1: A Synchrotron Radiation X-Ray Powder Diffraction Study. *J. Catal.* **1999**, *183*, 222–231.

(39) Marra, G. L.; Artioli, G.; Fitch, a. N.; Milanesio, M.; Lamberti, C. Orthorhombic to Monoclinic Phase Transition in High-Ti-Loaded TS-1: An Attempt to Locate Ti in the MFI Framework by Low Temperature XRD. *Microporous Mesoporous Mater.* **2000**, *40*, 85–94.

(40) Yang, G.; Lan, X.; Zhuang, J.; Ma, D.; Zhou, L.; Liu, X.; Han, X.; Bao, X. Acidity and Defect Sites in Titanium Silicalite Catalyst. *Appl. Catal. A Gen.* **2008**, *337*, 58–65.

(41) Zhuang, J.; Ma, D.; Yan, Z.; Deng, F.; Liu, X.; Han, X.; Bao, X.; Liu, X. W.; Guo, X.; Wang, X. Solid-State MAS NMR Detection of the Oxidation Center in TS-1 Zeolite by in Situ Probe Reaction. *J. Catal.* **2004**, *221*, 670–673.

(42) Lamberti, C.; Bordiga, S.; Zecchina, A.; Artioli, G.; Marra, G.; Spanò, G. Ti Location in the MFI Framework of Ti-Silicalite-1: A Neutron Powder Diffraction Study. *J. Am. Chem. Soc.* **2001**, *123*, 2204–2212.

(43) Boronat, M.; Concepcion, P.; Corma, A.; Navarro, M. T.; Renz, M.; Valencia, S. Reactivity in the Confined Spaces of Zeolites: The Interplay between Spectroscopy and Theory to Develop Structure-Activity Relantionships for Catalysis. *Phys. Chem. Chem. Phys.* **2009**, *11*, 2876–2884.

(44) Davies, L. J.; McMorn, P.; Bethell, D.; Page, P. C. B.; King, F.; Hancock, F. E.; Hutchings, G. J. Epoxidation of Crotyl Alcohol Using Ti-Containing Heterogeneous Catalysts: Comments on the Loss of Ti by Leaching. *J. Catal.* **2001**, *198*, 319–327.

(45) Carati, A.; Flego, C.; Previde Massara, E.; Millini, R.; Carluccio, L.; Parker, W.; Bellussi, G. Stability of Ti in MFI and Beta Structures: A Comparative Study. *Microporous Mesoporous Mater.* **1999**, *30*, 137–144.

(46) Wang, N.; Zhang, M.; Yu, Y. Density Functional Calculations on the Distribution of Ti in a Y Zeolite and Its Influence on Acidity. *RSC Adv.* **2014**, *4*, 4324–4329.

(47) Janchen, J.; Vorbeck, G.; Stach, H.; Parlitz, B.; van Hooff, J. H. . Adsorption Calorimetric and Spectroscopic Studies on Isomorphous Substituted (AI, Fe, In, Ti) MFI Zeolites. In *Catalysis by Microporous Materials*; Beyer, H. ., Karge, H. ., Kiricsi, I., Nagy, J. ., Eds.; Elsevier Science Ltd, 1995; Vol. 94, pp 108–115.

(48) Jones, A. J.; Iglesia, E. The Strength of Brønsted Acid Sites in Microporous Aluminosilicates. *ACS Catal.* **2015**, *5* (10), 5741–5755.

(49) Pearson, R. G. Chemical Hardness and Density Functional Theory. *J. Chem. Sci.* **2005**, *117*, 369–377.

(50) Sastre, G.; Corma, A. Relation between Structure and Lewis Acidity of Ti-Beta and TS-1 Zeolites : A Quantum-Chemical Study. *Chem. Phys. Lett.* **1999**, *302*, 447–453.

4 CHAPTER - CLOSED SITES OF M-BETA (M = SN, TI, ZR, OR HF) ZEOLITES CAN OPEN GLUCOSE AND FRUCTOSE RINGS IN ONE ELEMENTARY STEP.

4.1 INTRODUCTION

Lignocellulosic biomass is an abundant and inexpensive raw material from which high value added chemicals can be produced.[1] It is primarily composed of cellulose and hemicellulose, which can be decomposed into sugars through an acid hydrolysis.[2] Glucose is the main sugars obtained from this hydrolysis. Previous studies have demonstrated that Lewis acid catalysts, such as Sn-BEA, can catalyze the glucose – fructose isomerization. The catalytic path for the conversion of glucose with a Lewis catalyst is shown in Figure 4-1.

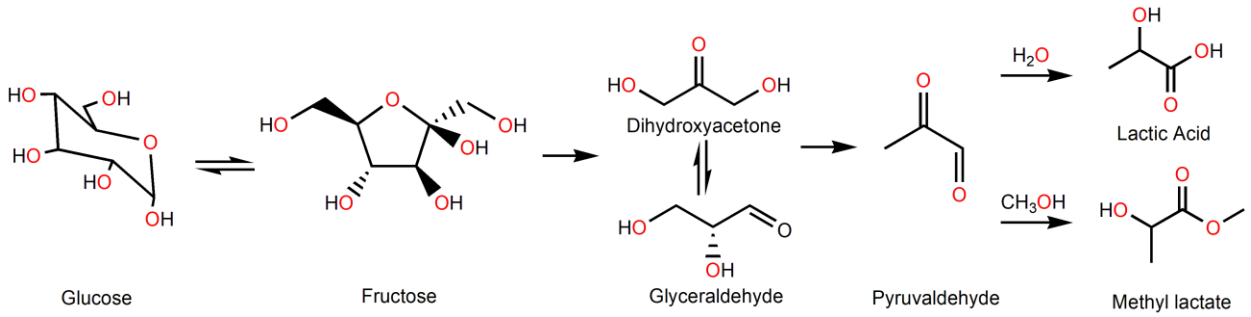

Figure 4-1. Catalytic path for the conversion of glucose with a Lewis catalyst.

Despite the outstanding performance of Sn-BEA, the selective conversion of these sugars, however, is still a challenge. Previous studies have focused in optimizing the above paths by varying the solvents and catalysts.[3–8] However, yields to obtain lactic acid from these sugars with Sn-BEA catalysts are below 30%. These yields are mainly due to the Brønsted acid nature of lactic acid, which can catalyze the reaction through other paths that produce hydroxymethylfurfural (HMF) and levulinic acid.[6] Furthermore, the vast number of functional groups in biomass-derived molecules imposes a major challenge on these reaction systems.

Since glucose is directly obtained from biomass hydrolysis, much effort has been put forth in understanding how glucose interacts and reacts on Sn-BEA. Previous studies on the reaction mechanism of glucose to fructose isomerization agree that the hydride shift from two adjacent carbon atoms within the molecule is the rate limiting step.[9–12] Despite the significant progress made to elucidate the mechanism for the conversion of glucose to fructose, further studies are still necessary to clarify how the glucose ring opens. For instance, it has been proposed that the opening of the glucose ring can occur through two different paths as shown in Figure 4-2.[10–12] These reaction mechanisms consist of two steps for the hydride shift on glucose from O1 to O5. The main difference between the mechanisms illustrated in Figure 4-2 is on the adsorption of glucose, which has been proposed to occur through O1[10,12] or O5[11]. We note that Yang and coworkers also performed periodic DFT calculations on the reaction mechanisms in Figure 4-2, but they analyzed closed sites instead of hydrolyzed sites.[12] Here we propose a third path for the opening of glucose that involves only one step with a lower energy barrier than the reaction mechanisms that have been previously proposed in the literature.

To our knowledge, the mechanism for the opening of the fructose ring by metal substituted zeolites has not been reported in the literature. In this study, we analyzed the opening of fructose and glucose rings on zeolite beta (BEA) substituted with tin (Sn), hafnium (Hf), titanium (Ti), and zirconium (Zr). Our results demonstrate that M-BEA can catalyze the ring opening of glucose and fructose in only one elementary step due to the synergistic effect of the closed sites of M-BEA with the molecule. Furthermore, the transition state (TS) energy for the glucose opening in Sn-BEA (96.9 kJ/mol) is lower than those reported previously (129 and 194 kJ/mol).[12] Moreover, the apparent activation energies of fructose opening on Hf-BEA and Zr-BEA are significantly lower than the one obtained on Sn-BEA, suggesting that in reactions involving the conversion of fructose

through a Lewis acid catalyst, Hf-BEA and Zr-BEA could exhibit better performance than Sn-BEA.

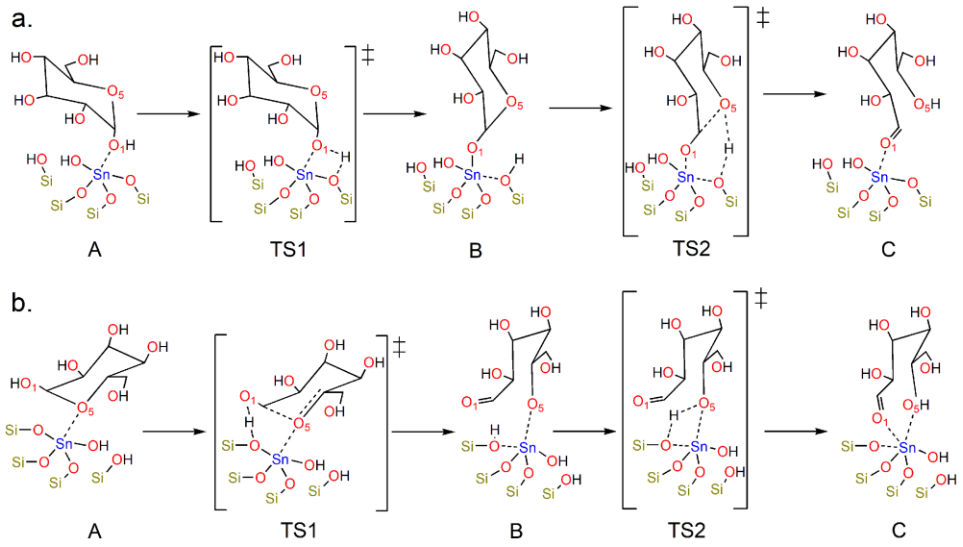

Figure 4-2. Previously reported reaction mechanisms for the glucose ring opening on Sn-BEA. (a) Reaction mechanism proposed by Li and coworkers[10] (b) Reaction mechanism proposed by Bermejo-Deval and coworkers.[11]

4.2 METHODOLOGY

In this work, the ring opening of glucose and fructose on M-BEA was analyzed using periodic DFT calculations. As shown in Figure 4-3, α-D-Glucopyranose (GP) and β-D-fructofuranose (FF) were selected as the conformers of glucose and fructose, respectively. We analyzed the polymorphism A of zeolite beta and used the coordinates as reported by the International Zeolite Association (IZA).[13] BEA has a tetragonal unit cell with lattice parameters: a = b = 12.6 Å and c = 26.2 Å, and has nine crystallographic sites, as shown in Figure C- 1 in the Appendix C. Metal substituted BEA zeolites (M-BEA) were analyzed with Sn, Hf, Zr, and Ti. The calculations were performed using the Vienna ab initio simulation package (VASP 5.4)[14,15] with the generalized gradient approximation Perdew–Burke–Ernzrhof (PBE) exchange-correlation.[16,17] Standard PAW potentials[15,18] were used for all the elements, except for the metal atoms, for which higher

electronic PAW pseudopotentials were used instead of the default ones. Thus, for the substituted metals, we employed Sn (Sn_d), Hf (Hf_pv), Zr (Zr_sv), and Ti (Ti_sv) to treat their semicores s, p, or d as valence states.[19] The dispersion interactions were taken into account with the DFT-D3 method.[20] The Brillouin zone sampling was restricted to the G-point. The energy cutoff was set to 500 eV. Full geometry optimizations were performed with fixed cell parameters. The nudged elastic band method (NEB) was used to determine the minimum energy path and to locate the transition-state (TS) structures.[21,22] Then, the climbing image NEB method was used to obtain the saddle point.[23] The TS were confirmed by frequency calculations involving only the motions of the atoms of the adsorbed molecules, as well as the metal substituted with its four bonded oxygens. We obtained two imaginary frequencies for the fructose ring opening in Sn-BEA (1381 cm^{-1}, 21 cm^{-1}) and Ti-BEA (1442 cm^{-1}, 11 cm^{-1}), and the smaller ones nearing zero were ignored. The rest of the TS frequencies showed only one imaginary frequency.

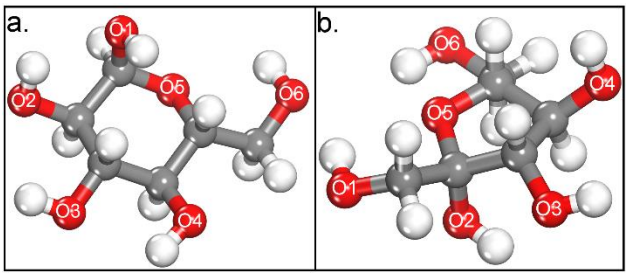

Figure 4-3. Glucose (a) and fructose (b) molecules. Color legend: red=oxygen, gray=carbon, white=hydrogen. Oxygen atoms are labeled from O1 to O6.

4.3 RESULTS AND DISCUSSION

The preferential substitution sites for Sn, Hf, Zr, and Ti in BEA were calculated by replacing the metal in each T-Site of the zeolite and optimizing the BEA unit cell structure. The nine T-sites of BEA are illustrated in Figure C- 1 in the Appendix C. As shown in the Supporting Information, our calculations demonstrate that the most stable substitution site for all the metal atoms in BEA

is in the T6 site, in agreement with experimental and other computational results.[24–27] For instance, Bare and co-workers, using EXAFS spectroscopy, found that the substitution of Sn in BEA is predominantly in the T6 site.[24] Furthermore, previous works with DFT calculations have demonstrated that the preferential substitution site of Zr and Ti in BEA is also in T6.[25–27] As far as we know, studies on the substitution of Hf in BEA have not been reported, but based on our results, the preferred substitution site for Hf in BEA is also in T6. In this work, all the calculations involving the adsorption of fructose and glucose were performed with the metal atoms substituted in the T6 site of BEA.

The adsorption energies of glucose on M-BEA were calculated through each of the oxygen atoms of the adsorbate, which are identified in Figure 4-3a. The different adsorption energies for glucose on M-BEA are shown in Figure 4-4(a). The optimized adsorbed structures were obtained in monodentate configurations, which have been reported to be energetically more favorable than the bidentate modes.[28] For instance, Yang and coworkers reported adsorption energies of cyclic glucose on Ti-BEA, and the lowest value reported is -123 kJ/mol in a monodentate configuration, whereas the adsorption energy is -98 kJ/mol in a bidentante configuration.[28] The distances between the adsorbed oxygen of the glucose and the metal of M-BEA vary between 2.22 to 3.37 Å, as shown on Table S1 and Figure C- 6 in the Appendix C. In general, the O-M distances obtained when the molecules adsorb through O5 are larger (2.84 - 3.37 Å) than the ones obtained through the other oxygens (2.22- 2.57 Å). This significant difference is due to the steric hindrance caused by the hydroxyl groups when the glucose is adsorbed through the O5 oxygen.

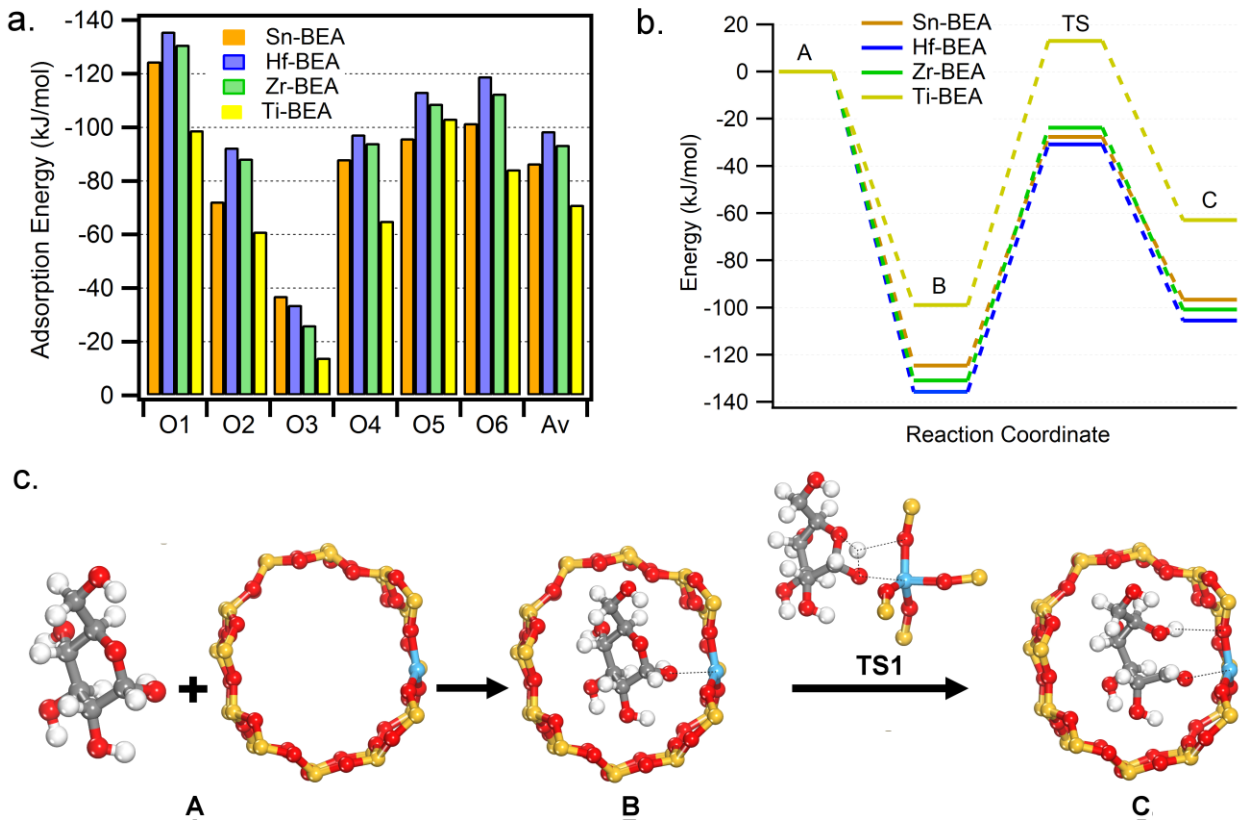

Figure 4-4. (a) Adsorption energies of glucose on M-BEA through the different oxygen atoms of the molecule. The oxygen atoms are identified in Figure 4-3(a). Av stands for the average adsorption energy. (b) Reaction energies of the opening of the glucose ring on M-BEA, and (c) the reaction mechanism for the opening of the glucose ring on M-BEA.

On the basis of Figure 4-4 (a), the adsorption energies of glucose on M-BEA is strongly affected by the nature of the metal as well as by the glucose oxygen coordinated to the metal. In average, the strongest adsorption of glucose is on Hf-BEA (-98.7 kJ/mol), followed by Zr-BEA (-93.5 kJ/mol), Sn-BEA (-86.7 kJ/mol), and Ti-BEA (-71.2 kJ/mol). Yang and co-workers reported the same trend for the adsorption of glucose in BEA zeolites substituted with Zr, Sn, and Ti.[28]

The strongest interactions of glucose on Hf-, Zr-, and Sn-BEA are through the oxygen O1 of glucose, which are below -120 kJ/mol. For Ti-BEA, the strongest interactions were obtained through O5 closely followed by O1. Previous DFT studies have reported that the isomerization of glucose to fructose on Sn-BEA starts when glucose is adsorbed on O1 or O5.[11,12]

The minimum energy path and the reaction mechanism for the glucose ring opening are shown in Figure 4-4 (b) and Figure 4-4 (c), respectively. Our calculations suggest that the glucose ring can be opened in one elementary step, in which the hydrogen atom is shifted from O1 to O5 as illustrated in the TS configuration in Figure 4-5 (a). The confinement effect of the closed sites of M-BEA allows the simultaneous interaction between several atoms of the glucose molecule and the zeolite which are manifested in the distances of the TS shown in Table 4-1. As the hydride shift occurs between O1 and O5, O1 interacts simultaneously with the metal atom (M), while the hydrogen atom interacts with one of the oxygen atoms coordinated to the metal (Oz). These interactions are reflected in the distances $d_{O1\text{-}M}$ which range between 2.20 - 2.27 Å and the distances $d_{H\text{-}Oz}$ which range between 2.43 - 2.55 Å. This TS configuration can be obtained on the closed sites of M-BEA, and it is not possible to obtain with open sites due to the steric hindrance caused by the hydrolyzed groups (M-OH, Si-OH) in the open site. The energy barriers increase as follows: Sn-BEA (96.9 kJ/mol) < Hf-BEA (104.9 kJ/mol) < Zr-BEA (107.1 kJ/mol) < Ti-BEA (111.9 kJ/mol). Thus, Sn-BEA has the lowest energy barrier for the opening of the glucose ring, and it is well known that Sn-BEA exhibits high catalytic activity for the isomerization of glucose to fructose.[4,8]

The TS energy obtained here for Sn-BEA is lower than the TS energies reported in previous works, in which the opening of the glucose ring was analyzed through two consecutive steps, as shown in Figure 4-2. TS energies reported in the literature for the opening of the glucose ring on Sn-BEA are 194 kJ/mol and 129 kJ/mol for O5 and O1 oxygen atoms of the glucose, respectively.[12] We note that we have to be careful when comparing our results with the reported energies of the reaction mechanisms of Figure 4-2 (a)[10] and Figure 4-2 (b).[11] For instance, Li and coworkers reported the reaction energies using the solvated glucose as reference, instead of the

glucose in gas phase that we are reporting.[10] On the other hand, Bermejo-Deval and coworkers reported the energies as enthalpies at 298K with a polarizable continuum model using the water dielectric constant and small cluster models.[11] However, we can compare our energies with the ones reported by Yang and coworkers.[12] They studied the reaction mechanisms illustrated in Figure 4-2, but with closed sites, and they used a similar methodology to ours. The transition state (TS) energy for the glucose opening in Sn-BEA that we obtained (96.9 kJ/mol) is lower than those reported by Yang and coworkers (129 and 194 kJ/mol).[12]

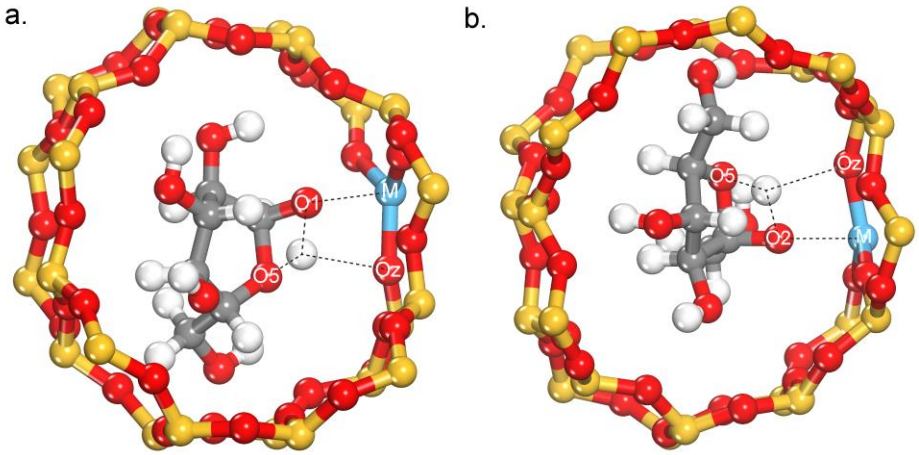

Figure 4-5. TS configurations for the opening of (a) glucose and (b) fructose rings.

Table 4-1. Optimized distances for the glucose ring opening TS on M-BEA.

	$d_{O1\text{-}H}$ (Å)	$d_{O5\text{-}H}$ (Å)	$d_{O1\text{-}M}$ (Å)	$d_{H\text{-}Oz}$ (Å)
Sn-BEA	1.34	1.19	2.22	2.45
Hf-BEA	1.33	1.19	2.24	2.43
Zr-BEA	1.34	1.19	2.27	2.46

On the basis of Figure 4-4 (b), the apparent activation energies of Hf-BEA, Sn-BEA, and Zr-BEA are similar. On the other hand, the apparent activation energy obtained for Ti-BEA is much higher when compared to the other zeolites. It is well known that Ti-BEA has a lower catalytic activity than Sn-BEA for the isomerization of glucose to fructose.[3,29] The reaction energies for the

conversion of the adsorbed cyclic glucose to adsorbed acyclic glucose increase as follows: Sn-BEA (28.0 kJ/mol) < Zr-BEA (30.0 kJ/mol) < Hf-BEA (30.2 kJ/mol) < Ti-BEA (36.1 kJ/mol).

The adsorption energies of fructose through the different oxygen atoms of the molecule on M-BEA are shown in Figure 4-6 (a). Similar to glucose, the optimized structures for the adsorption of fructose on M-BEA were obtained in monodentate configurations. The only exception is when the adsorption of fructose is through O5, in which the fructose is also coordinated to the metal atom through O6. The distances between the adsorbed oxygen of the fructose and the metal of M-BEA vary between 2.17 to 2.74 Å, as shown on Table S2 and Figure C- 7 in the Appendix C. In general, the O5-M distances obtained by the bidentate adsorption through the O5 and O6 are larger (2.55 – 2.74 Å) than the ones obtained through the other oxygens, similar to the results obtained for glucose.

The adsorption energies of fructose on M-BEA are also strongly affected by the substituted metal atom and by the fructose oxygen that is coordinated to the metal. However, the adsorption of fructose is stronger than the adsorption of glucose on M-BEA. Comparing the average values of the adsorption energies on each M-BEA catalyst, the strongest adsorption of fructose was obtained on Zr-BEA (-163.3 kJ/mol), followed by Hf-BEA (-153.9 kJ/mol), Sn-BEA (-131.8 kJ/mol) and Ti-BEA (-122.70 kJ/mol). Furthermore, on average, the strongest interaction of fructose on M-BEA are through the oxygen O2, closely followed by O1, O6, O3, O4, and O5. We note that this result differs to that reported by Yang and co-workers, in which fructose adsorbs more strongly through O4 on Sn-BEA when compared to the other oxygens.[30]

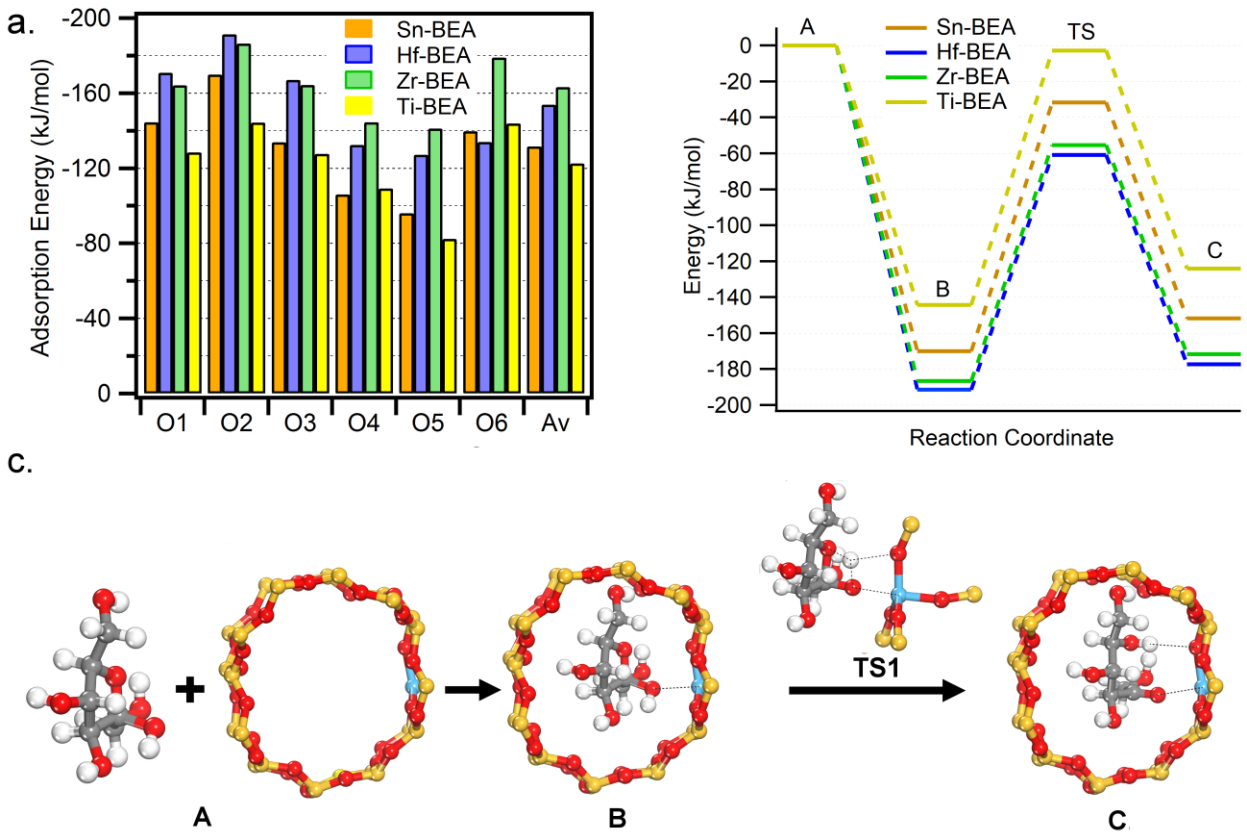

Figure 4-6. (a) Adsorption energies of fructose on M-BEA through the different oxygen atoms of the molecule. The oxygen atoms are identified in Figure 4-3(b). Av stands for the average adsorption energy. (b) Reaction energies of the opening of the fructose ring on M-BEA, and (c) the reaction mechanism for the opening of the fructose ring on M-BEA.

The minimum energy path and the reaction mechanism for the fructose ring opening are shown in Figure 4-6 (b) and Figure 4-6 (c), respectively. Figure 4-5 (b) shows the TS configuration in which the hydrogen atom is shifted directly from O2 to O5. The synergistic interactions between the closed site of the zeolite and fructose are reflected in the distances $d_{O2\text{-}M}$, and $d_{H\text{-}Oz}$ for the TS configurations. As shown in Table 2, these distances range between 2.23 - 2.34 Å for $d_{O2\text{-}M}$ and 2.29 - 2.31 Å for $d_{H\text{-}Oz}$. The energy barriers increase as follows: Hf-BEA (130.6 kJ/mol) > Zr-BEA (131.2 kJ/mol) > Sn-BEA (138.3 kJ/mol) > Ti-BEA (141.5 kJ/mol).

Table 4-2. Optimized distances for the fructose ring opening TS on M-BEA.

	$d_{O2\text{-}H}$ (Å)	$d_{O5\text{-}H}$ (Å)	$d_{O2\text{-}M}$ (Å)	$d_{H\text{-}Ozeo}$ (Å)
Sn-BEA	1.31	1.21	2.27	2.31
Hf-BEA	1.31	1.21	2.23	2.29
Zr-BEA	1.31	1.21	2.27	2.31
Ti-BEA	1.31	1.21	2.34	2.30

Based on Figure 4-6 (b), the lowest apparent activation energy for the opening of fructose is on Hf-BEA, followed by Zr-BEA, Sn-BEA, and Ti-BEA. The reaction energies for the conversion of adsorbed cyclic fructose to adsorbed acyclic fructose increase as follows: Hf-BEA (14.1 kJ/mol) < Zr-BEA (14.8 kJ/mol) < Sn-BEA (18.3 kJ/mol) < Ti-BEA (20.4 kJ/mol). After the opening of the fructose ring, the adsorbed acyclic fructose is close to its conversion to the trioses glyceraldehyde and dihydroxyacetone. The remaining steps would include the hydrogen shift between the atoms O4 to C3. Based on previous studies, the limiting step for the conversion of fructose to methyl lactate (with ethanol as solvent) or lactic acid (with water as solvent) is the formation of the trioses.[6,7] Thus, based in our results, we suggest that closed sites of Hf-BEA could perhaps achieve good yields, comparable to Sn-BEA for the conversion of fructose to lactates.

4.4 CONCLUSIONS

Our results demonstrate that the preferential site of substitution of Sn, Hf, Zr, and Ti in BEA is in T6. The adsorption of glucose and fructose in M-BEA is strongly affected by the nature of the metal and by the oxygen through which the sugar is adsorbed on the zeolite. In average, the strongest adsorption of glucose and fructose were obtained on Hf-BEA and Zr-BEA, respectively. Furthermore, the strongest interactions of glucose on M-BEA were obtained through the oxygens O1 and O5, which are the ones that trigger the isomerization reaction. Our results also demonstrate that the lowest TS energy for the glucose ring opening is obtained with Sn-BEA. On the other hand, Hf-BEA yields the lowest activation energy for the fructose ring opening.

4.5 REFERENCES

(1) Klemm, D.; Heublein, B.; Fink, H. P.; Bohn, A. Cellulose: Fascinating Biopolymer and Sustainable Raw Material. *Angew. Chemie - Int. Ed.* **2005**, *44*, 3358–3393.

(2) Zhou, C.-H.; Xia, X.; Lin, C.-X.; Tong, D.-S.; Beltramini, J. Catalytic Conversion of Lignocellulosic Biomass to Fine Chemicals and Fuels. *Chem. Soc. Rev.* **2011**, *40*, 5588–5617.

(3) Moliner, M.; Román-Leshkov, Y.; Davis, M. E. Tin-Containing Zeolites Are Highly Active Catalysts for the Isomerization of Glucose in Water. *Proc. Natl. Acad. Sci.* **2010**, *107*, 6164–6168.

(4) Osmundsen, C. M.; Holm, M. S.; Dahl, S.; Taarning, E. Tin-Containing Silicates: Structure-Activity Relations. *Proc. R. Soc. A Math. Phys. Eng. Sci.* **2012**, *468*, 2000–2016.

(5) Dapsens, P. Y.; Mondelli, C.; Pérez-Ramírez, J. Design of Lewis-Acid Centres in Zeolitic Matrices for the Conversion of Renewables. *Chem. Soc. Rev.* **2015**, *44*, 7025–7043.

(6) Holm, M. S.; Saravanamurugan, S.; Taarning, E. Conversion of Sugars to Lactic Acid Derivatives Using Heterogeneous Zeotype Catalysts. *Science* **2010**, *328*, 602–605.

(7) Dong, W.; Shen, Z.; Peng, B.; Gu, M.; Zhou, X.; Xiang, B.; Zhang, Y. Selective Chemical Conversion of Sugars in Aqueous Solutions without Alkali to Lactic Acid Over a Zn-Sn-Beta Lewis Acid-Base Catalyst. *Sci. Rep.* **2016**, *6*, 26713.

(8) Lew, C. M.; Rajabbeigi, N.; Tsapatsis, M. Tin-Containing Zeolite for the Isomerization of Cellulosic Sugars. *Microporous Mesoporous Mater.* **2012**, *153*, 55–58.

(9) Román-Leshkov, Y.; Moliner, M.; Labinger, J. A.; Davis, M. E. Mechanism of Glucose Isomerization Using a Solid Lewis Acid Catalyst in Water. *Angew. Chemie - Int. Ed.* **2010**, *49*, 8954–8957.

(10) Li, Y. P.; Head-Gordon, M.; Bell, A. T. Analysis of the Reaction Mechanism and Catalytic Activity of Metal-Substituted Beta Zeolite for the Isomerization of Glucose to Fructose. *ACS Catal.* **2014**, *4*, 1537–1545.

(11) Bermejo-Deval, R.; Assary, R. S.; Nikolla, E.; Moliner, M.; Roman-Leshkov, Y.; Hwang, S.-J.; Palsdottir, A.; Silverman, D.; Lobo, R. F.; Curtiss, L. a.; et al. Metalloenzyme-like Catalyzed Isomerizations of Sugars by Lewis Acid Zeolites. *Proc. Natl. Acad. Sci.* **2012**, *109*, 9727–9732.

(12) Yang, G.; Pidko, E. a; Hensen, E. J. M. The Mechanism of Glucose Isomerization to Fructose over Sn-BEA Zeolite: A Periodic Density Functional Theory Study. *ChemSusChem* **2013**, *6*, 1688–1696.

(13) International Zeolite Association (IZA). http://europe.iza-structure.org/IZA-SC/ftc_fw.php?STC=MFI (accessed Aug 20, 2016).

(14) Kresse, G.; Hafner, J. Ab Initio Molecular-Dynamics Simulation of the Liquid-Metal–amorphous-Semiconductor Transition in Germanium. *Phys. Rev. B* **1994**, *49*, 14251–14269.

(15) Kresse, G. From Ultrasoft Pseudopotentials to the Projector Augmented-Wave Method. *Phys. Rev. B* **1999**, *59*, 1758–1775.

(16) Perdew J. P, B. K.; Ernzerhof, M. Generalized Gradient Approximation Made Simple. *Phys. Rev. Lett.* **1996**, *77*, 3865–3868.

(17) Perdew, J. P.; Burke, K.; Ernzerhof, M. Generalized Gradient Approximation Made Simple. *Phys. Rev. Lett.* **1997**, *78*, 1396.

(18) Blochl, P. E. Projector Augmented-Wave Method. *Phys. Rev. B* **1993**, *50*, 17953–17979.

(19) Jain, A.; Hautier, G.; Moore, C. J.; Ping Ong, S.; Fischer, C. C.; Mueller, T.; Persson, K. A.; Ceder, G. A High-Throughput Infrastructure for Density Functional Theory Calculations. *Comput. Mater. Sci.* **2011**, *50*, 2295–2310.

(20) Grimme, S.; Antony, J.; Ehrlich, S.; Krieg, H. A Consistent and Accurate Ab Initio Parametrization of Density Functional Dispersion Correction (DFT-D) for the 94 Elements H-Pu. *J. Chem. Phys.* **2010**, *132*, 154104.

(21) Mills, G.; Jdnsson, H.; Schenter, G. K. Reversible Work Transition State Theory : Application to Dissociative Adsorption of Hydrogen. *Surf. Sci.* **1995**, *50*, 305–337.

(22) Ulitsky, a.; Elber, R. A New Technique to Calculate Steepest Descent Paths in Flexible Polyatomic Systems. *J. Chem. Phys.* **1990**, *92*, 1510–1511.

(23) Henkelman, G.; Uberuaga, B. P.; Jónsson, H. Climbing Image Nudged Elastic Band Method for Finding Saddle Points and Minimum Energy Paths. *J. Chem. Phys.* **2000**, *113*, 9901–9904.

(24) Bare, S. R.; Kelly, S.; Sinkler, W.; Low, J.; Valencia, S.; Corma, A.; Nemeth, L.; Modica, F. Uniform Catalytic Site in Sn-SS-Zeolite Determined Using X-Ray Absorption Fine Structur. *J. Am. Chem. Soc.* **2005**, *127*, 12924–12932.

(25) Montejo-Valencia, B. D.; Salcedo-Pérez, J. L.; Curet-Arana, M. C. DFT Study of Closed and Open Sites of BEA, FAU, MFI, and BEC Zeolites Substituted with Tin and Titanium. *J. Phys. Chem. C* **2016**, *120*, 2176–2186.

(26) Yang, G.; Pidko, E. A.; Hensen, E. J. M. Structure, Stability, and Lewis Acidity of Mono and Double Ti, Zr, and Sn Framework Substitutions in BEA Zeolites: A Periodic Density Functional Theory Study. *J. Phys. Chem. C* **2013**, *117*, 3976–3986.

(27) Montejo-Valencia, B. D.; Curet-Arana, M. C. DFT Study of the Lewis Acidities and Relative Hydrothermal Stabilities of Bec and Bea Zeolites Substituted with Ti, Sn, and Ge. *J. Phys. Chem. C* **2015**, *119*, 4148–4157.

(28) Yang, G.; Zhu, C.; Zhou, L. Adsorption of Glucose within M(IV)-Incorporated Zeolites: Insights from Periodic Density Functional Theory Calculations. *ChemistrySelect* **2016**, *1*, 6834–6840.

(29) Roman-Leshkov, Y.; Davis, M. E. Activation of Carbonyl-Containing Molecules with Solid Lewis Acids in Aqueous Media. *ACS Catal.* **2011**, *1*, 1566–1580.

(30) Yang, G.; Li, X.; Zhou, L. Adsorption of Fructose in Sn-BEA Zeolite from Periodic Density Functional Calculations. *RSC Adv.* **2016**, *6*, 8838–8847.

5 CHAPTER - DFT STUDY TO UNRAVEL THE CATALYTIC PROPERTIES OF M-EXCHANGED MFI, (M = BE, CO, CU, MG, MN, ZN) FOR THE CONVERSION OF METHANE AND CARBON DIOXIDE TO ACETIC ACID.

5.1 INTRODUCTION

Shale gas, which is predominantly composed of methane (CH_4), is one of the main sources of natural gas in the USA. It is, thus, expected that methane will be the primary source of commodity hydrocarbons in the future[1] and its demand will likely increase from 5 trillion cubic feet (TCF) in 2010 to 13.6 TCF in 2035.[2] CH_4 activation and its conversion to higher value chemicals, however, is still a major challenge. In general, the poor conversion that is usually obtained in CH_4 activation is a consequence of the high C-H bond energy (104 kcal/mol).[3,4] Furthermore, it is also difficult to achieve high selectivity towards a desired product due to the high reactivity of the CH_3 radical. Several review articles have compiled strategies used to activate CH_4 and have outlined the current challenges to develop efficient catalysts for these systems.[5,6] However, most of the experimental[7–15] and computational[16–19] studies have focused on the production of methanol, paying little attention to other products, such as acetic acid. Acetic acid has a market value of $19,560 million, and it is expected to have a market demand of 16,300 kilotons in 2018.[6] As shown in Equation 5-1, acetic acid can be formed from the direct conversion of CH_4 with CO_2:

$$CH_4 + CO_2 \rightarrow CH_3COOH \qquad (5\text{-}1)$$

However, the reaction is thermodynamically unfavorable (ΔG=16.98 kcal/mol) and even under extreme conditions (1000 K, 100 atm with a flow of 95% CO_2 and 5% of CH_4), the thermodynamic equilibrium conversion of CH_4 is 1.6×10^{-6}.[20] Despite these thermodynamic limitations, efforts have been put forth to optimize catalytic systems for this reaction. For example, the reaction has been

carried out successfully with homogeneous catalysts, such as $NaNO_3$–pyrazine-2-carboxylic acid[21] and $Pd(OAc)_2/Cu(OAc)_2/O2/CF_3$.[22] However, the separation process with homogeneous catalysts make these systems not feasible. With heterogeneous catalysts, acetic acid has been produced at high temperatures (>700 K) using metals surfaces,[23–26] or at low temperatures (i.e., 480 K) with metal exchanged zeolites.[27–31] Cu/Co metal oxide,[23] V_2O_5-$PdCl_2/Al_2O_3$,[24] Rh/SiO_2, Pd/SiO_2,[25] and Pt/Al_2O_3[26] are among the metal catalysts that have been employed for the conversion of CH_4 and CO_2 into acetic acid. All these metal oxides require high temperature (>700 K), and their yields are very low, achieving 38 $\mu mol \cdot g^{-1}_{cat} \cdot h^{-1}$ of acetic acid. Cu-MFI and Cu-MOR, on the other hand, have been used to convert CH_4, CO, and H_2O into acetic acid under moderate temperatures (473 K), but with low yields, (22 $\mu mol \cdot g^{-1}_{cat}$ of acetic acid in 0.5 h).[27] Wu and coworkers, however, reported high selectivities on the direct catalytic conversion of CH_4 and CO_2 into acetic acid using Zn-MFI at a moderate temperature of 523K, but low conversions were obtained.[28] It is important to note that all these previous studies have used other reactants, such as CO, H_2, H_2O, or O_2 besides CO_2 and CH_4 in order to overcome the thermodynamic limitations of this reaction. Despite these efforts, however, to our knowledge, no efficient catalyst has been reported yet for the conversion of CH_4 and CO_2 into acetic acid.

Previous density functional theory (DFT) studies have analyzed the activation of CH_4 on different catalysts, as well as the reaction to produce acetic acid or methanol. Periodic DFT calculations have been applied to analyze the metal exchanged zeolites (Zn-FER[32], Cu-MOR[16], Cu-MFI[8]) and metal surfaces (Zn-doped ceria surface[33]). Cluster models have been also used to analyze MFI exchanged zeolites with Au Mg, and Zn.[34–36] For instance, Panjan and coworkers proposed a mechanism for the conversion of CH_4 and CO_2 into acetic acid using Au-MFI.[34] They proposed that CH_4 activation occurs through two steps, both with low activation energies. However,

the following CO_2 insertion was found to be unfavorable (E_{TS} = 66.4 kcal/mol). Zhao and coworkers proposed a similar mechanism using Zn-doped ceria surface as a catalyst, obtaining low energies for CH_4 activation and CO_2 insertion.[33] The final step of the mechanism, which involves the hydrogen transfer from the zeolite to the acetate specie, was found to be unfavorable (E_{TS} = 61.8 kcal/mol).

While most of those studies have made significant contributions to the understanding of the direct conversion of CH_4 and CO_2 into acetic acid, they all have focused on a specific catalyst. A systematic analysis of the effect of the metal cations within the zeolite is still lacking in the literature. In this study, we systematically analyzed and compared the catalytic properties of MFI zeolite exchanged with Be, Co, Cu, Mg, Mn, and Zn. For each stable intermediate and transition state along the reaction mechanism, we obtained several electronic properties to rationalize the differences obtained in the energies of the reaction mechanisms.

5.2 METHODOLOGY

The coordinates used to generate the MFI cluster were obtained from the International Zeolite Association (IZA).[37] The cluster model was obtained by cutting the periodic structure, as shown in Figure 5-1. The boundary Si atoms were saturated with hydrogen atoms, which were aligned in the same direction of the oxygen atoms that were removed. The Si−H bonds were maintained at 1.5000 Å. The site for metal exchange was analyzed within the six-member ring located at the surface of the straight channel, which is composed of two fused five-member rings.[38] This substitution site is called alpha on the basis of the nomenclature proposed by Wichterlova and coworkers.[39] Two Al atoms were substituted in the T2 and T5 positions. To compensate the charge induced by the Al atoms, a +2 charge metal (Be, Co, Cu, Mg, Mn, or Zn) was added to the zeolite.

All the results were obtained using the functional ωB97XD,[40] which is a long-range corrected functional, while the Pople basis set 6- 31+g** was used for all the atoms. The geometry optimizations were performed by optimizing all the atoms, except for the terminal hydrogen atoms that were kept fixed. For the DFT clusters, the partial atomic charges were obtained with the natural bond orbital (NBO) population analysis.[41] All the transition states were corroborated by displaying only one imaginary frequency along the reaction coordinate. Transition states were also verified with intrinsic reaction coordinate (IRC) calculations,[42,43] and all the paths are included in the Appendix D.

The reaction energies of the metal exchanged zeolites were calculated with ONIOM[44] to incorporate the effect of the surrounding zeolitic framework. ONIOM is a combined quantum mechanics / molecular mechanics (QM/MM) method, in which two layers are linked via mechanical embedding. The functional ωB97XD with the basis set 6-31+g** was used for all the atoms in the QM layer, while UFF[45] was used for the MM layer. The section of the zeolite where the reactions occur, composed of 49 atoms, was treated with QM, and the extended zeolite section, composed of 467 atoms, was treated with UFF. This approach has been found appropriate to describe reactions in zeolites.[46–49] Figure 5-2 shows the ONIOM cluster of M−MFI. The geometry optimizations of stable species obtained with ONIOM and DFT were verified with frequency calculations within the rigid-rotor, harmonic-oscillator approximation. Statistical mechanics was used to calculate the vibrational, translational, rotational, and electronic contributions to the partitions functions and the zero-point energy (ZPE) corrections. NBO analysis was performed on stable intermediates and transition states to calculate partial atomic charges. All the energies reported herein have the ZPE corrections. All calculations were carried out with Gaussian 09 Rev B.[50]

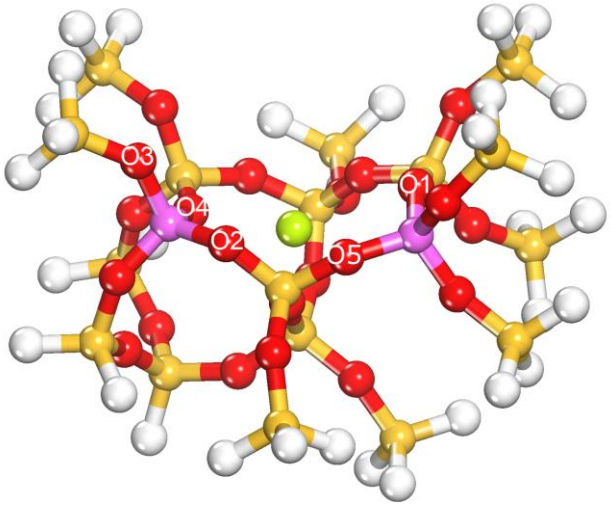

Figure 5-1. 74 atoms cluster used for the DFT calculations of M−MFI. Color legend: yellow = Si; red = O; white = H; pink = Al; green = metal atom (M = Be, Co, Cu, Mg, Mn, Zn).

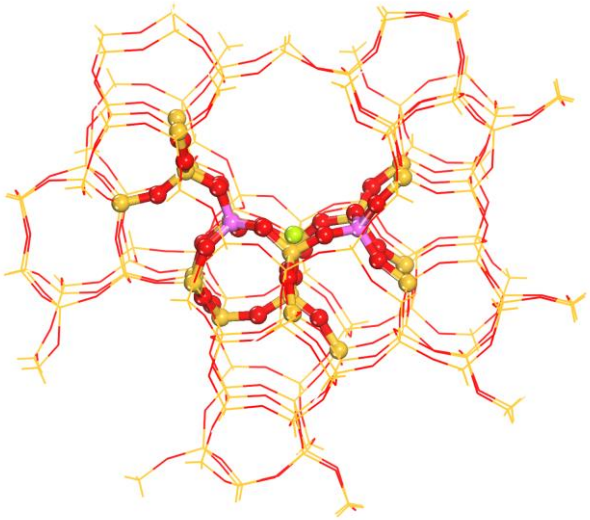

Figure 5-2. M−MFI cluster (49-DFT atoms, 467-MM atoms). The atoms treated with DFT and the atoms treated with MM are shown with the ball and stick and with the wireframe representations, respectively.

5.3 RESULTS AND DISCUSSION

The direct conversion of CH_4 and CO_2 requires three main steps. These include: (i) the dissociation of CH_4, (ii) the insertion of CO_2 into M-CH_3, and iii) the protonation of the acetate species. In the following sections, we aim to obtain a deeper understanding of the activation of

CH_4 and insertion of CO_2 over Be, Cu, Co, Mg, Mn, and Zn exchanged in MFI to elucidate the effect of the metals and the zeolite on the reaction mechanism. First, the lowest spin states of the metal-exchanged zeolites (M =Be, Cu, Co, Mg, Mn, and Zn) are presented followed by the analysis of the adsorption of CH_4 and its activation. The insertion of CO_2 into the M-CH_3 radicals, followed by the acetate protonation are then discussed. In the last section, the effects of the long-range interactions in the reaction energies are analyzed.

5.3.1 Spin states and CH_4 activation on metal exchanged MFI

The reaction mechanism for the conversion of CH_4 and CO_2 into acetic acid over the metal exchanged zeolites was analyzed on the lowest energy spin state of each zeolite. Figure 5-3 shows the relative energies for the three lowest spin states on M-MFI, where the zero energy is assigned to the ground state of each zeolite. For Be-, Mg-, and Zn-MFI zeolites, Ma, Mb, and Mc correspond to the singlet, triplet, and quintet spin states, respectively. For Co-, Cu-, and Mn-MFI zeolites, Ma, Mb, and Mc correspond to the doublet, quartet, and sextet spin states, respectively. As shown in Figure 5-3, the singlet spin state is the lowest energy state for Be-, Mg-, and Zn-MFI zeolites. Doublet, quartet, and sextet spin states are the lowest energy states for Cu-, Co-, and Mn-MFI zeolites, respectively. These results are in good agreement with the experimental ground states obtained with electron paramagnetic resonance spectroscopy for the high spin systems of Mn, Co, and Cu -MFI.[51,52] Thus, all the following geometry optimizations and TS calculations were performed on the ground state of each M-MFI zeolite, as depicted in Figure 5-3.

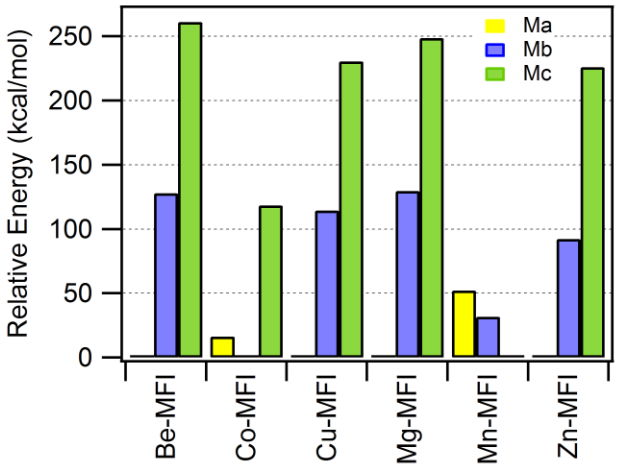

Figure 5-3. Relative energies between spin states for M-MFI. Ma, Mb, and Mc correspond to low, middle, and high spin states, respectively.

Figure 5-4 shows the complete reaction mechanism for the conversion of acetic acid from CO_2 and CH_4. All the energies have the ZPE corrections and were calculated using the DFT cluster shown in Figure 5-1. The first step of the reaction mechanism is the adsorption of CH_4 on the M-MFI zeolite. On the basis of Figure 5-4, CH_4 adsorption energies range from -9.72 kcal/mol for Mg-MFI to -4.59 kcal/mol for Be-MFI. Our results also demonstrate that when CH_4 interacts with the zeolite, the C-H stretching frequency changes, exhibiting a negative shift when interacting with the zeolite. Figure 5-5 shows the relation between CH_4 adsorption energies with the symmetric stretching of the C-H frequency shifts. These results indicate that as the frequency shifts are more negative, the adsorption energies increase. These results are in agreement with the experimental study of Itadani and coworkers, which obtained the same trend with the adsorption of CH_4 on Cu exchanged MFI, MOR, BEA, and USY zeolites.[53] Furthermore, our calculated C-H symmetric stretching frequency of 3027 cm^{-1} is in good agreement with the experimental value of 2885 cm^{-1} with an error of 5%.[53] The predicted negative shift obtained here, -29 cm^{-1}, is identical to the one obtained experimentally (-29.2 cm^{-1}).[53] Thus, on the basis of these results, our calculations accurately describe the interactions of CH_4 with the active sites of the zeolites analyzed herein.

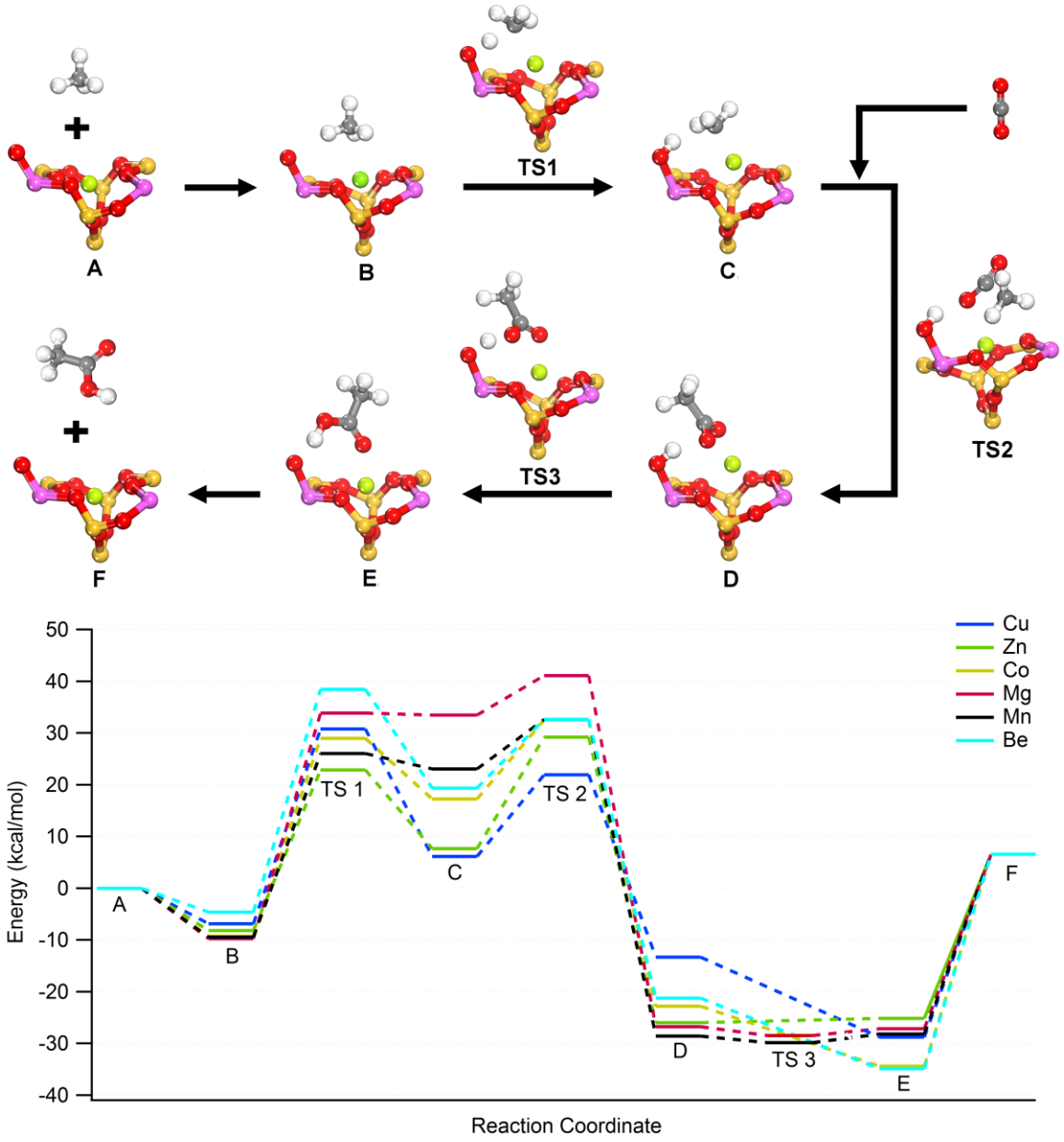

Figure 5-4. Proposed reaction mechanism for the formation of acetic acid from CO_2 and CH_4 (top) and the minimum energy path for the formation of acetic acid on M-MFI (bottom). Atoms beyond the alpha ring were removed on the figures for clarity.

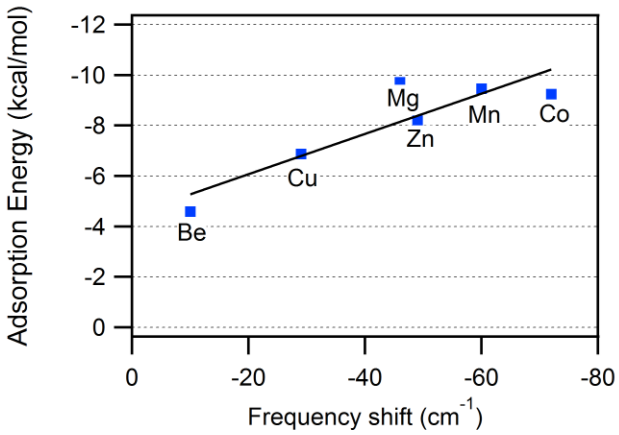

Figure 5-5. CH_4 adsorption energies as function of C-H frequency shifts.

As illustrated with reaction intermediate **C** in Figure 5-4, the detachment of a hydrogen atom from the CH_4 molecule follows methane adsorption. When dissociation of CH_4 occurs, an -OH Brønsted acid site is formed on the ring where CH_3 is coordinated to the metal. The -OH Brønsted acid site can be formed on different oxygen atoms within the ring shown in Figure 5-1. Furthermore, the location of the -OH site yields different reaction energies for the CH_4 dissociation step. Figure 5-6 compares the CH_4 dissociation energies obtained with the different locations of the -OH Brønsted sites on the alpha ring. We note that not all the -OH Brønsted sites yield a stable intermediate **C**, and those sites are not included in Figure 5-6. The lowest CH_4 dissociation energies for Co-MFI, Cu-MFI, Mg-MFI, Mn-MFI, and Zn-MFI were obtained when the -OH Brønsted acid site is located on the O3 oxygen, while for Be-MFI it is on the O2 oxygen. However, CH_4 dissociation energies obtained on Be-MFI –O1 (22.0 kcal/mol), O2 (21.4 kcal/mol), and O3 (23.9 kcal/mol)– are similar, indicating that CH_4 dissociation on Be-MFI can yield an -OH Brønsted site at any of the oxygen atoms on that ring. Therefore, for all the zeolites, we analyzed the rest of the reaction mechanisms from intermediate **C** with the -OH Brønsted acid site located in O3.

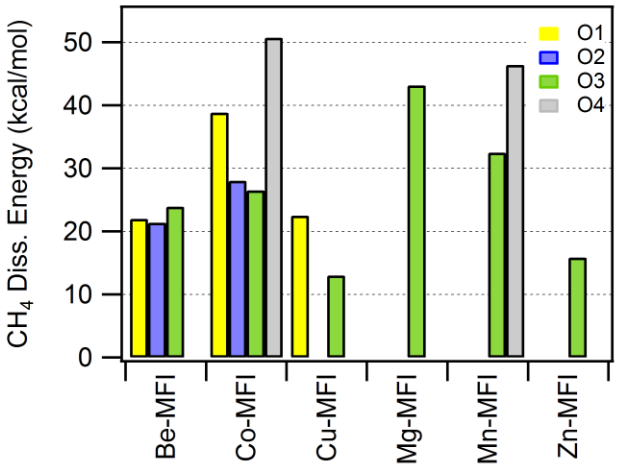

Figure 5-6. Effect of the location of the OH Brønsted acid site on CH_4 dissociation energies on the alpha ring of M-MFI. The location of O1, O2, O3, and O4 within the ring are illustrated in Figure 5-1.

The O-H bond formed upon CH_4 dissociation has the same length of 0.96 Å on all the zeolites, while the length of the M-C bond varies significantly from 1.7 Å for Be-MFI to 2.13 Å for Mg-MFI. The three C-H bonds of the CH_3 remain between 1.09 and 1.10 Å, close to the CH_4 gas phase value of 1.09 Å. Experimentally, the OH and the C-H stretching bands of CH_4 dissociated on Zn-MFI appear at 3610 cm^{-1} and 2890 cm^{-1}, respectively.[54] On the other hand, X-ray adsorption analysis of dimethyl zinc shows that the Zn-C bond length is 1.93 Å.[55,56] Our calculated OH (3725 cm^{-1}), and C-H (3028 cm^{-1}) bands, as well as our calculated Zn-C (1.96 Å) bond length, are in good agreement with those experimental results.

The methane dissociation step is endothermic on all the zeolites that were analyzed, and the energy on that step ranges from 13.0 kcal/mol for Cu-MFI to 43.2 kcal/mol for Mg-MFI. Table D-1 and Table D-2 in the Appendix D show how the NBO charges of the metal and the carbon atoms change through this step. In all zeolites, the C atom becomes more negative upon CH_4 dissociation when compared against the isolated or adsorbed CH_4. On the other hand, the metal atom becomes less positive upon CH_4 dissociation, indicating that the reaction involves a charge transfer from CH_4 to the metal atom. Thus, this reaction can be described as an electron donation reaction, in

which electron density is transferred from CH_4-σ-(C-H) to the metal unoccupied orbital. This electron density transfer is also reflected in the electronic occupancy of the metal atoms as the electron density of the metal increases during CH_4 dissociation. For example, the 4s, 3d, and 4p orbitals of Cu-MFI, which has the lowest dissociation energy, increase their electron occupancy through CH_4 dissociation, as shown in Table 5-1.

Table 5-1 Cu electron occupancy along the dissociation step. A, B and C are illustrated in Figure 5-4.

Cu in **A**	[core]4s(0.23)3d(9.24)4p(0.26)5p(0.01)
Cu in **B**	[core]4s(0.22)3d(9.24)4p(0.34)
Cu in **C**	[core]4s(0.27)3d(9.53)4p(0.31)

The transition state (TS) of CH_4 dissociation is highly endothermic, as shown in Figure 5-4. The TS energies increase as follows: Zn-MFI (31.1 kcal/mol) < Mn-MFI (35.5 kcal/mol) < Cu-MFI (37.6 kcal/mol) < Co-MFI (38.2 kcal/mol) < Be-MFI (43.1 kcal/mol) < Mg-MFI (43.6 kcal/mol). Our results also indicate that the energy of the TS can be related to the energy of the lowest unoccupied molecular orbital (LUMO) of the isolated zeolite. Figure 5-7a shows that as the LUMO energy decreases, the TS energy decreases, suggesting that a lower LUMO energy on a metal-exchanged zeolite facilitates the electronic donation from CH_4 to the zeolite. The results in Figure 5-7b also indicate that there is an inverse relationship between the TS energies and the electronegativities (X) of the isolated zeolites. X was calculated with the negative average value between the HOMO and the LUMO energies.[57] Thus, as shown in Figure 5-7b, as X increases the energy of the TS decreases, suggesting that it is easier for the zeolite to attract the electron density from CH_4.

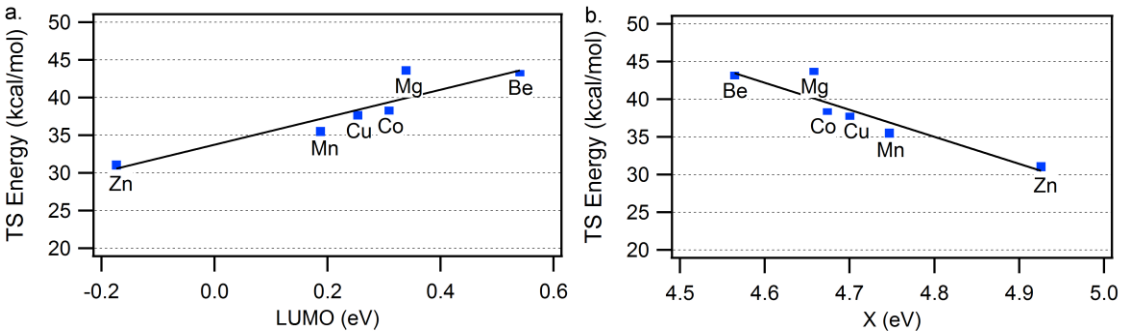

Figure 5-7 Relationship between the TS of the CH_4 dissociation with the (a) LUMO energies and (b) electronegativity, X, of the metal exchanged MFI zeolites.

Figure 5-8 and

Table 5-2 describe the TS geometry obtained for the metal exchanged MFI zeolites. For instance, the distance between the donated hydrogen (H1) and the carbon atom (C1), C1-H1, is elongated from 1.09 Å, which corresponds to C-H bond on CH4, to 1.41-1.70 Å. The distance between the metal atom (M) and the C1 atom is shortened to 1.83-2.21 Å depending on the metal. This TS also involves the formation of the Brønsted acid site, as the distance between the oxygen atom (O3) and the donated hydrogen, (O3-H1) shortens to 1.09-1.30 Å.

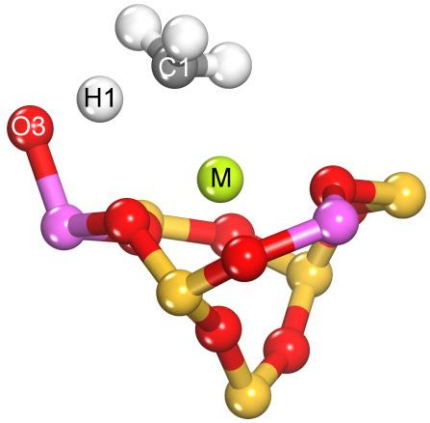

Figure 5-8. Transition state of the dissociation of CH_4. Atoms beyond the alpha ring were removed on this figure for clarity. M = Be, Co, Cu, Mg, Mn, Zn

Table 5-2 Geometric parameters of the TS's for the dissociation of CH_4. d_{ij} is the distance between atoms i and j. The legend of the atom number is shown in Figure 5-8.

	$d_{O3\text{-}H1}$ (Å)	$d_{C1\text{-}H1}$ (Å)	$d_{M\text{-}C1}$ (Å)
Be-MFI	1.25	1.49	1.83
Co-MFI	1.19	1.52	2.12
Cu-MFI	1.30	1.41	2.10
Mg-MFI	1.09	1.70	2.21
Mn-MFI	1.13	1.59	2.21
Zn-MFI	1.24	1.47	2.10

5.3.2 Insertion of CO_2 into the M-CH_3 radicals and acetate protonation

The reaction of **C** to stable intermediate **D** shown in Figure 5-4 illustrates the CO_2 insertion onto the M-CH_3 complex. In this reaction mechanism, the CO_2 insertion occurs following an Eley-Rideal mechanism.[58] The intermediate **D** is formed through the insertion of CO_2 into de M-C bond yielding an acetate species. This acetate intermediate, **D**, is adsorbed on the zeolite as a bidentate pincer, coordinating both oxygens to the metal atom (e.g., on Cu-MFI, the distances between the Cu atom and the acetate oxygens are 1.97 Å and 2.03 Å). The CO_2 insertion step is highly

exothermic in all the zeolites, and it ranges from -19.5 kcal/mol for Cu-MFI to -60.2 kcal/mol for Mg-MFI. These strong interactions are related to a very stable acetate intermediate.

The CO_2 insertion into M-CH_3 has been conducted experimentally in several studies.[59,60] For instance, Johansson and coworkers used 30 equiv. of CO_2 in a reaction with $PCP^{(tBu)}$Pd-CH_3 to obtain $PCP^{(tBu)}$Pd-OAc.[59] In another study, the insertion of CO_2 in (PCP)Ni-CH_3 resulted in a step with a high TS energy of 30.3 kcal/mol.[60] Thus, in general, the CO_2 insertion is a slow process even in homogeneous catalysis. On the other hand, a recent theoretical study obtained low energy barriers for CO_2 insertion in Zn-doped ceria surface (11.8 kcal/mol).[33] The catalysts analyzed in this work exhibit similar TS energies. The TS energies of CO_2 insertion (TS2) increase as follows: Mg-MFI (7.6 kcal/mol) < Mn-MFI (9.6 kcal/mol) < Be-MFI (13.3 kcal/mol) < Co-MFI (15.3 kcal/mol) < Cu-MFI (15.8 kcal/mol) < Zn-MFI (21.6 kcal/mol).

CO_2 has a highly oxidized carbon and its insertion into the M-C bond is through a nucleophilic attack. Figure 5-9 and Table 5-3 describe the transition states obtained for the metal exchanged MFI zeolites. Table 5-3 shows the CO_2 angle, the distance between the CH_3 carbon (C1) and the CO_2 carbon (C2), as well as the distance between the oxygen of the CO_2 (O6) and the hydrogen of the Brønsted site (H1). In TS2, CO_2 activation is evident, as it is bent and the C-O bonds are elongated. Thus, as shown in Table 5-3, CO_2 changes its 180° angle in the gas phase to an angle that ranges between 146.6° to 158.5° depending on the metal. In general, the TS energies obtained for all the zeolites are low, due to the synergistic interactions between the atoms. These interactions are reflected in the short distances found between the atoms O6-H1, M-C1, M-C2, and C1-C2, allowing a low activation energy for the insertion of the CO_2 into the M-CH_3.

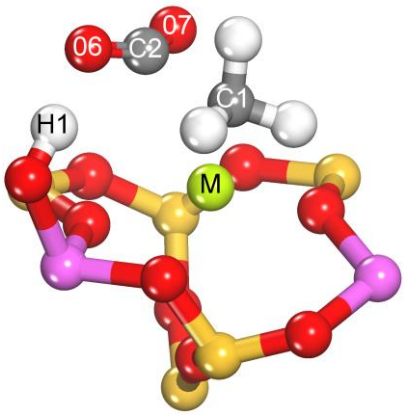

Figure 5-9. Transition state of CO_2 insertion, TS2. Atoms beyond the alpha ring were removed on this figure for clarity. M = Be, Co, Cu, Mg, Mn, Zn.

Table 5-3. Geometric parameters for the transition state of CO_2 insertion, TS2. d_{ij} is the distance between atoms i and j and $\theta_{i\text{-}j\text{-}k}$ is the angle between atoms i, j, and k. The legend of the atom number is shown in Figure 5-9.

	$\theta_{O6\text{-}C2\text{-}O7}$ (°)	$d_{C1\text{-}C2}$ (Å)	$d_{O6\text{-}H1}$ (Å)	$d_{M\text{-}C1}$ (Å)	$d_{M\text{-}C2}$ (Å)
Be-MFI	158.5	2.30	3.22	1.80	2.18
Co-MFI	150.8	2.18	1.64	2.05	2.47
Cu-MFI	153.9	2.11	1.88	3.79	3.14
Mg-MFI	157.0	2.33	1.71	2.18	2.92
Mn-MFI	155.3	2.30	1.75	2.16	2.68
Zn-MFI	146.6	2.08	1.53	2.08	2.55

As opposed to the regular CO_2 insertion through the four- centered transition state, in which the O-M and C-C bonds are formed while the M-C bond breaks,[61] here the CO_2 insertion occurs through a S_E2 mechanism, in which the M-C bond is not broken. The S_E2 mechanism in CO_2 insertion was also observed in Pd-CH_3,[62] Ni-CH_3,[60] and Zn doped ceria surface.[33] The C1 charge varies from -0.55 to -1.36, and the C2 charge varies from 0.95 to 1.06, reflecting the high electron density of the M-CH_3 species and the highly oxidized carbon on the inserted CO_2.

The protonation of acetate to produce acetic acid is shown in the reaction from intermediate **D** to **E** in Figure 5-4. The protonation energies range from 0.83 kcal/mol for Zn-MFI to -15.4 kcal/mol for Cu-MFI. This reaction is spontaneous, and the energies of the protonation transition states found are -1.72 kcal/mol and -1.29 kcal/mol for Mg-MFI and Mn-MFI, respectively. These

negative values are due to the error introduced by the approximations taken in the frequency calculations. The TS energies values obtained without the ZPE correction were 0.35 kcal/mol and 0.68 kcal/mol for Mg-MFI and Mn-MFI, respectively. Table 5-4 and Figure 5-10 describe the geometry of the TS. The donated hydrogen (H1) is between oxygens O3 and O6, while the metal atom interacts with both oxygens of the acetate, O6, and O7. The transition states found have only one imaginary frequency, which corresponds to the movement of the H1 hydrogen between the O3 and O6 oxygens. Due to the highly favorable protonation energies, the TS's for the other metals could not be obtained. The almost zero TS's energies obtained for Mg-MFI and Mn-MFI were extrapolated to the others metals. Thus, the adsorbed acetic acid is more stable than the acetate intermediate, and its protonation step is spontaneous for all the zeolites. These MFI catalysts can transform the acetate into acetic acid easily, in contrast to other proposed catalysts, such as Zn doped ceria, which has a high TS energy of 61.8 kcal/mol.[33]

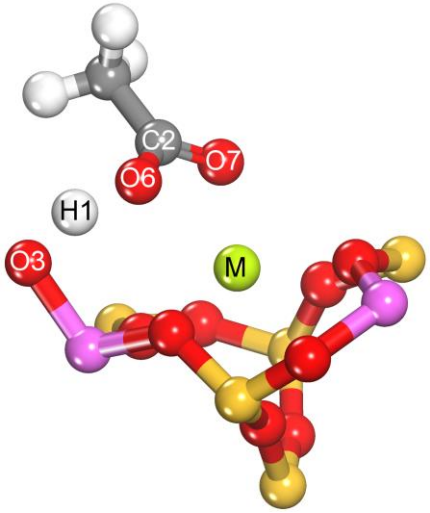

Figure 5-10. Transition state of the acetate protonation. M = Mg or Mn.

Table 5-4. Geometric parameters for the acetate protonation. The legend of the atom number is shown in Figure 5-10.

	$d_{O3\text{-}H1}$ (Å)	$d_{H1\text{-}O6}$ (Å)	$d_{M\text{-}O6}$ (Å)	$d_{M\text{-}O7}$ (Å)
Mg-MFI	1.18	1.22	2.30	2.12
Mn-MFI	1.21	1.18	2.34	2.2

The last step of the reaction mechanism is the acetic acid desorption, which is highly unfavorable. Desorption energies range from 31.7 kcal/mol for Zn-MFI to 41.5 kcal/mol for Be-MFI. In the following section, we discuss the possibility of desorbing the acetic acid with water in order to overcome the strong interaction of acetic acid with the zeolite and, thus, make the reaction more thermodynamically favorable.

5.3.3 Effect of the long-range interactions in the reaction energies

The effect of the zeolite confinement on these systems was studied by calculating reaction energies using the ONIOM cluster shown in Figure 5-2. Figure 5-11 shows CH_4 adsorption energies and CH_4 dissociation energies. The long-range dispersion contributions to the CH_4 adsorption energies (solid blue) were isolated from the rest of the contributions (lines pattern), which include the DFT energy and the bending, torsion and stretching contributions from the molecular mechanic's layer of the ONIOM cluster.

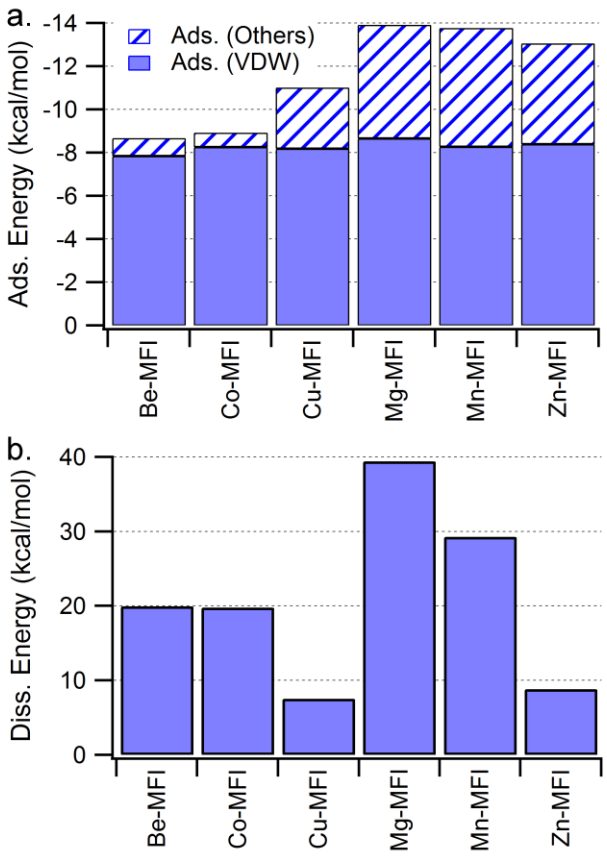

Figure 5-11. (a) CH_4 adsorption and (b) dissociation energies calculated with ONIOM.

The adsorption energies obtained with the ONIOM cluster are lower than the energies obtained with the DFT clusters. In all the systems, dispersion contributions account for more than 60% of the total adsorption energies and are roughly constant regardless of the metal cation in the zeolite. The dispersion effects on Be-MFI and Co-MFI, in particular, account for more than 90% of the adsorption energies. As shown in Figure 5-11a, the metal cation within the zeolite has an impact on the adsorption energies, and this is reflected in the quantum mechanical contributions to the adsorption energies, which are outlined in Table D-3 of the Appendix D. In general, the adsorption of CH_4 is feasible in all the zeolites analyzed due to the dispersion energies manifested when CH_4 interacts with the tight pore of the MFI zeolite.

CH_4 dissociation energies on these systems ranged from 7.6 kcal/mol for Cu-MFI to 39.4 kcal/mol for Mg-MFI. The energies for CH_4 dissociation with ONIOM are lower than those

obtained with the DFT cluster, but the energy trends calculated with both methods are similar. The energy contributions to CH_4 dissociation energies are listed in Table D-4 in the Appendix D. The dispersion contributions to the CH_4 dissociation energies are almost negligible (<0.5 kcal/mol). On the other hand, some other contributions that are captured from the molecular mechanics part, such as the stretching, bending, and torsion affect to a greater extent the dissociation energies.

Based on the dissociation energies obtained for Cu-MFI (7.6 kcal/mol) and Zn-MFI (8.9 kcal/mol), which are lower than those obtained with the other materials (>19.7 kcal/mol), CH_4 activation is more favorable on Cu-MFI and Zn-MFI than on Be, Mg, Mn, or Co-MFI. Thus, we calculated the transition states of methane dissociation with the ONIOM cluster for Cu-MFI and Zn-MFI. The TS energies obtained are 22.5 kcal/mol and 28.7 kcal/mol for Cu-MFI and Zn-MFI, respectively. These values are lower than those obtained with the DFT cluster. The contributions to the calculated TS energies are shown in Table D- 5 in the Appendix D. The contribution of dispersion forces to the TS energies are low, while contributions such as stretching, bending, and torsion have a greater impact on the TS energies. Furthermore, TS geometries obtained with ONIOM differ from those obtained with the DFT cluster. On the TS geometry obtained with ONIOM, the metal atom is coordinated to O2 and O5 oxygens of the alpha ring, while in the DFT cluster, the metal is coordinated to O4 and O2. The distances between the metal and the coordinated oxygens, as well as the distance between the metal atom and the carbon atom decrease when compared to the DFT results. These changes on the TS geometries impact the charge of the metal atom, which in general are more positive in the ONIOM calculation than in the DFT results. The geometric parameters and the charges of the atoms are shown in Table D- 6 and Table D- 7 in the Appendix D for Cu-MFI and Zn-MFI, respectively. The differences in the TS energies obtained

between methods could be related to the static dipole moments caused by the pore confinement that is reflected in the change of the metal charge, as suggested by Göltl and coworkers.[17]

Based on the mechanisms obtained with the DFT cluster, the CH_4 dissociation is the step with highest energy barrier in the conversion of CH_4 and CO_2 into acetic acid. ONIOM calculations suggest that Cu-MFI is the zeolite which requires less energy to dissociate CH_4 with an apparent activation energy of 11.5 kcal/mol. Based on the above, we calculated the rest of the stable intermediates for Cu-MFI using the ONIOM cluster. The complete reaction mechanism for Cu-MFI is shown in Figure 5-12, in which the geometry optimizations are shown for each step of the reaction mechanism.

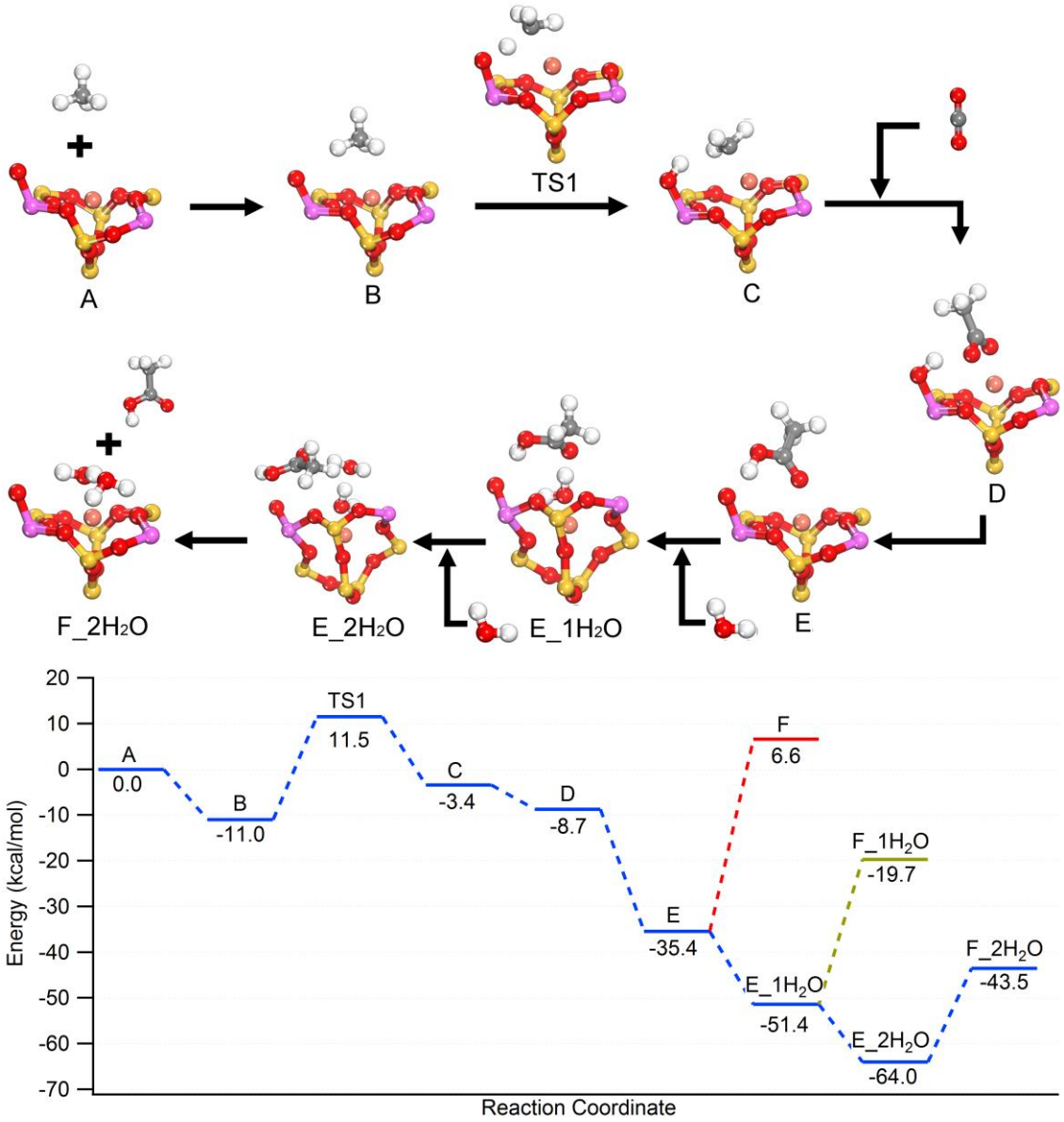

Figure 5-12. Reaction mechanism for the conversion of CH_4 and CO_2 into acetic acid on Cu-MFI (top) and the energy path for the reaction on Cu-MFI obtained with ONIOM (bottom). The last two steps in the reaction mechanism correspond to desorption of acetic acid with one or two water molecules in the system.

We note that the insertion of CO_2 into Cu-CH_3 complex and the protonation of acetate are exothermic with energies of -5.3 kcal/mol and -26.7 kcal/mol. The adsorbed acetic acid has a strong interaction with the zeolite, which is reflected in its high desorption energy of 42 kcal/mol. The adsorption of water molecules on intermediate **E** is energetically favorable and reduces the

acetic acid desorption energy to 31.7 kcal/mol with one co-adsorbed water molecule, and to 20.5 kcal/mol with two co-adsorbed water molecules. Thus, acetic acid desorption can be promoted with water and a moderate temperature increase in agreement with experimental[15] and computational[16] results.

The forward rate for CH_4 dissociation can be calculated with the equation 5-2:

$$r_{site}^{forward} = k_{site}^{forward} p_{CH_4} \theta_{site} \quad (5\text{-}2)$$

Here, $k_{site}^{forward}$ is the forward rate constant, p_{CH_4} is the methane partial pressure, and θ_{site} is the number of catalytic sites in which CH_4 can be dissociated. The forward rate constant can be calculated with transition state theory (Equation 5-3):

$$k_{site}^{forward} = \frac{k_B T}{h} e^{\frac{-\Delta G^{\neq}_{site}}{k_B T}} \quad (5\text{-}3)$$

Here, k_B is the Boltzmann constant, h is the Planck constant, and $\Delta G^{\neq}_{site}$ is the Gibbs free energy barrier of the transition state to dissociate the CH_4 at a temperature T. On the basis of our ONIOM results, the Gibbs free energy barrier for CH_4 dissociation at 398 K on Cu-MFI is 23.45 kcal/mol, which gives a forward rate constant ($k_{site}^{forward}$) of 1.1 s^{-1}. This rate constant is higher to that of Cu-MOR active site obtained by Zhao and coworkers, who reported a rate constant value of 0.79 s^{-1} at 398K[16] It is important to highlight that in the catalytic systems analyzed herein, CH_4 activation does not occur through oxygen atoms that are coordinated to the metal, such as the active site analyzed by Zhao and coworkers.[16] In our case, the metal atom promotes CH_4 activation by forming an M-C bond. The advantage of reduced catalytic system is that the active sites of the catalyst require less regeneration, and the product desorption may be more feasible if water is used when compared to oxidized metal sites.

Our results indicate that Cu-MFI and Zn-MFI can convert CO_2 and CH_4 into acetic acid at a moderate temperature. As far as we know, only two experimental studies with Cu- and Zn- MFI have reported the conversion of CH_4 and CO_2 or CO into acetic acid at moderate temperatures.[27,28] Those studies, however, reported low yields. It is important to note that our work has been based on the analysis of acetic acid formation through metals exchanged on the alpha ring of MFI zeolite, while experiments always include a distribution of sites in which the reaction is catalyzed to different extents. Future work should address the impact of the different sites of MFI on the kinetics of acetic acid formation and methane activation.

5.4 CONCLUSIONS

Our results demonstrate that the singlet spin state is the lowest energy state for Be-, Mg-, and Zn-MFI zeolites, while doublet, quartet, and sextet spin states are the lowest energy states for Cu-, Co-, and Mn-MFI zeolites, respectively. Our calculations clearly showed that as the C-H stretching frequency shifts are more negative on adsorbed CH_4, the adsorption energies increase. Upon CH_4 dissociation, the charge of the metal atom decreases when compared to the charge of the metal on the isolated zeolite, indicating that the process is carried out through a charge transfer from the CH_4 to the metal atom. Our results also indicate that as the LUMO energy decreases, the TS energy for CH_4 dissociation decreases. Furthermore, CO_2 insertion occurs though a S_E2 mechanism in which the M-C bond is maintained on the TS. The protonation step to form adsorbed acetic acid is spontaneous on all the zeolites that were analyzed, and this adsorbed species is more stable than gas phase acetic acid. The ONIOM calculations revealed that while dispersion contributions account for more than 60% of the CH_4 adsorption energies, the exchanged metal within the zeolite also impacts the adsorption energies. The CH_4 dissociation step is the reaction with the highest

energy barrier in the conversion of CH_4 and CO_2 into acetic acid, and Cu-MFI is the zeolite which requires less energy to dissociate the CH_4, with an apparent activation energy of 11.5 kcal/mol. Finally, our results also demonstrated that the acetic acid desorption energy can be reduced from 42.0 kcal/mol to 20.5 kcal/mol with the co-adsorption of water molecules.

5.5 REFERENCES

(1) McFarland, E. Unconventional Chemistry for Unconventional Natural Gas. *Science.* **2012**, *338*, 340–342.

(2) Liss, W. Addressing the Challenges Along the Shale Gas Supply Chain. *Chem. Eng. Prog.* **2012**, *108*, 34.

(3) Havran, V.; Duduković, M. P.; Lo, C. S. Conversion of Methane and Carbon Dioxide to Higher Value Products. *Ind. Eng. Chem. Res.* **2011**, *50*, 7089–7100.

(4) Labinger, J. A.; Bercaw, J. E. Understanding and Exploiting C-H Bond Activation. *Nature* **2002**, *417*, 507–514.

(5) Olivos-Suarez, A. I.; Szécsényi, A.; Hensen, E. J. M.; Ruiz-Martinez, J.; Pidko, E. A.; Gascon, J. Strategies for the Direct Catalytic Valorization of Methane Using Heterogeneous Catalysis: Challenges and Opportunities. *ACS Catal.* **2016**, *6*, 2965–2981.

(6) Taifan, W.; Baltrusaitis, J. CH4 Conversion to Value Added Products: Potential, Limitations and Extensions of a Single Step Heterogeneous Catalysis. *"Applied Catal. B, Environ.* **2016**, *198*, 525–547.

(7) Narsimhan, K.; Iyoki, K.; Dinh, K.; Román-Leshkov, Y. Catalytic Oxidation of Methane into Methanol over Copper- Exchanged Zeolites with Oxygen at Low Temperature. *ACS Cent. Sci.* **2016**, *2*, 424–429.

(8) Kulkarni, A. R.; Zhao, Z.; Siahrostami, S.; Nørskov, J. K.; Studt, F. Monocopper Active Site for Partial Methane Oxidation in Cu- Exchanged 8MR Zeolites. *ACS Catal.* **2016**, *6*, 6531–6536.

(9) Alayon, E. M. C.; Nachtegaal, M.; Bodi, A.; Van Bokhoven, J. A. Reaction Conditions of Methane-to-Methanol Conversion Affect the Structure of Active Copper Sites. *ACS Catal.* **2014**, *4*, 16–22.

(10) Grundner, S.; Markovits, M. A. C.; Li, G.; Tromp, M.; Pidko, E. A.; Hensen, E. J. M.; Jentys, A.; Sanchez-Sanchez, M.; Lercher, J. A. Single-Site Trinuclear Copper Oxygen Clusters in Mordenite for Selective Conversion of Methane to Methanol. *Nat. Commun.* **2015**, *6*, 7546.

(11) Tomkins, P.; Mansouri, A.; Bozbag, S. E.; Krumeich, F.; Park, M. B.; Alayon, E. M. C.; Ranocchiari, M.; VanBokhoven, J. A. Isothermal Cyclic Conversion of Methane into Methanol over Copper-Exchanged Zeolite at Low Temperature. *Angew. Chemie - Int. Ed.* **2016**, *55*, 5467–5471.

(12) Woertink, J. S.; Smeets, P. J.; Groothaert, M. H.; Vance, M. a; Sels, B. F.; Schoonheydt, R. a; Solomon, E. I. A $[Cu_2O]^{2+}$ Core in Cu-ZSM-5, the Active Site in the Oxidation of Methane to Methanol. *Proc. Natl. Acad. Sci.* **2009**, *106*, 18908–18913.

(13) Wulfers, M. J.; Lobo, R. F.; Ipek, B.; Teketel, S. Conversion of Methane to Methanol on Copper-Containing Small-Pore Zeolites and Zeotypes. *Chem. Commun.* **2015**, *51*, 4447–4450.

(14) Groothaert, M. H.; Smeets, P. J.; Sels, B. F.; Jacobs, P. A.; Schoonheydt, R. A. Selective Oxidation of Methane by the Bis (M-Oxo) Dicopper Core Stabilized on ZSM-5 and Mordenite Zeolites. *J. Am. Chem. Soc.* **2005**, *127*, 1394–1395.

(15) Vanelderen, P.; Snyder, B. E. R.; Tsai, M.-L.; Hadt, R. G.; Vancauwenbergh, J.; Coussens, O.; Schoonheydt, R. a.; Sels, B. F.; Solomon, E. I. Spectroscopic Definition of the Copper Active Sites in Mordenite : Selective Methane Oxidation. *J. Am. Chem. Soc.* **2015**, *137*, 6383–6392.

(16) Zhao, Z.-J.; Kulkarni, A.; Vilella, L.; Norskov, J. K.; Studt, F. Theoretical Insights into the Selective Oxidation of Methane to Methanol in Copper-Exchanged Mordenite. *ACS Catal.* **2016**, *6*, 3760–3766.

(17) Göltl, F.; Michel, C.; Andrikopoulos, P. C.; Love, A. M.; Hafner, J.; Hermans, I.; Sautet, P. Computationally Exploring Confinement Effects in the Methane-to-Methanol Conversion Over Iron-Oxo Centers in Zeolites. *ACS Catal.* **2016**, *6*, 8404–8409.

(18) Pantu, P.; Pabchanda, S.; Limtrakul, J. Theoretical Investigation of the Selective Oxidation of Methane to Methanol on Nanostructured Fe-ZSM-5 by the ONIOM Method. *ChemPhysChem* **2004**, *5*, 1901–1906.

(19) Mahyuddin, M. H.; Staykov, A.; Shiota, Y.; Yoshizawa, K. Direct Conversion of Methane to Methanol by Metal-Exchanged ZSM-5 Zeolite (Metal = Fe, Co, Ni, and Cu). *ACS Catal.* **2016**, *6*, 8321–8331.

(20) Wilcox, E. M.; Gogate, M. R.; Spivey, J. J.; Roberts, G. W. Direct Synthesis of Acetic Acid from Methane and Carbon Dioxide. In *Studies in Surface Science and Catalysis*; 2001; 136, 259–264.

(21) Nizova, G. V.; Suss-Fink, G.; Stanislas, S.; Shul'pin, G. B. Carboxylation of Methane with CO or CO2 in Aqueous Solution Catalysed by Vanadium Complexes. *Chem. Commun.* **1998**, *1998*, 1885–1886.

(22) Kurioka, M.; Fujiwara, Y.; Taniguchi, Y.; Takaki, K.; Nakata, K.; Jintoku, T. Palladium-Catalyzed Acetic Acid Synthesis from Methane and Carbon Monoxide or Dioxide. *Chemistry Letters*. **1995**, 1995 244.

(23) Huang, W. Possibility of Direct Conversion of CH_4 and CO_2 to High-Value Products. *J. Catal.* **2001**, *201*, 100–104.

(24) Huang, W.; Zhang, C.; Yin, L.; Xie, K. Direct Synthesis of Acetic Acid from CH4 and CO2 in the Presence of O2 over a V2O5-PdCl2/Al2O3 Catalyst. *J. Nat. Gas Chem.* **2004**, *13*, 113–115.

(25) Ding, Y. H.; Huang, W.; Wang, Y. G. Direct Synthesis of Acetic Acid from CH_4 and CO_2 by a Step-Wise Route over Pd/SiO_2 and Rh/SiO_2 Catalysts. *Fuel Process. Technol.* **2007**, *88*, 319–324.

(26) Wilcox, E. M.; Roberts, G. W.; Spivey, J. J. Direct Catalytic Formation of Acetic Acid from CO_2 and Methane. *Catal. Today* **2003**, *88*, 83–90.

(27) Narsimhan, K.; Michaelis, V. K.; Mathies, G.; Gunther, W. R.; Griffin, R. G.; Román-Leshkov, Y. Methane to Acetic Acid over Cu-Exchanged Zeolites: Mechanistic Insights from a Site-Specific Carbonylation Reaction. *J. Am. Chem. Soc.* **2015**, *137*, 1825–1832.

(28) Wu, J.; Yu, S.; Wang, W. D.; Fan, Y.; Bai, S.; Zhang, C.; Gao, Q.; Huang, J.; Wang, W. Mechanistic Insight into the Formation of Acetic Acid from the Direct Conversion of Methane and Carbon Dioxide on Zinc-Modified H−ZSM-5 Zeolite. *J. Am. Chem. Soc.* **2013**, *135*, 13567–13573.

(29) Rabie, A. M.; Betiha, M. A.; Park, S.-E. Direct Synthesis of Acetic Acid by Simultaneous Co-Activation of Methane and CO2 over Cu-Exchanged ZSM-5 Catalysts. *"Applied Catal. B, Environ.* **2017**, *215*, 50–59.

(30) Wang, X.; Qi, G.; Xu, J.; Li, B.; Wang, C.; Deng, F. NMR-Spectroscopic Evidence of Intermediate-Dependent Pathways for Acetic Acid Formation from Methane and Carbon Monoxide over a ZnZSM-5 Zeolite Catalyst. *Angew. Chem. Int. Ed. Engl* **2012**, *51*, 3850–3853.

(31) Wu, J. F.; Wang, W. D.; Xu, J.; Deng, F.; Wang, W. Reactivity of C1 Surface Species Formed in Methane Activation on Zn-Modified H-ZSM-5 Zeolite. *Chem. a Eur. J.* **2010**, *16*, 14016–14025.

(32) Benco, L. Electronic Structure of Zn^+-Modified Zeolite: A Density Functional Theory Study of Ferrierite. *J. Phys. Chem. C* **2016**, *120*, 6031–6038.

(33) Zhao, Y.; Cui, C.; Han, J.; Wang, H.; Zhu, X.; Ge, Q. Direct C−C Coupling of CO2 and the Methyl Group from CH4 Activation through Facile Insertion of CO2 into Zn−CH3 σ-Bond. *J. Am. Chem. Soc.* **2016**, *138*, 10191–10198.

(34) Panjan, W.; Sirijaraensre, J.; Warakulwit, C.; Pantu, P.; Limtrakul, J. The Conversion of CO2 and CH4 to Acetic Acid over the Au-Exchanged ZSM-5 Catalyst : A Density Functional Theory Study. *Phys. Chem. Chem. Phys.* **2012**, *14*, 16588–16594.

(35) Oda, A.; Torigoe, H.; Itadani, A.; Ohkubo, T.; Yumura, T.; Kobayashi, H.; Kuroda, Y. Mechanism of CH4 Activation on a Monomeric Zn2+ -Ion Exchanged in MFI-Type Zeolite with a Specific Al Arrangement: Similarity to the Activation Site for H2. *J. Phys. Chem. C* **2013**, *117*, 19525–19534.

(36) Oda, A.; Torigoe, H.; Itadani, A.; Ohkubo, T.; Yumura, T.; Kobayashi, H.; Kuroda, Y. An Important Factor in CH_4 Activation by Zn Ion in Comparison with Mg Ion in MFI: The Superior Electron-Accepting Nature of Zn^{2+}. *J. Phys. Chem. C* **2014**, *118*, 15234–15241.

(37) International Zeolite Association (IZA). http://europe.iza-structure.org/IZA-SC/ftc_fw.php?STC=MFI (accessed Aug 20, 2016).

(38) Groothaert, M. H.; Pierloot, K.; Delabie, A.; Schoonheydt, R. A. Identification of Cu(II) Coordination Structures in Cu-ZSM-5, Based on a DFT/ab Initio Assignment of the EPR Spectra. *Phys. Chem. Chem. Phys.* **2003**, *5*, 2135–2144.

(39) Dědeček, J.; Kaucký, D.; Wichterlová, B. Co^{2+} Ion Siting in Pentasil-Containing Zeolites, Part 3. Co^{2+} Ion Sites and Their Occupation in ZSM-5: A VIS Diffuse Reflectance Spectroscopy Study. *Microporous Mesoporous Mater.* **2000**, *35–36*, 483–494.

(40) Chai, J.-D.; Head-Gordon, M. Long-Range Corrected Hybrid Density Functionals with Damped Atom-Atom Dispersion Corrections. *Phys. Chem. Chem. Phys.* **2008**, *10*, 6615–6620.

(41) Weinhold, F.; Carpenter, J. *The Structure of Small Molecules and Ions*; Naaman, R., Vager, Z., Eds.; Springer US: (Plenum, New York), 1988.

(42) Hratchian, H. P.; Schlegel, H. B. Theory and Applications of Computational Chemistry: The First 40 Years. In *Theory and Applications of Computational Chemistry: The First 40 Years*; Dykstra, C. E., Frenking, G., Kim, K. S., Scuseria, G. E., Eds.; Elsevier: Amsterdan, 2005; 195–249.

(43) Fukui, K. The Path of Chemical Reactions - the IRC Approach. *Acc. Chem. Res.* **1981**, *14*, 363–368.

(44) Humbel, S.; Sieber, S.; Morokuma, K. The IMOMO Method: Integration of Different Levels of Molecular Orbital Approximations for Geometry Optimization of Large Systems: Test for N-Butane Conformation and S_N2 Reaction: RCl+Cl^-. *J. Chem. Phys.* **1996**, *105*, 1959–1967.

(45) Rappe, a. K.; Casewit, C. J.; Colwell, K. S.; Goddard III, W. a.; Skiff, W. M. UFF, a Full Periodic Table Force Field for Molecular Mechanics and Molecular Dynamics Simulations. *J. Am. Chem. Soc.* **1992**, *114*, 10024–10035.

(46) Shiota, Y.; Suzuki, K.; Yoshizawa, K. QM/MM Study on the Catalytic Mechanism of Benzene Hydroxylation over Fe-ZSM-5. *Organometallics* **2006**, *25*, 3118–3123.

(47) Wattanakit, C.; Nokbin, S.; Boekfa, B.; Pantu, P.; Limtrakul, J. Skeletal Isomerization of 1-Butene over Ferrierite Zeolite: A Quantum Chemical Analysis of Structures and Reaction Mechanisms. *J. Phys. Chem. C* **2012**, *116*, 5654–5663.

(48) Mosallanejad, S.; Dlugogorski, B. Z.; Kennedy, E. M.; Stockenhuber, M. HCl Adsorption on Copper-Modi Fi Ed ZSM-5 : FTIR and DFT Study. *J. Phys. Chem. C* **2013**, *117*, 19365–19372.

(49) Kumsapaya, C.; Bobuatong, K.; Khongpracha, P.; Tantirungrotechai, Y.; Limtrakul, J. Mechanistic Investigation on 1,5- to 2,6-Dimethylnaphthalene Isomerization Catalyzed by Acidic β Zeolite: ONIOM Study with an M06-L Functional. *J. Phys. Chem. C* **2009**, *113*, 16128–16137.

(50) Frisch, M. J.; Trucks, G. W.; Schlegel, H. B.; Scuseria, G. E.; Robb, M. A.; Cheeseman, J. R.; Scalmani, G.; Barone, V.; Mennucci, B.; Petersson, G. A.; Nakatsuji, H.; Li, X.; Caricato, M.; Marenich, A.; Bloino, J.; Janesko, B. G.; Gomperts, R.; Mennucci, B.; Hratchian, H. P.; et al. Gaussian 09. Gaussian, Inc., Wallingford CT 2009.

(51) Dzwigaj, S.; Che, M. Incorporation of Co(II) in Dealuminated BEA Zeolite at Lattice Tetrahedral Sites Evidenced by XRD, FTIR, Diffuse Reflectance UV-Vis, EPR, and TPR. *J. Phys. Chem. B* **2006**, *110*, 12490–12493.

(52) Bennur, T. H.; Srinivas, D.; Ratnasamy, P. EPR Spectroscopy of Copper and Manganese Complexes Encapsulated in Zeolites. *Microporous Mesoporous Mater.* **2001**, *48*, 111–118.

(53) Itadani, A.; Sugiyama, H.; Tanaka, M.; Ohkubo, T.; Yumura, T.; Kobayashi, H.; Kuroda, Y. Potential for C-H Activation in CH4 Utilizing a CuMFI-Type Zeolite as a Catalyst. *J. Phys. Chem. C* **2009**, *113*, 7213–7222.

(54) Kazansky, V. B.; Serykh, A. I.; Pidko, E. A. DRIFT Study of Molecular and Dissociative Adsorption of Light Paraffins by HZSM-5 Zeolite Modified with Zinc Ions: Methane Adsorption. *J. Catal.* **2004**, *225*, 369–373.

(55) Bacsa, J.; Hanke, F.; Hindley, S.; Odedra, R.; Darling, G. R.; Jones, A. C.; Steiner, A. The Solid-State Structures of Dimethylzinc and Diethylzinc. *Angew. Chemie - Int. Ed.* **2011**, *50*, 11889–11891.

(56) Almutairi, S. M. T.; Mezari, B.; Magusin, P. C. M. M.; Pidko, E. A.; Hensen, E. J. M. Structure and Reactivity of Zn-Modified ZSM-5 Zeolites : The Importance of Clustered Cationic Zn Complexes. *ACS Catal.* **2012**, *2*, 71–83.

(57) Pearson, R. G. Absolute Electronegativity and Hardness Correlated with Molecular Orbital Theory. *Proc. Natl. Acad. Sci. U. S. A.* **1986**, *83*, 8440–8441.

(58) Zhang, R.; Song, L.; Liu, H.; Wang, B. The Interaction Mechanism of CO2 with CH3 and H on Cu (111) Surface in Synthesis of Acetic Acid from CH4/CO2: A DFT Study. *Appl. Catal. A Gen.* **2012**, *443–444*, 50–58.

(59) Johansson, R.; Jarenmark, M.; Wendt, O. F. Insertion of Carbon Dioxide into (PCP)Pd ^{II} −Me Bonds. *Organometallics* **2005**, *24*, 4500–4502.

(60) Links, D. A. Exploring the Reactions of CO2 with PCP Supported Nickel Complexes. *Chem. Commun.* **2011**, *47*, 1824–1826.

(61) SAKAKI, S.; OHKUBO, K. Ab Initio MO Study of CO2 Insertion into a Cu(I)-H Bond. Semiquantitative Understanding of Changes in Geometry, Bonding, and Electron Distribution during the Reaction. *Inorg. Chem.* **1989**, *8*, 2583–2590.

(62) Johnson, M. T.; Johansson, R.; Kondrashov, M. V.; Steyl, G.; Ahlquist, M. S. G.; Roodt, A.; Wendt, O. F. Mechanisms of the CO2 Insertion into (PCP) Palladium Allyl and Methyl O-Bonds. A Kinetic and Computational Study. *Organometallics* **2010**, *29*, 3521–3529.

6 CHAPTER – CONCLUDING REMARKS

In this work, quantum mechanical calculations were employed to guide the design of efficient catalysts in an effort to seek renewable energy sources through the transformation of agricultural waste biomass into valuable chemicals. The properties of metal modified zeolites were studied along with their interaction with derived compounds of the biomass.

Two different polymorphisms of zeolite beta (BEA and BEC) substituted with Sn, Ti, and Ge were studied. Based on the hydrolysis energies, and for both polymorphisms, Ti-substituted zeolites have a higher hydrothermal stability than Sn and Ge substituted zeolites. FAU and MFI zeolites substituted with Sn and Ti were also analyzed. Among the zeolites that were studied, Sn-BEA has the highest Lewis acidity, which is manifested in the low binding energy of NH_3, the low hardness, and the highest charge transfer from NH_3 to the zeolite. Furthermore, the open sites in Sn-BEA form Brønsted acid sites, providing a double functionality to the catalyst, while also increasing the Lewis acidity. We also demonstrated that the Van der Waals (VDW) forces in the NH_3 binding energy on MFI are more significant than in BEA, BEC, and FAU zeolites. Furthermore, VDW forces decrease with increasing pore size of the zeolite.

In this work, we analyzed the reaction mechanism for the ring opening of glucose and fructose, which are two of the main sugars obtained from the acid hydrolysis of the biomass. Sn-, Ti-, Zr-, Hf-substituted BEA zeolites were systematically analyzed for both reactions. In average, the strongest adsorption of glucose and fructose were obtained in Hf-BEA and Zr-BEA, respectively. The lowest transition state energy for the glucose ring opening was obtained with Sn-BEA, while Hf-BEA has the lowest activation energy for the opening of the fructose ring. As far as we know, computational studies on the fructose ring opening have not been reported in the literature. Thus,

there are still many questions that future studies could address, such as the complete reaction mechanism for the conversion of fructose to the trioses.

We also studied the conversion of the greenhouse gases CH_4 with CO_2, the latter being a waste gas obtained from the conversion of biomass. We found that the CH_4 dissociation step is the reaction with the highest energy barrier, and Cu-MFI is the zeolite which requires less energy to dissociate the CH_4, with an apparent activation energy of 11.5 kcal/mol. Upon CH_4 dissociation, the charge of the metal atom decreases when compared to the charge of the metal on the isolated zeolite, indicating that the process is carried out through a charge transfer from the CH_4 to the metal atom. Furthermore, CO_2 insertion occurs though a S_E2 mechanism in which the M-C bond is maintained on the TS, and the protonation step to form adsorbed acetic acid is spontaneous. Finally, our results also demonstrated that the acetic acid desorption energy can be reduced from 42.0 kcal/mol to 20.5 kcal/mol with the co-adsorption of water molecules. The analysis was done using a specific aluminum arrangement in the zeolite ring. Future studies could addressed how the aluminum configurations affect the catalytic activity of these materials.

APPENDIX A - A DFT STUDY OF THE LEWIS ACIDITY AND RELATIVE HYDROTHERMAL STABILITY OF BEC AND BEA ZEOLITES SUBSTITUTED WITH TI, SN AND GE

A.1 Validation of the Exchange Correlation Functionals

A.1.1 Methodology

Three exchange correlation functionals (B3LYP, B3PW91 and ωB97XD) were analyzed, to select the one that best describes the properties of the materials. B3LYP and B3PW91 follow the formal structure of hybrid functionals suggested by Becke.[1] The major difference between them is the behavior in the slowly varying density limit. B3PW91 fulfills the uniform electron gas limit, whereas the LYP correlation energy functional is not correct in that limit.[2,3] Since Van der Waals forces play a crucial role in the substituted zeolites, we used ωB97XD, which is one of the latest functional developed from Head-Gordon's research group that includes empirical dispersion as described by Chai and coworkers.[4] Because ωB97XD is a relatively new functional, we are comparing the results with B3LYP and B3PW91 which are extensively used in the literature, but do not account for dispersion. In order to assess the exchange-correlation functionals to be employed in these calculations, we have systematically analyzed the three different functionals. The NMR shifts of Si-BEC, the optimized geometries of the zeolites and various vibrational frequencies were obtained with B3LYP, B3PW91 and ωB97XD. Results were compared with experimental data available in the literature.

NMR shifts of Si-BEC were calculated with clusters centered in each T-site, as shown in Figure A-1. The energy of each cluster was calculated as a single point using the structure reported in the literature of Si-BEC.[5] Hydrogen atoms were placed on the terminal atoms of the model where bonds were truncated. These hydrogen atoms were aligned along the truncated bond. Their

positions were calculated with the position vector and the covalent radii of the atoms involved in the bond. The Si-H bond distances were fixed at 1.5000 Å. The basis set 6-311+g** was used for the O, Si and H atoms. The NMR shielding tensors were computed with the Gauge-Independent Atomic Orbital (GIAO) method.[6]

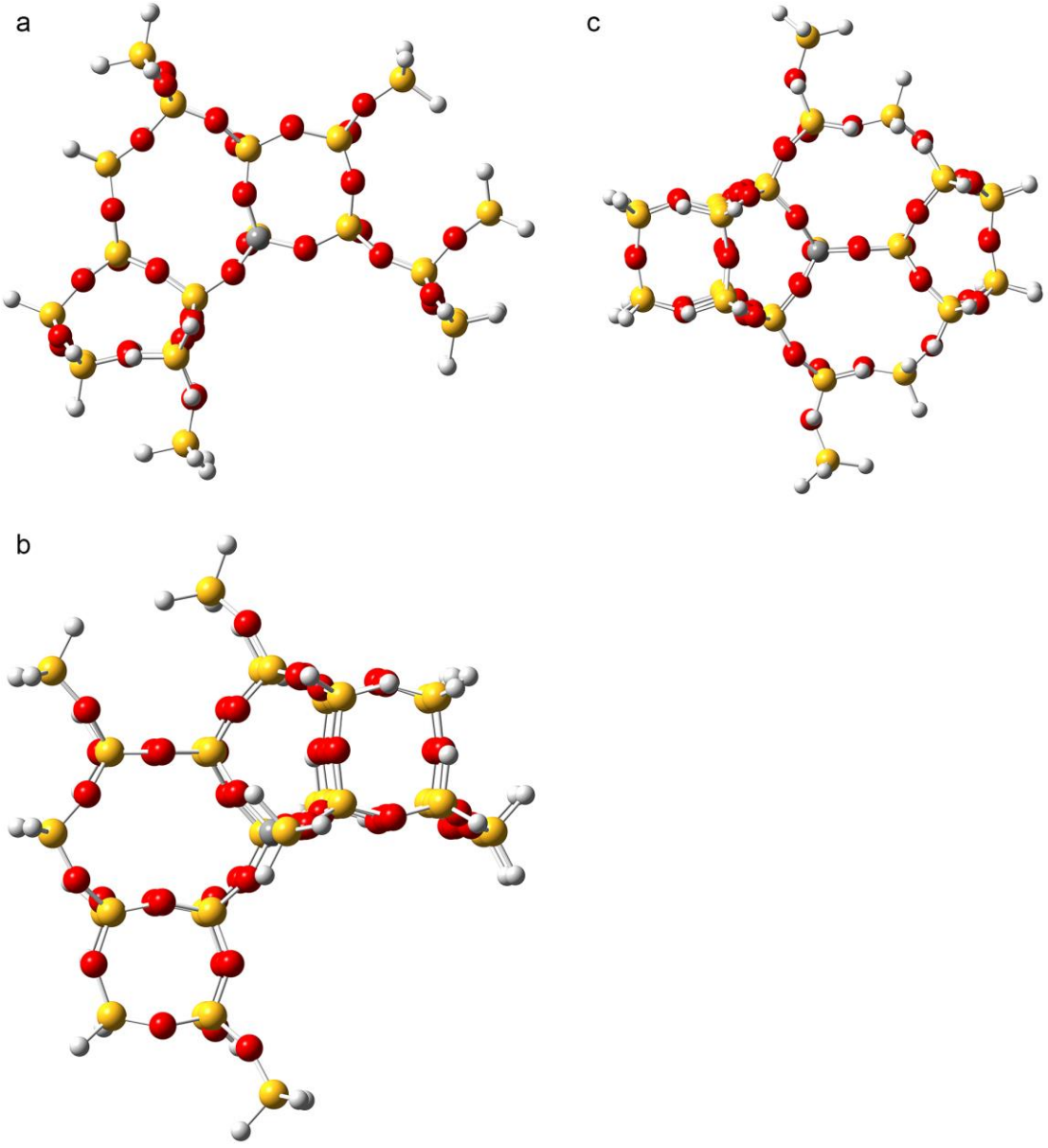

Figure A-1. Clusters of Si-BEC used for calculating the NMR shifts. a.) 117-atom cluster centered in T1 b.) 122-atom cluster centered in T2 c.) 128-atom cluster centered in T3. Color legend: yellow = Si; red = O; white = H; gray = Si atom centered on the T site.

Optimizations of the Si-BEC clusters (Figure A-2) centered in the T1 site were performed using the three functionals and the basis-set 6-31+g** for the O, Si and H atoms. All the silicon and oxygen atoms were optimized keeping fixed the hydrogen atoms. The optimized coordinates were compared with those reported in the literature.[5] Finally, vibrational frequency calculations were performed in order to assess the accuracy of the functionals. All calculations were carried out with the Gaussian 09 program package.[7]

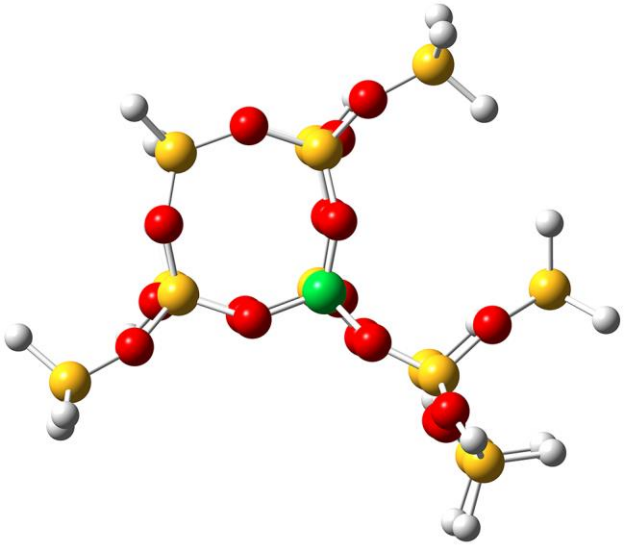

Figure A-2. 53-atom Si-BEC cluster centered in T1.

A.1.2 Results

Figure A-3 compares the crystallographic positions of Si-BEC with the calculated geometries obtained with the three functionals. The mean displacement of atoms from the X-ray diffraction (XRD) positions in the optimized geometries ($\overline{\Delta d}$) as defined in Equation A-1, was used to compare both geometries.

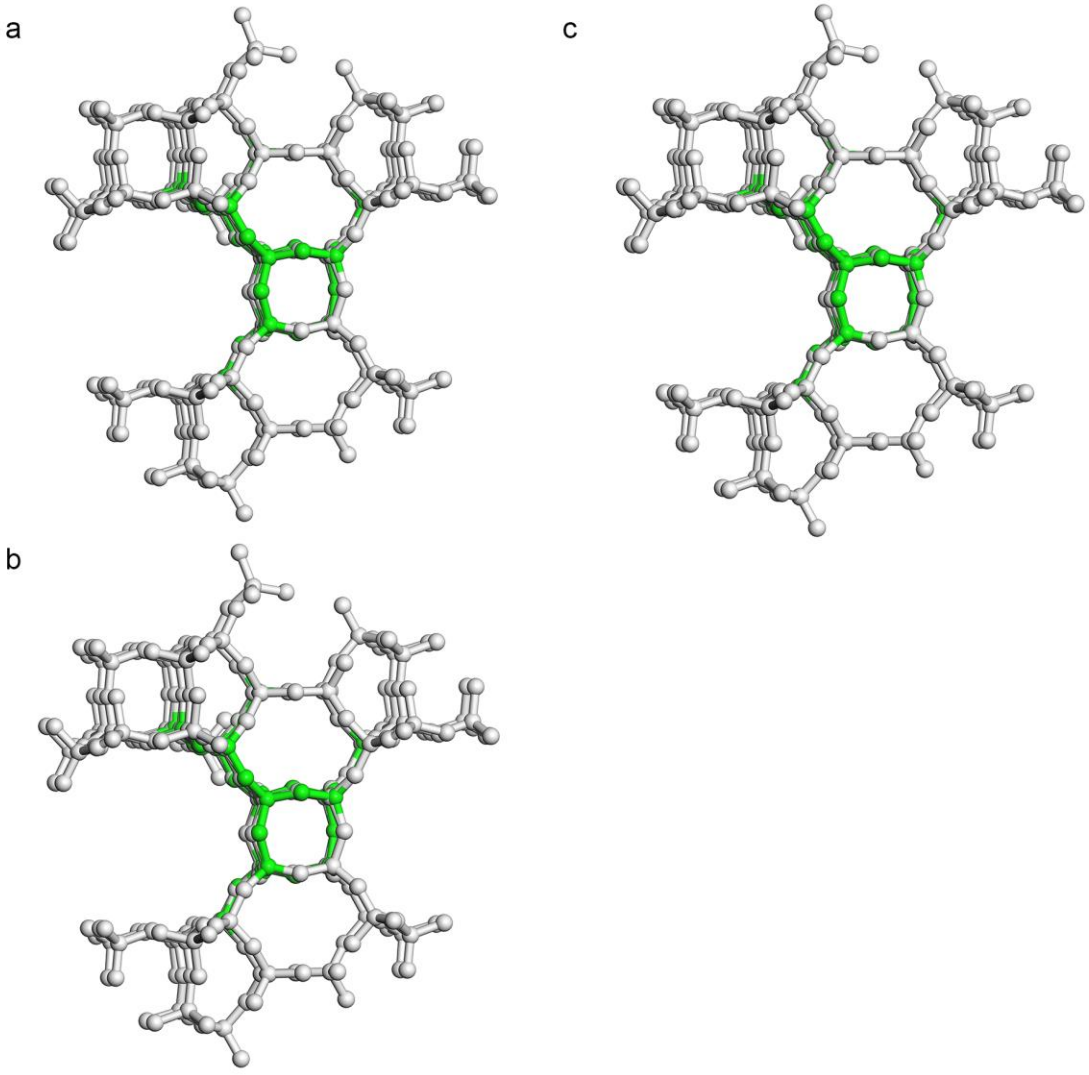

Figure A-3. Optimized geometries of Si-BEC obtained with three different functionals a.) B3LYP $\overline{\Delta \boldsymbol{d}}$= 0.191 Å, b.) B3PW91 $\overline{\Delta \boldsymbol{d}}$= 0.191 and c.) ωB97XD $\overline{\Delta \boldsymbol{d}}$= 0.189 Å. Green atoms correspond to the optimized geometries, gray atoms show the crystallographic positions of atoms.[5]

$$\overline{\Delta \mathrm{d}} = \frac{\sum_{i=1}^{N} \sqrt{\left(X_i^{DFT} - X_i^{XRD}\right)^2 + \left(Y_i^{DFT} - Y_i^{XRD}\right)^2 + \left(Z_i^{DFT} - Z_i^{XRD}\right)^2}}{N} \qquad \textbf{(1)}$$

In this equation, X_i^{DFT}, Y_i^{DFT}, Z_i^{DFT} are the coordinates of the Si or O atoms obtained with the geometry optimizations; X_i^{XRD}, Y_i^{XRD}, Z_i^{XRD} are the coordinates of the Si or O atoms according to the XRD values; and N is the total number of atoms. The mean displacement obtained with B3LYP, B3PW91 and ωB97XD are almost identical with values of 0.191Å, 0.191Å and 0.189Å,

respectively. Hence, all the functionals lead to comparable deviations of the XRD positions on this system.

Table A-1 compares experimental results of the Si-NMR shifts obtained by Moliner and coworkers[8] with the Si-NMR shifts obtained using the three functionals assessed in this study. The DFT calculations overestimate the experimental Si-NMR chemical shifts, except for the shift obtained for T1 using ωB97XD. By comparing the error percentage showed in Table A-1, the NMR shifts calculated with ωB97XD are closer to the experimental NMR shifts. It seems the chemical ambient of the silicon in the zeolites is better described by the long range functional ωB97XD.

Table A-1. NMR shifts obtained with B3LYP, B3PW91 and ωB97XD in Si-BEC (top) and percent difference (bottom) of the experimental Si MAS NMR spectra of calcinated pure silica BEC samples reported by Moliner and coworkers[8].

	B3LYP	B3PW91	ωB97XD	Experimental Values[8]
T1	-114.195 6.84%	-107.688 0.76%	-104.421 -2.30%	-106.88
T2	-128.651 10.17%	-121.542 4.09%	-118.272 1.29%	-116.77
T3	-122.962 11.03%	-116.381 5.08%	-111.026 0.25%	-110.75

Vibrational frequency calculations were carried out to compare the accuracy of the functionals in describing the properties of the zeolites. Table A-2**Error! Reference source not found.** compares the experimental vibrational frequencies of different metal substituted zeolites with the frequencies obtained with B3LYP, B3PW91 and ωB97XD. The first two rows show the vibrational frequencies corresponding to the OH stretching in germanol (3675 cm^{-1}) and silanol (3740 cm^{-1}) groups respectively.[9,10] The third row shows the vibrational frequency (960 cm^{-1}) corresponding to Ti species in framework positions.[11] Characteristic vibrational frequencies of the interaction of Sn-BEA with acetonitrile were calculated to determine how the functionals describe

the interaction of a guest molecule with the zeolites. The fourth row in Table A-2 shows the vibrational frequencies corresponding to the C≡N bond stretching (2308 cm^{-1}) on adsorbed Sn-BEA.[12] In general, results shown in Table A-1 and Table A-2**Error! Reference source not found.** demonstrate the three functionals accurately describe the properties of the zeolites. Errors (above 10%) were only obtained on the NMR shifts calculated using B3LYP. Since the ωB97XD functional best described the properties of the zeolites and takes into consideration the dispersion forces, this functional was used for subsequent calculations.

Table A-2. Vibrational frequencies of different metal substituted zeolites obtained with B3LYP, B3PW91 and ωB97XD (top) and the percentage difference (bottom) of the experimental vibrational frequencies reported in the literature.

Vibrational Frequencies (cm^{-1})	B3LYP	B3PW91	ωB97XD	Experimental
Ge-OH in Ge-BEC*	3801.21 3.43%	3804.35 3.52%	3855.89 4.92%	3675[10]
Si-OH in Ge-BEC**	3844.94 2.81%	3870.1 3.48%	3921.50 4.85%	3740[10]
Ti-BEC	970.02 1.04%	975.29 1.59%	962.85 0.30%	960[11]
Sn-BEA Acetonitrile	2375.76 2.85%	2389.76 3.42%	2403.93 3.99%	2308[12]

* Vibrational frequency due to the OH stretching in germanol
** Vibrational frequency due to the OH stretching in silanol

A.2 Validation of the Basis-Sets

Table A- 3. Influence of the sizes of the basis sets in the electronic properties.

		Si-BEC	Ge-BEC	Ti-BEC	Ti-BEA	Sn-BEC
ε_{LUMO} (A.U.)	6-31+G**	0.037	0.032	-0.002	-0.003	0.006
	6-311+G**	0.036	0.030	-0.003	-0.004	0.004
η (A.U.)	6-31+G**	0.4229	0.4176	0.3839	0.3838	0.3911
	6-311+G**	0.4233	0.4163	0.3836	0.3835	0.3899

A.3 Supplementary Data

Table A-4. Relative energies in kCal/mol for the three lowest spin states of Ti-BEC for each T-site.

kCal/mol	T1	T2	T3
Singlet	0	0	0
Triplet	114	148	139
Quintet	217	287	206

Table A-5. Relative energies, in kCal/mol for the three lowest spin states of Ti-BEA for each T-site.

	T1	T2	T3	T4	T5	T6	T7	T8	T9
Singlet	0	0	0	0	0	0	0	0	0
Triplet	102	*	105	102	105	105	107	*	102
Quintet	*	204	*	206	*	231	*	233	235

*The optimization did not converge.

** The values shown have as zero, the lowest energy found for each T-Site.

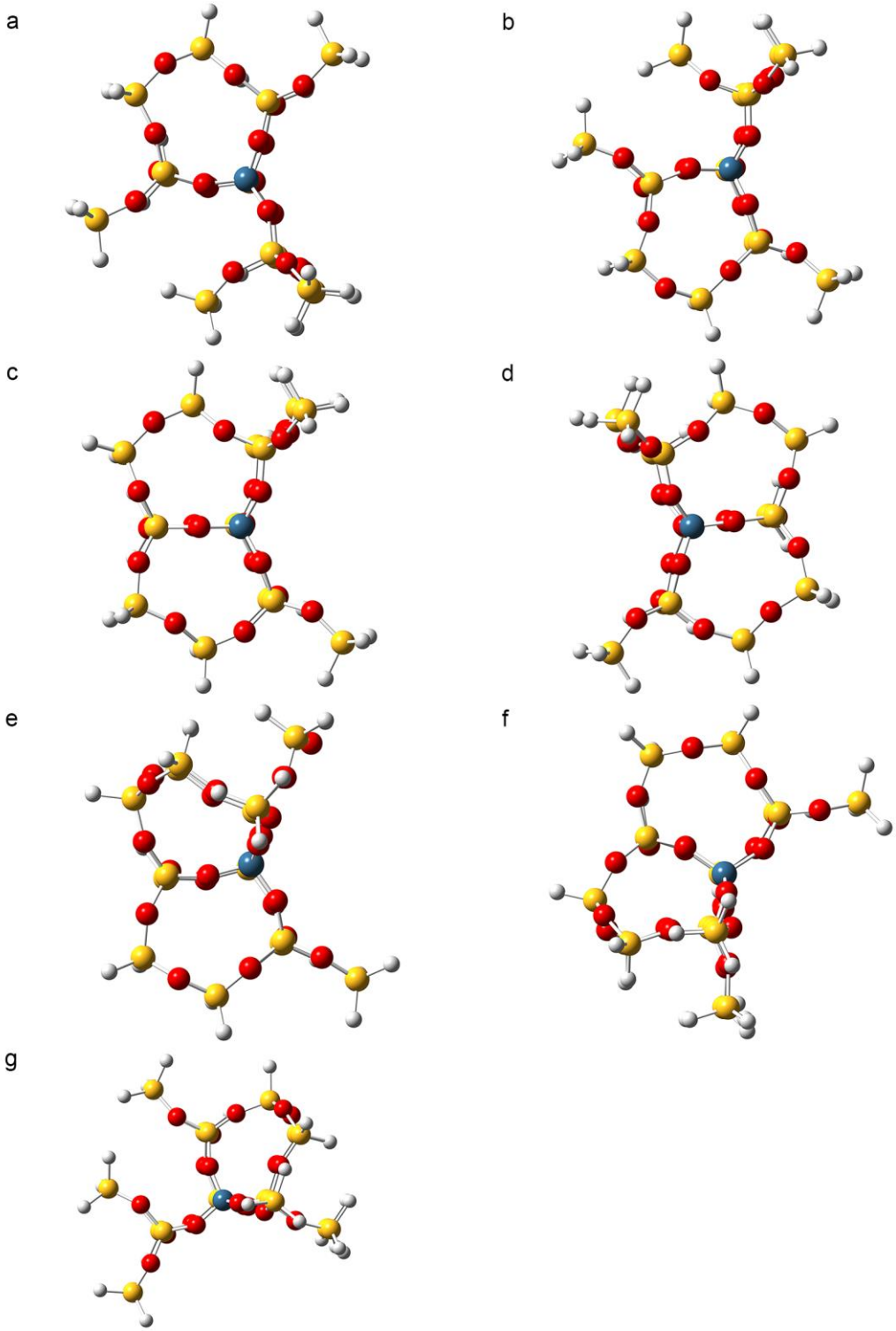

Figure A-4. Clusters used for the DFT calculations of Ti-BEA a.) 57-atom cluster centered in T3 b.) 57-atom cluster centered in T4 c.) 56-atom cluster centered in T5 d.) 56-atom cluster centered in T6 e.) 63-atom cluster centered in T7 f.) 64-atom cluster centered in T8 g.) 65-atom cluster centered in T9.

Table A-6. Preferential location of the heteroatoms (Ge,Sn, Ti) in BEC

ΔE_{rxn} (kcal/mol)	Ge-BEC	Sn-BEC	Ti-BEC
T1	22.12	29.78	18.95
T2	27.03	36.61	25.04
T3	26.72	34.75	22.31

Table A- 7. Preferential location of Ti in BEA

ΔE_{rxn} (kcal/mol)	T1	T2	T3	T4	T5	T6	T7	T8	T9
Ti-BEA	14.84	14.89	16.96	16.81	16.02	15.92	20.36	20.66	21.47

Table A-8. LUMO energies of Ge-BEC, Sn-BEC and Ti-BEC in the three T-sites.

ε_{LUMO} (A.U.)	Ge-BEC	Sn-BEC	Ti-BEC
T1	0.0320	0.0058	-0.0021
T2	0.0344	0.0151	0.0054
T3	0.0366	0.0060	0.0004

Table A-9. Hardness of Ge-BEC, Sn-BEC and Ti-BEC in the three T-sites.

η (A.U.)	Ge-BEC	Sn-BEC	Ti-BEC
T1	0.4176	0.3911	0.3839
T2	0.4189	0.3995	0.3897
T3	0.4192	0.3891	0.3826

Table A-10. NBO Charges of Ge, Sn and Ti in M-BEC for the three T-sites.

NBO Charges	Ge-BEC	Sn-BEC	Ti-BEC
T1	2.706	2.837	1.685
T2	2.722	2.846	1.718
T3	2.725	2.867	1.681

Table A-11. Local structural perturbation at the T-Site for Ge-BEC, Sn-BEC and Ti-BEC.

φ	Ge-BEC	Sn-BEC	Ti-BEC
T1	0.97	2.97	1.24
T2	0.58	1.88	0.62
T3	2.01	6.47	2.48

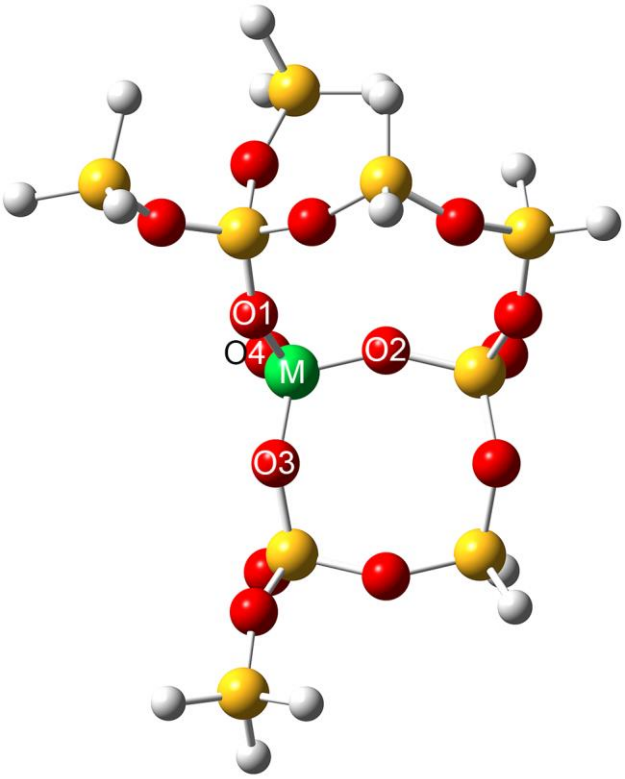

Figure A- 5. Bonds through which the hydrolysis can occur in M-BEC

Table A-12. Hydrolysis energies of M-BEC

ΔErxn (kcal/mol)	Si-BEC	Ge-BEC	Sn-BEC	Ti-BEC
O1	19.43	9.14	-4.34	-0.79
O2	35.55	25.58	4.59	8.11
O3	48.46	42.30	10.89	19.02
O4	34.63	21.00	6.58	8.95

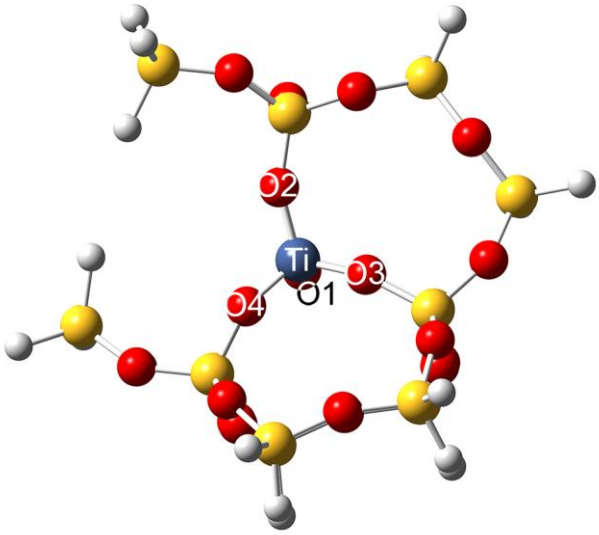

Figure A- 6. Bonds through which the hydrolysis can occur in Ti-BEA

Table A-13. Hydrolysis energies of Ti-BEA

ΔErxn (kcal/mol)	O1	O2	O3	O4
Ti-BEA	14.74	9.37	17.70	1.83

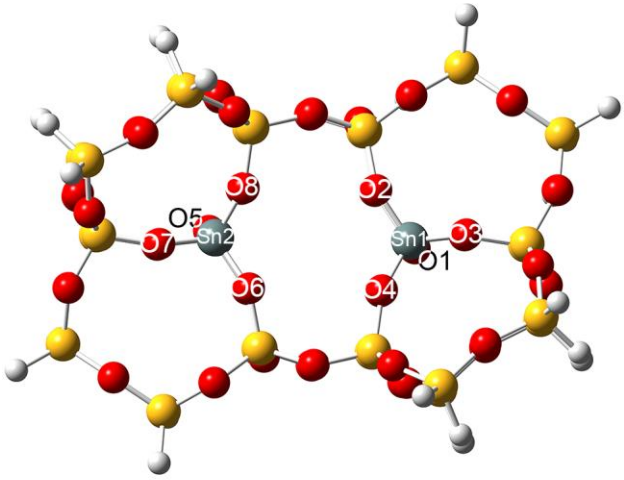

Figure A-7. Bonds through which the hydrolysis can occur in Sn-BEA

Table A-14. Hydrolysis energies of Sn-BEA

ΔErxn (kcal/mol)	Sn-BEA		Sn-BEA
O1	1.88	O5	3.99
O2	-2.94	O6	-6.35
O3	-2.17	O7	1.42
O4	-8.19	O8	-2.22

Table A-15. Summary of the properties of the hydrolyzed and non-hydrolyzed M-BEC, Sn-BEA and Ti-BEA

	ε_{LUMO} (A.U.)	η (A.U.)	NBO Charge	
Si-BEC	0.0371	0.4229	2.594	
Si-BEC_OH	0.0339	0.4149	2.567	
Ge-BEC	0.0320	0.4176	2.706	
Ge-BEC_OH	0.0292	0.4104	2.693	
Ti-BEC	-0.0021	0.3839	1.685	
Ti-BEC_OH	-0.0211	0.3513	1.570	
Ti-BEA	-0.0035	0.3838	1.694	
Ti-BEA_OH	-0.0197	0.3608	1.562	
Sn-BEC	0.0058	0.3911	2.837	
Sn-BEC_OH	0.0120	0.3923	2.847	
Sn-BEA	-0.0038	0.3841	Sn_1	2.879
			Sn_2	2.879
Sn-BEA_OH	-0.0109	0.3681	Sn_1	2.895
			Sn_2	2.876

Table A-16. Hydrolysis energies for M-BEC, Sn-BEA and Ti-BEA for different metal composition. For M-BEC the ratios M/Si are R1=1/13, R2=1/32, R3=1/64, R4=1/114; for Sn-BEA the ratios Sn/Si are R1=2/30, R2=2/50, R3=2/86, R4=2/148; for Ti-BEA the ratios Ti/Si are R1=1/15, R2=1/33, R3=1/62, R4=1/110.

$\Delta E_{Hydrolysis}$(kcal/mol) M/Si	Si-BEC	Ge-BEC	Ti-BEC	Ti-BEA	Sn-BEC	Sn-BEA
R1	19.43	9.14	-0.79	1.83	-4.87	-8.19
R2	20.68	10.21	-0.49	1.37	-3.83	-6.46
R3	20.69	10.23	-0.46	0.06	-3.80	-6.45
R4	20.67	10.27	-0.47	1.41	-3.80	-7.53

Table A-17. Local structural perturbation of M-BEC, Sn-BEA and Ti-BEA for different metal composition. For M-BEC the ratios M/Si are R1=1/13, R2=1/32, R3=1/64, R4=1/114; for Sn-BEA the ratios Sn/Si are R1=2/30, R2=2/50, R3=2/86, R4=2/148; for Ti-BEA the ratios Ti/Si are R1=1/15, R2=1/33, R3=1/62, R4=1/110.

φ M/Si	Ge-BEC	Ti-BEC	Ti-BEA	Sn-BEC	Sn-BEA
R1	0.80	1.05	1.00	2.63	2.97
R2	0.30	0.96	1.05	1.23	2.99
R3	0.30	1.00	2.00	1.20	2.97
R4	0.29	1.01	1.05	1.18	2.97

Table A-18. Hydrolysis Energies of M-BEC, Sn-BEA and Ti-BEA. For M-BEC the ratios M/Si are R1=1/13, R2=1/32, R3=1/64, R4=1/114; for Sn-BEA the ratios Sn/Si are R1=2/30, R2=2/50, R3=2/86, R4=2/148; for Ti-BEA the ratios Ti/Si are R1=1/15, R2=1/33, R3=1/62, R4=1/110.

$\Delta E_{Hydrolysis}$(kcal/mol) M/Si	Si-BEC	Ge-BEC	Ti-BEC	Ti-BEA	Sn-BEC	Sn-BEA
R1	62.67	-39.50	5.45	6.55	0.15	-2.45
R2	25.22	14.52	6.57	6.25	1.52	-0.37
R3	25.17	14.86	6.44	5.27	1.43	-0.47
R4	25.14	14.95	6.42	6.24	1.40	-1.52

Table A-19. Properties of the hydrolyzed and non-hydrolyzed M-BEC and Sn-BEA taking in consideration the solvent effect

	ε_{LUMO} (A.U.)	η (A.U.)	NBO Charge	
Si-BEC	0.0464	0.3759	2.655	
Si-BEC_OH	0.0382	0.4127	2.569	
Ge-BEC	0.0321	0.4088	2.703	
Ge-BEC_OH	0.0330	0.4076	2.697	
Ti-BEC	-0.0008	0.3807	1.713	
Ti-BEC_OH	-0.0171	0.3526	1.587	
Ti-BEA	0.0030	0.3857	1.725	
Ti-BEA_OH	-0.0141	0.3665	1.584	
Sn-BEC	0.0177	0.3992	2.933	
Sn-BEC_OH	0.0253	0.3993	2.927	
Sn-BEA	0.0038	0.3876	(Sn_1)	2.899
			(Sn_2)	2.899
Sn-BEA_OH	-0.0058	0.3768	(Sn_1)	2.888
			(Sn_2)	2.906

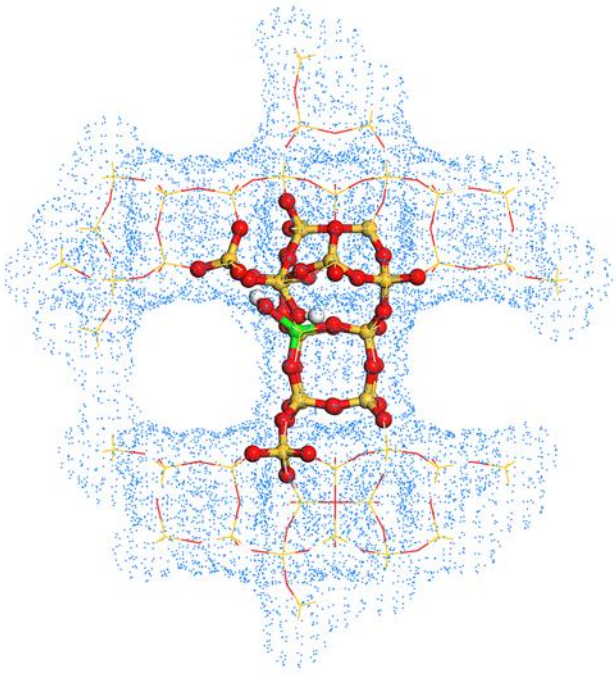

Figure A-8. Representation of the surface cavity used for the PCM calculations. The structure corresponds to the hydrolyzed Ge-BEC with a M/Si ratio of 1/114.

A.4 References

(1) Becke, A. D. Density-Functional Thermochemistry . III . The Role of Exact Exchange. *J. Chem. Phys.* **1993**, *98*, 5648–5652.

(2) Becke, A. D. Density-Functional Thermochemistry . IV . A New Dynamical Correlation Functional and Implications for Exact-Exchange Mixing. *J. Chem. Phys.* **1996**, *104*, 1040–1046.

(3) Tao, J.; Gori-Giorgi, P.; Perdew, J. P.; McWeeny, R. Uniform Electron Gas from the Colle-Salvetti Functional : Missing Long-Range Correlations. *Phys. Rev. A* **2001**, *63*, 032513–032517.

(4) Chai, J.-D.; Head-Gordon, M. Long-Range Corrected Hybrid Density Functionals with Damped Atom-Atom Dispersion Corrections. *Phys. Chem. Chem. Phys.* **2008**, *10*, 6615–6620.

(5) Corma, A.; Navarro, M. T.; Rey, F.; Rius, J.; Valencia, S. Pure Polymorph C of Zeolite Beta Synthesized by Using Framework Isomorphous Substitution as a Structure-Directing Mechanism. *Angew. Chem. Int. Ed. Engl* **2001**, *40*, 2277–2280.

(6) Wolinski, K.; Hinton, J. F.; Pulay, P. Efficient Implementation of the Gauge-Independent Atomic Orbital Method for NMR Chemical Shift Calculations. *J. Am. Chem. Soc.* **1990**, *112*, 8251–8260.

(7) M.J. Frisch, G.W. Trucks, H.B. Schlegel, G.E. Scuseria, M.A. Robb, J.R. Cheeseman, G. Scalmani, V. Barone, B. Mennucci, G.A. Petersson, H. Nakatsuji, M. Caricato, X. Li, H.P. Hratchian, A.F. Izmaylov, J. Bloino, G. Zheng, J.L. Sonnenberg, M. Hada, M. Ehara, K. Toyota, R. Fukuda, J. Hasegawa, M. Ishida, T. Nakajima, Y. Honda, O. Kitao, H. Nakai, T. Vreven, J.A. Montgomery, J.E.J. Peralta, F. Ogliaro, M. Bea park, J.J. Heyd, E. Brothers, K.N. Kudin, V.N. Staroverov, R. Kobayashi, J. Normand, K. Raghavachari, A. Rendell, J.C. Burant, S.S. Iyengar, J. Tomasi, M. Cossi, N. Rega, J.M. Millam, M. Klene, J.E. Knox, J.B. Cross, V. Bakken, C. Adamo, J. Jaramillo, R. Gomperts, R.E. Stratmann, O. Yazyev, A.J. Austin, R. Cammi, C. Pomelli, J.W. Ochterski, R.L. Martin, K. Morokuma, V.G. Zakrzewski, G.A. Voth, P. Salvador, J.J. Dannenberg, S. Dapprich, A.D. Daniels, Ö. Farkas, J.B. Foresman, J.V. Ortiz, J. Cioslowski, J.D. Fox, Gaussian 09 Revision A.02, Gaussian, Inc., Wallingford, CT, 2009.

(8) Moliner, M.; Serna, P.; Cantín, A.; Sastre, G.; Díaz-cabanas, M. J.; Corma, A. Synthesis of the Ti - Silicate Form of BEC Polymorph of -Zeolite Assisted by Molecular Modeling. *J. Phys. Chem. C* **2008**, *112*, 19547–19554.

(9) Moliner, M.; Diaz-Cabanas, M.; Fornes, V.; Martinez, C.; Corma, A. Synthesis Methodology, Stability, Acidity, and Catalytic Behavior of the 18×10 Member Ring Pores ITQ-33 Zeolite. *J. Catal.* **2008**, *254*, 101–109.

(10) Kosslick, H.; Tuan, V. a.; Fricke, R.; Peuker, C.; Pilz, W.; Storek, W. Synthesis and Characterization of Ge-ZSM-5 Zeolites. *J. Phys. Chem.* **1993**, *97*, 5678–5684.

(11) Taramasso, M.; Milanese, S.; Perego, G.; Milan; Notari, B. Preparation of Porous Crystalline Synthetic Material Comprised of Silicon and Titanium Oxides. US4410501 A, 1982.

(12) Boronat, M.; Concepcion, P.; Corma, a; Renz, M.; Valencia, S. Determination of the Catalytically Active Oxidation Lewis Acid Sites in Sn-Beta Zeolites, and Their Optimisation by the Combination of Theoretical and Experimental Studies. *J. Catal.* **2005**, *234*, 111–118.

APPENDIX B – DFT STUDY OF CLOSED AND OPEN SITES OF BEA, BEC, FAU, MFI ZEOLITES SUBSTITUTED WITH SN AND TI

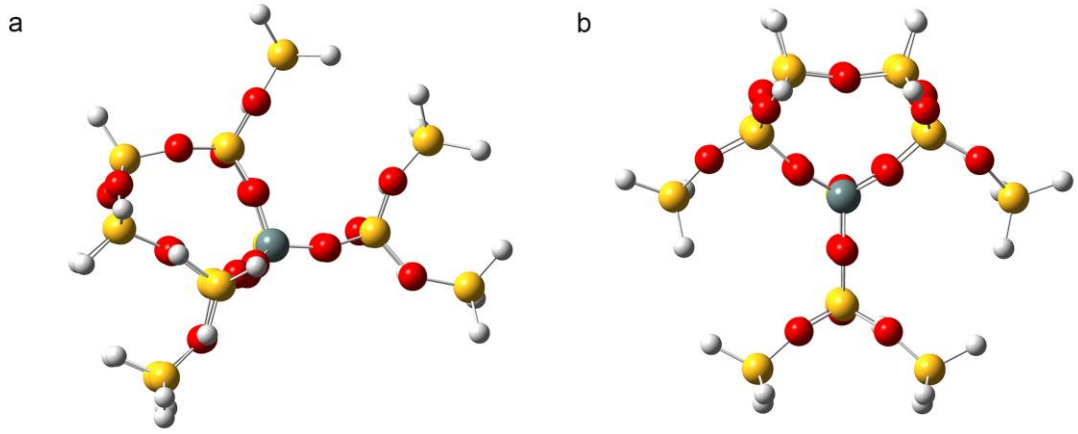

Figure B-1. M-BEC clusters centered in a.) T2 (65 atoms) b.) T3 (60 atoms)

Table B-1. Preferential location of the heteroatoms Sn and Ti in BEC.

ΔE_{rxn} (kJ/mol)	Sn-BEC	Ti-BEC
T1	124.60	79.29
T2	153.18	104.77
T3	145.39	93.35

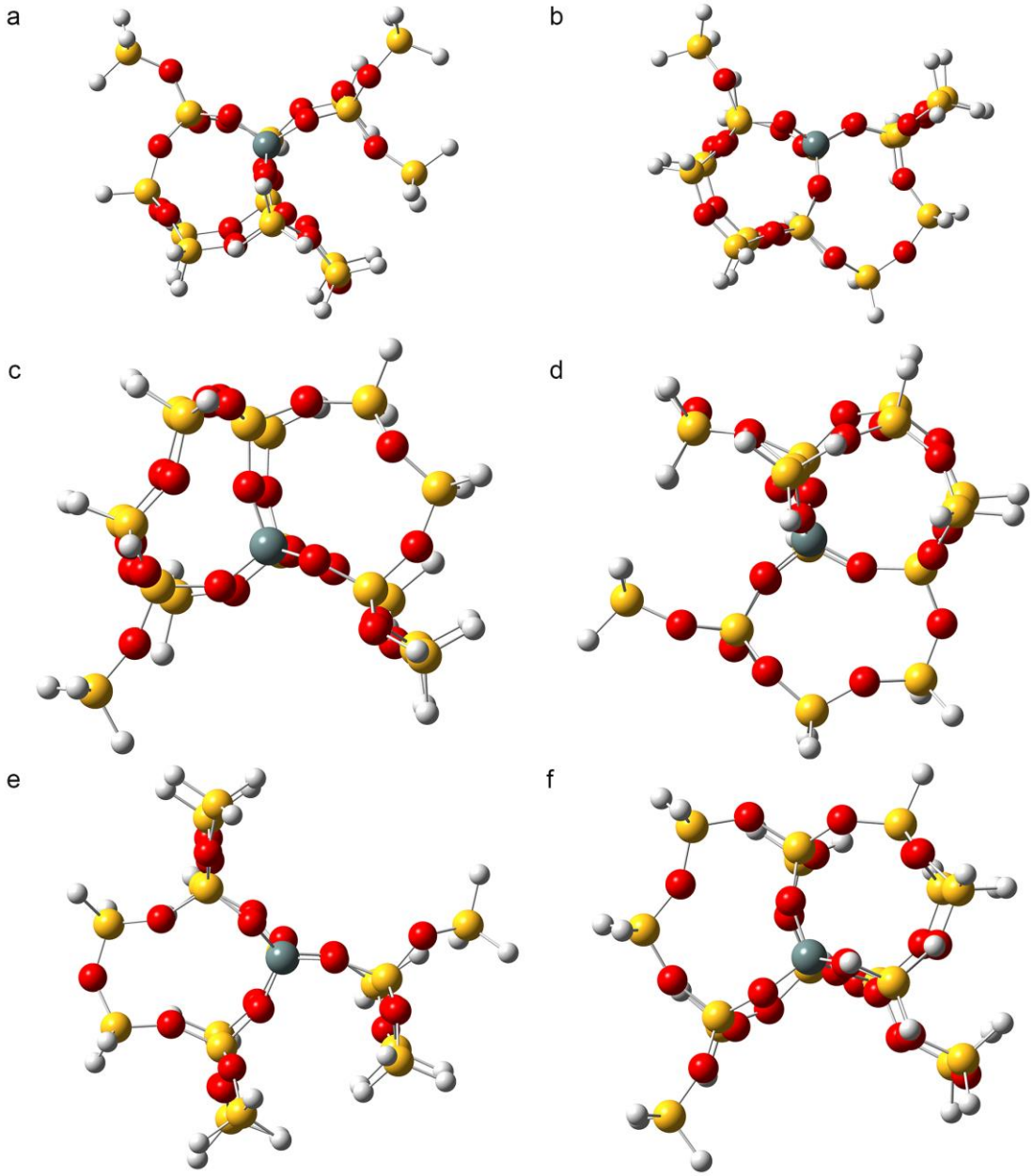

Figure B-2. M-MFI clusters centered in a.) T1 (64 atoms) b.) T2 (63 atoms) c.) T3 (63 atoms) d.) T4 (63 atoms) e.) T5 (65 atoms) f.) T6 (63 atoms)

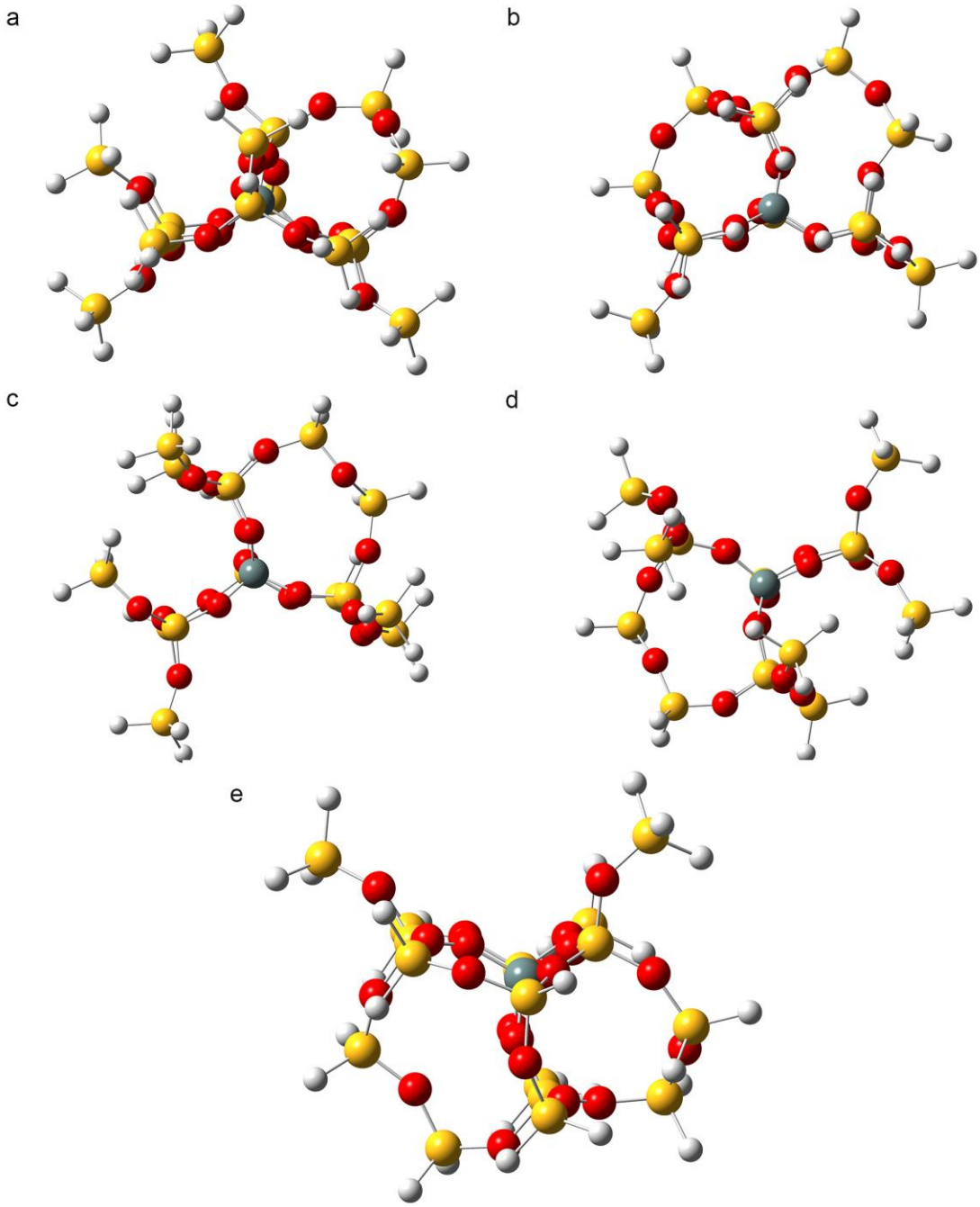

Figure B-3. M-MFI clusters centered in a.) T7 (66 atoms) b.) T8 (64 atoms) c.) T9 (61 atoms) d.) T10 (61 atoms) e.) T12 (65 atoms)

Table B-2. Preferential location of the heteroatoms Sn and Ti in MFI.

ΔE_{rxn} (kJ/mol)	Sn-MFI	Ti-MFI
T1	167.53	118.70
T2	146.61	113.72
T3	155.94	114.93
T4	153.59	108.45
T5	149.45	110.79
T6	164.43	118.91
T7	144.22	106.32
T8	145.98	112.01
T9	144.26	102.34
T10	141.88	100.16
T11	132.51	101.55
T12	150.83	110.96

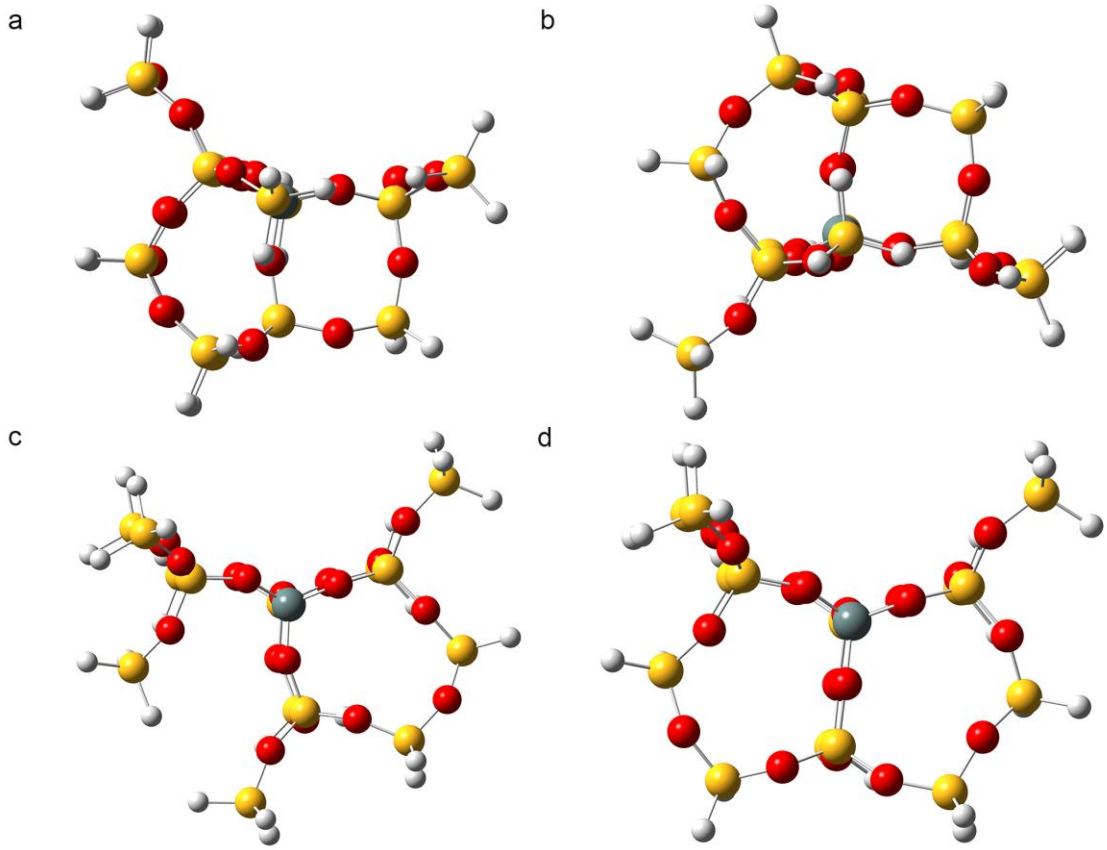

Figure B-4. M-BEA clusters centered in a.) T1 (59 atoms) b.) T3 (57 atoms) c.) T4 (57 atoms) d.) T5 (56 atoms)

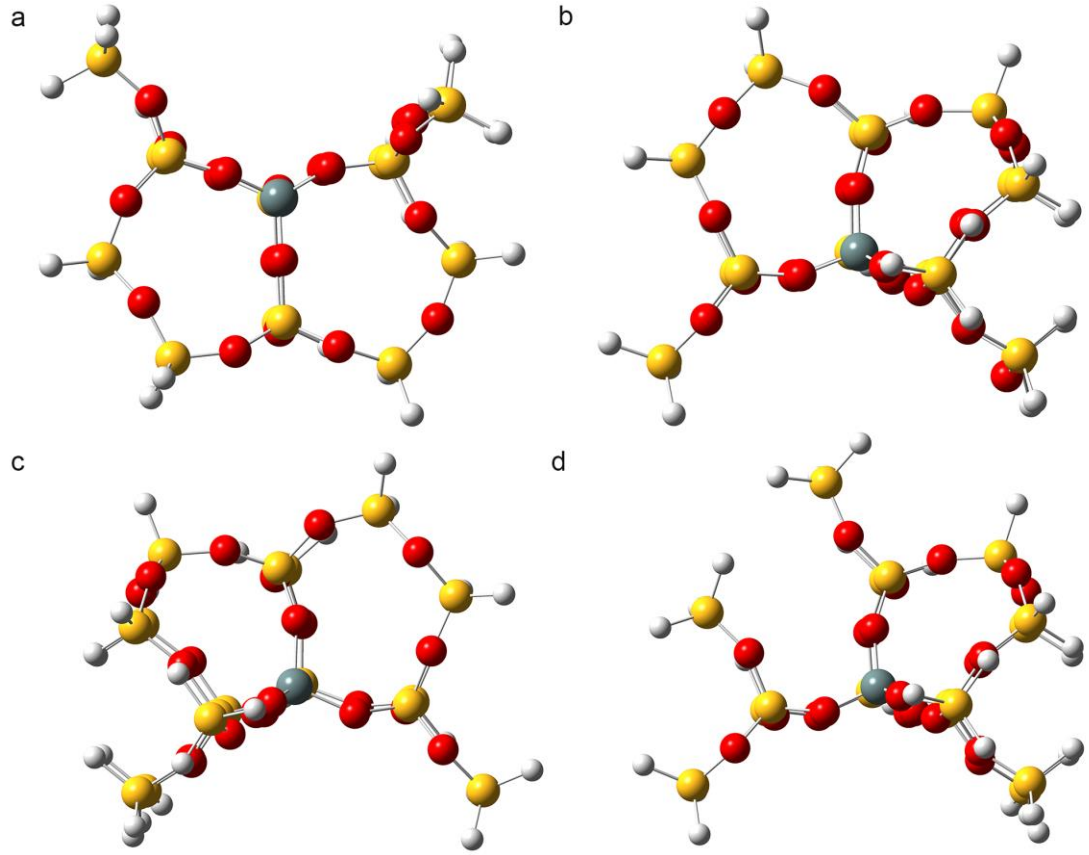

Figure B-5. M-BEA clusters centered in a.) T6 (56 atoms) b.) T7 (63 atoms) c.) T8 (64 atoms) d.) T9 (65 atoms)

Table B-3. Preferential location of Ti in BEA

ΔE_{rxn} (kJ/mol)	T1	T2	T3	T4	T5	T6	T7	T8	T9
Ti-BEA	62.09	62.30	70.96	70.33	67.03	66.61	85.19	86.44	89.83

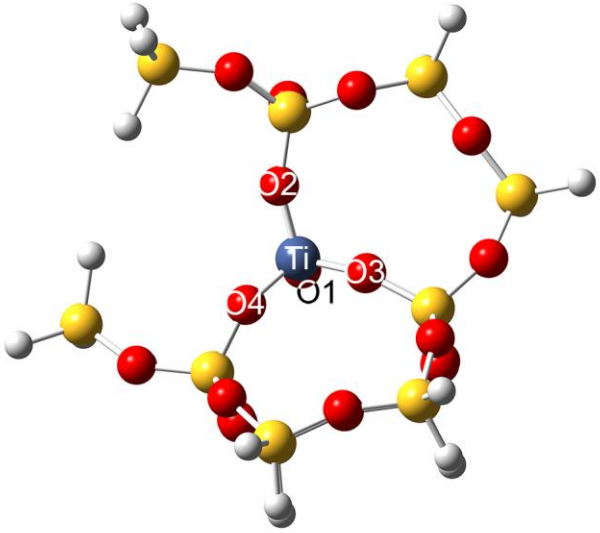

Figure B-6. Bonds through which the hydrolysis can occur in Ti-BEA.

Table B-4. Hydrolysis energies of Ti-BEA.

ΔErxn (kJ/mol)	O1	O2	O3	O4
Ti-BEA	61.67	39.20	74.06	7.66

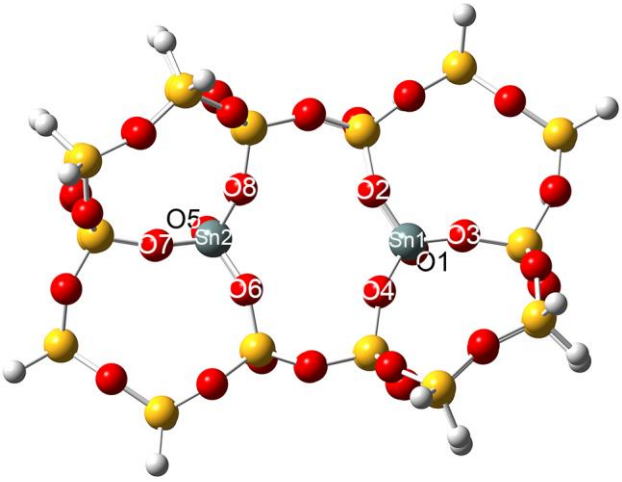

Figure B-7. Bonds through which the hydrolysis can occur in Sn-Sn-BEA.

Table B-5. Hydrolysis energies of Sn-BEA

ΔErxn (kJ/mol)	Sn- BEA		Sn- BEA
O1	7.87	O5	16.69
O2	-12.30	O6	-26.57
O3	-9.08	O7	5.94
O4	-34.27	O8	-9.29

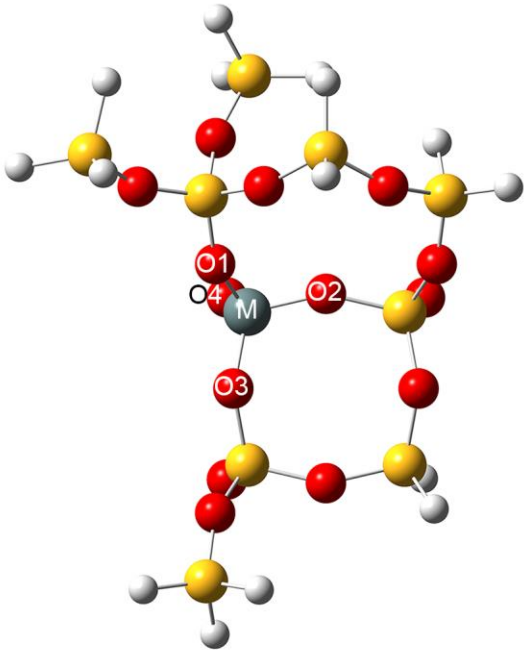

Figure B-8. Bonds through which the hydrolysis can occur in M-BEC.

Table B-6. Hydrolysis energies of M-BEC.

ΔErxn (kJ/mol)	Sn-BEC	Ti-BEC
O1	-18.16	-3.31
O2	19.20	33.93
O3	45.56	79.58
O4	27.53	37.45

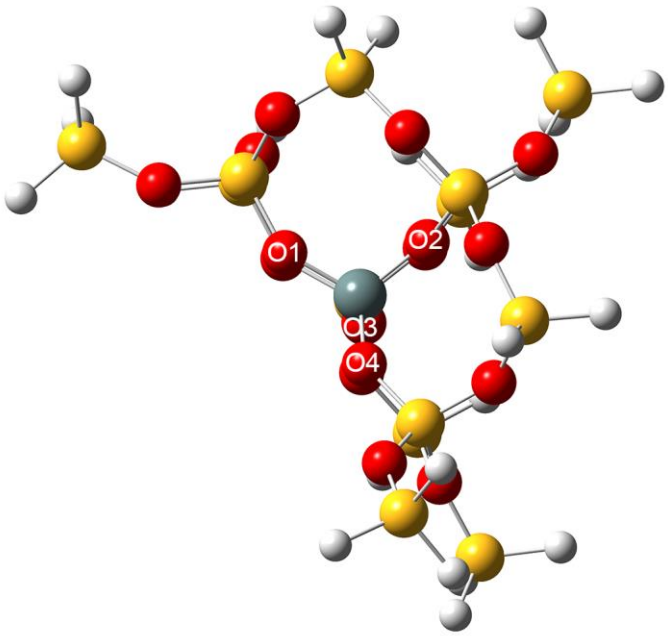

Figure B-9. Bonds through which the hydrolysis can occur in M-FAU.

Table B-7. Hydrolysis energies of M-FAU

ΔErxn (kJ/mol)	Sn-FAU	Ti-FAU
O1	41.71	56.40
O2	25.15	54.94
O3	17.87	23.64
O4	-39.08	-15.65

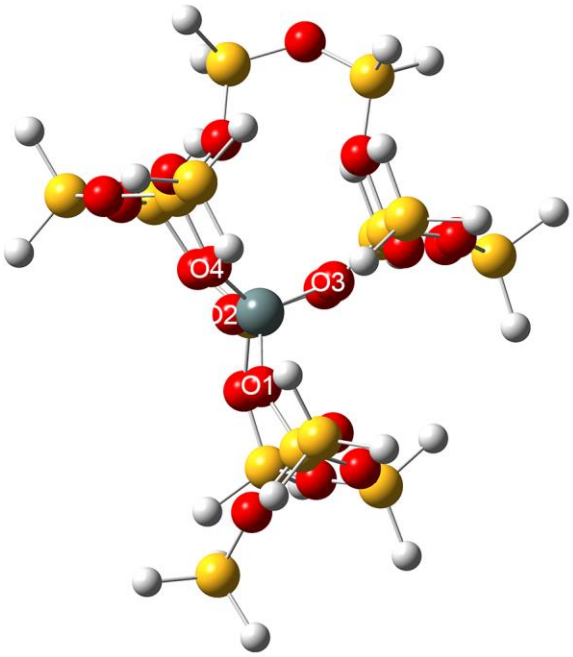

Figure B-10. Bonds through which the hydrolysis can occur in M-MFI.

Table B-8. Hydrolysis energies of M-MFI

ΔErxn (kJ/mol)	Sn-MFI	Ti-MFI
O1	76.94	104.18
O2	77.49	102.26
O3	-5.77	5.23
O4	13.22	24.89

Preferential Location of Al in BEA

The preferential location of Al in BEA was calculated with the electronic energy difference between the zeolite substituted with Al and the pure zeolite. The clusters that were used for these calculations are shown in the Figure B-4, Figure B-5 and Figure 3-1 a. When Al is substituted in the zeolite, the negative charge is compensated with a proton in one of the four oxygens bonded to Al (O1 to O4). The electronic energies differences are shown in Table B-9, and the lowest energy obtained (T2-O4) was set as zero. On the basis of Table B-9, the preferential location of Al in BEA was in T2 with the proton bonded to either O4 or O1. Despite T2-O4 has slighlty lower energy than T2-O1, with a difference in energy of 0.78 kJ/mol, the proton in the former

configuration is not exposed to the pore. Hence, T2-O1 was selected as the preferential location of Al in BEA. The ONIOM cluster used for the calculation of the deprotonation energy is shown in the Figure B-11.

Table B-9. Preferential location of Al in BEA.

Site	Bond	Energy (kJ/mol)	Site	Bond	Energy (kJ/mol)	Site	Bond	Energy (kJ/mol)
T1	O1	1.82	T2	O1	0.78	T3	O1	12.83
	O2	8.12		O2	8.50		O2	20.09
	O3	0.84		O3	1.92		O3	13.22
	O4	44.56		O4	0.00		O4	4.85
T4	O1	14.04	T5	O1	7.04	T6	O1	8.01
	O2	12.48		O2	5.91		O2	5.28
	O3	4.70		O3	9.28		O3	15.60
	O4	19.97		O4	15.43		O4	11.64
T7	O1	5.85	T8	O1	10.14	T9	O1	17.95
	O2	5.85		O2	11.28		O2	17.95
	O3	20.06		O3	7.74		O3	18.01
	O4	19.96		O4	22.66		O4	10.02

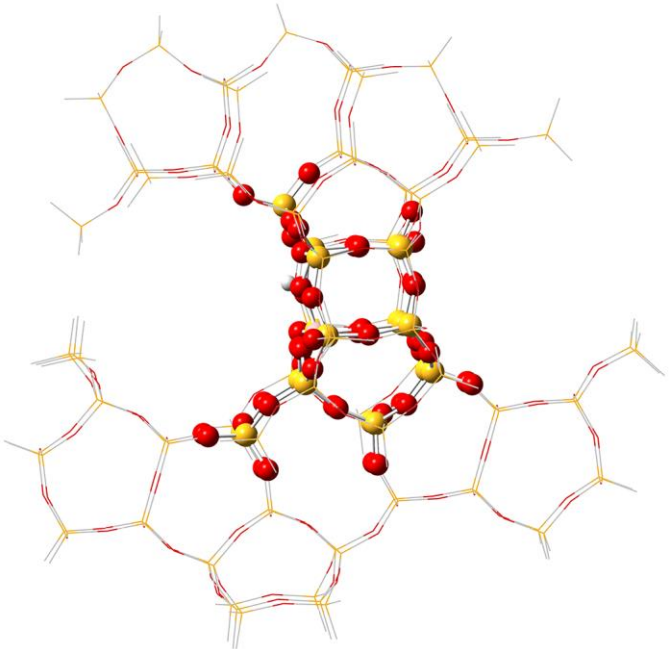

Figure B-11. ONIOM cluster of Al-BEA.Color legend: yellow = Si; red = O; white = H; pink = Al

Table B-10. Difference between the binding energy calculated using the ONIOM cluster and the binding energy calculated using the DFT cluster for each zeolite

Zeolites	Energy Difference (kJ/mol)
Sn-BEA	8.08
Sn-BEC	4.66
Sn-FAU	-9.82
Sn-MFI	-20.21
Ti-BEA	0.70
Ti-BEC	-5.04
Ti-FAU	-10.61
Ti-MFI	-22.37

Table B-11. VDW forces contributions to the ONIOM binding energies of NH3 on the metal substituted zeolites.

Energy (kJ/mol)	DFT	VDW	Total
Sn-BEA	-87.41	-21.47	-108.88
Sn-BEC	-77.08	-18.06	-95.14
Sn-FAU	-72.01	-17.83	-89.84
Sn-MFI	-69.94	-24.55	-94.49
Ti-BEA	-46.17	-23.21	-69.38
Ti-BEC	-53.11	-18.86	-71.97
Ti-FAU	-52.08	-18.55	-70.64
Ti-MFI	-48.93	-25.62	-74.55

Table B-12. Difference between the binding energy calculated using the ONIOM cluster in water and the binding energy calculated using the ONIOM cluster in vacuum for each zeolite.

Zeolites	Energy Difference (kJ/mol)
Sn-BEA	10.23
Sn-BEC	18.44
Sn-FAU	0.13
Sn-MFI	30.28
Ti-BEA	25.48
Ti-BEC	13.82
Ti-FAU	1.95
Ti-MFI	23.56

APPENDIX C – CLOSED SITES OF M-BETA (M = SN, TI, ZR, OR HF) ZEOLITES CAN OPEN GLUCOSE AND FRUCTOSE RINGS IN ONE ELEMENTARY STEP.

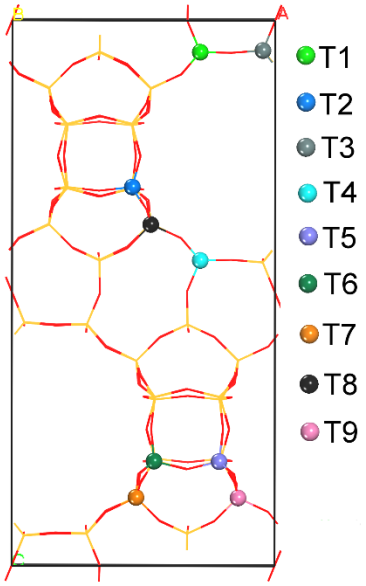

Figure C- 1. BEA unit cell and its nine crystallographic sites (T1 to T9).

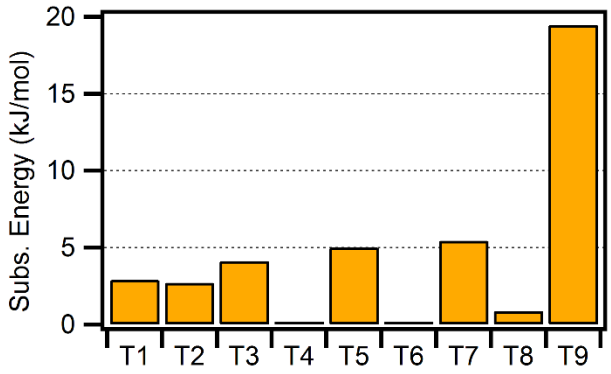

Figure C- 2. Relative substitution energies of Sn in BEA T-sites.

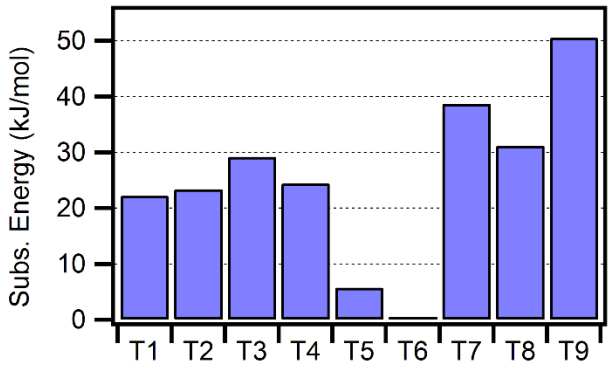

Figure C- 3. Relative substitution energies of Hf in BEA T-sites.

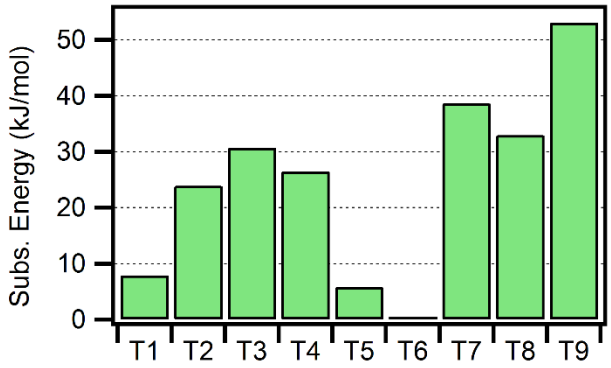

Figure C- 4. Relative substitution energies of Zr in BEA T-sites.

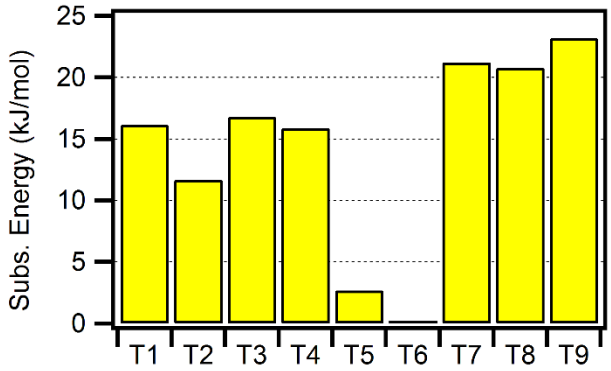

Figure C- 5. Relative substitution energies of Ti in BEA T-sites.

Table C- 1. Optimized distances for the adsorption of glucose in M-BEA.

	Sn-BEA	Hf-BEA	Zr-BEA	Ti-BEA
$d_{O1\text{-}M}$ (Å)	2.335	2.334	2.373	2.369
$d_{O2\text{-}M}$ (Å)	2.374	2.376	2.401	2.567
$d_{O3\text{-}M}$ (Å)	2.246	2.262	2.293	2.229
$d_{O4\text{-}M}$ (Å)	2.274	2.301	2.325	2.291
$d_{O5\text{-}M}$ (Å)	3.014	2.841	2.806	3.365
$d_{O6\text{-}M}$ (Å)	2.243	2.255	2.328	2.222

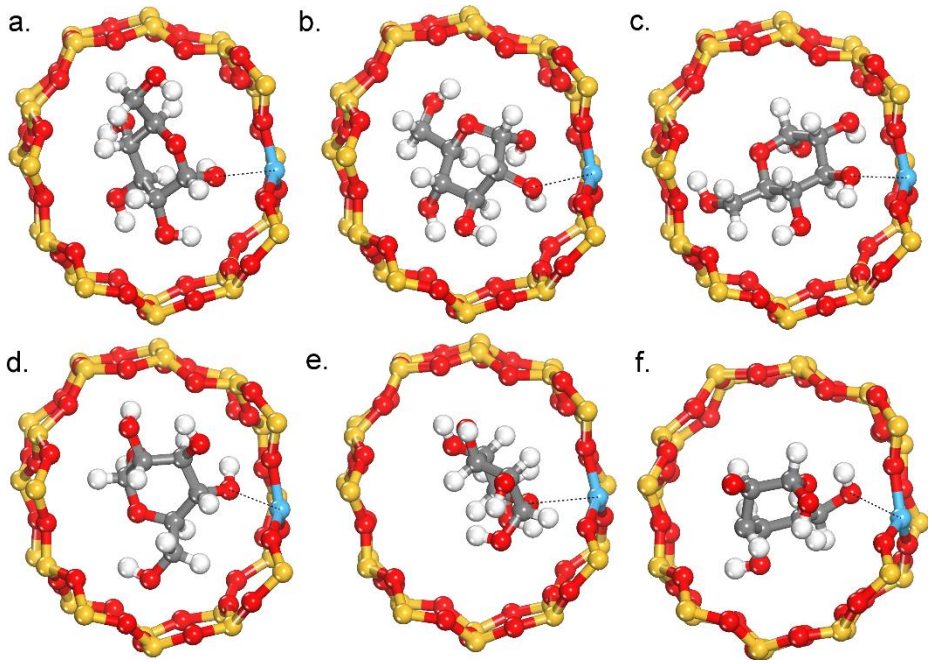

Figure C- 6. Optimized geometries for the adsorption of glucose through (a) O1, (b) O2, (c) O3, (d) O4, (e) O5, (f) O6 on M-BEA.

Table C- 2. Optimized distances for the adsorption of fructose in M-BEA.

	Sn-BEA	Hf-BEA	Zr-BEA	Ti-BEA
d_{O1-M} (Å)	2.262	2.298	2.322	2.248
d_{O2-M} (Å)	2.368	2.348	2.381	2.440
d_{O3-M} (Å)	2.368	2.367	2.414	2.454
d_{O4-M} (Å)	2.409	2.393	2.502	2.658
d_{O5-M} (Å)*	2.609	2.547	2.587	2.735
d_{O6-M} (Å)*	(2.179)	(2.207)	(2.246)	(2.166)
d_{O6-M} (Å)	2.218	2.231	2.276	2.192

***Bidentate mode**

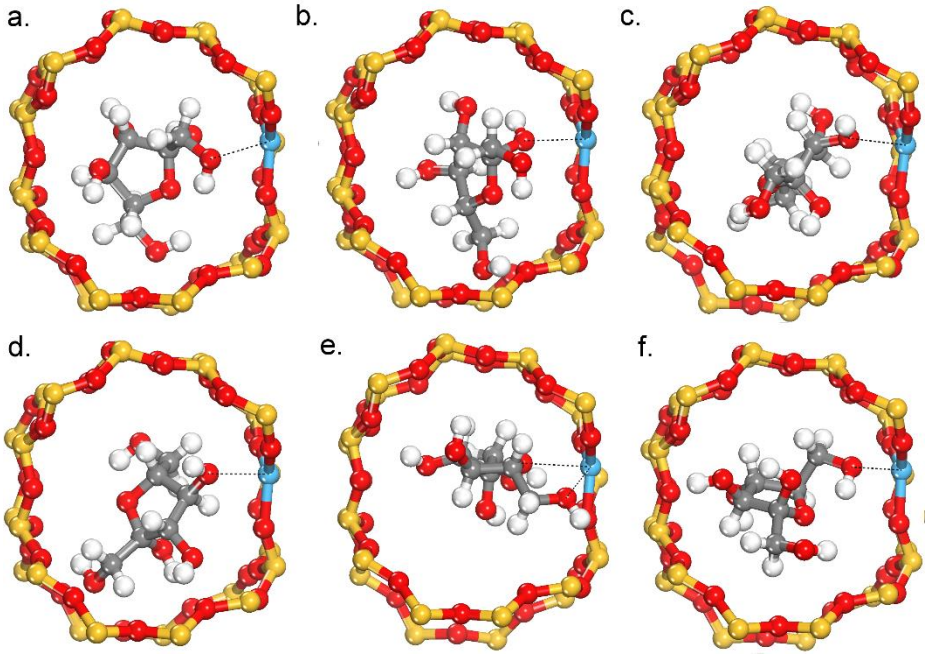

Figure C- 7. Optimized geometries for the adsorption of fructose through (a) O1, (b) O2, (c) O3, (d) O4, (e) O5, (f) O6 on M-BEA.

APPENDIX D - DFT STUDY TO UNRAVEL THE CATALYTIC PROPERTIES OF M-EXCHANGED MFI, (M = BE, CO, CU, MG, MN, ZN) FOR THE CONVERSION OF METHANE AND CARBON DIOXIDE TO ACETIC ACID.

Table D-1. Changes in the NBO charge of the carbon atom through CH_4 dissociation obtained with DFT.

	C in A	C in B	C in C
Be-MFI	-0.97	-0.98	-1.43
Co-MFI		-0.99	-1.29
Cu-MFI		-0.99	-1.04
Mg-MFI		-1.03	-1.49
Mn-MFI		-1.00	-1.39
Zn-MFI		-1.00	-1.39

Table D-2. Changes in the NBO charge of the metal atom through CH_4 dissociation obtained with DFT.

	M in A	M in B	M in C
Be-MFI	1.319	1.315	1.307
Co-MFI	1.294	1.156	1.123
Cu-MFI	1.251	1.184	0.883
Mg-MFI	1.614	1.525	1.502
Mn-MFI	1.387	1.173	1.244
Zn-MFI	1.431	1.326	1.325

Table D-3. Energy contributions in kcal/mol to CH_4 adsorption energies obtained with ONIOM.

	DFT	Stretching, bending, and torsion	Disp.	Total
Be-MFI	-0.71	-0.11	-7.86	-8.69
Co-MFI	-0.44	-0.23	-8.26	-8.93
Cu-MFI	-2.65	-0.17	-8.20	-11.02
Mg-MFI	-4.96	-0.30	-8.66	-13.92
Mn-MFI	-5.12	-0.37	-8.28	-13.77
Zn-MFI	-4.26	-0.40	-8.40	-13.06

Table D-4. Energy contributions in kcal/mol to CH_4 dissociation energies obtained with ONIOM.

	DFT	Stretching, bending, and torsion	Disp.	Total
Be-MFI	22.18	-2.01	-0.18	19.98
Co-MFI	21.86	-2.24	0.20	19.82
Cu-MFI	10.36	-2.71	-0.09	7.57
Mg-MFI	40.96	-1.96	0.44	39.43
Mn-MFI	31.04	-1.36	-0.39	29.30
Zn-MFI	10.74	-1.72	-0.17	8.85

Table D- 5. Energy contributions in kcal/mol to the TS energies of CH_4 dissociation obtained with ONIOM.

	DFT	Stretching, bending, and torsion	VDW	Total
Cu-MFI	24.30725	-2.44235	0.673359	22.53826
Zn-MFI	30.11197	-1.94533	0.563884	28.73053

Table D- 6. Geometric parameters of the TS for CH_4 dissociation on Cu-MFI obtained with ONIOM and with the DFT cluster.

Cu-MFI	DFT	ONIOM
d_{M-C} (Å)	2.11	2.02
d_{M-O4} (Å)	2.04	3.44
d_{M-O2} (Å)	2.28	1.92
d_{M-O5} (Å)	3.33	1.92
Mulliken Charge	-0.16	0.56

Table D- 7. Geometric parameters of the TS for CH_4 dissociation on Zn-MFI obtained with ONIOM and with the DFT cluster.

Zn-MFI	DFT	ONIOM
d_{M-C} (Å)	2.10	2.04
d_{M-O4} (Å)	2.32	2.00
d_{M-O2} (Å)	2.08	3.35
d_{M-O5} (Å)	3.25	1.95
Mulliken Charge	0.21	0.38